

# Pulsar Magnetospheres and Their Radiation

A. Philippov<sup>1,2</sup> and M. Kramer<sup>3</sup><sup>1</sup>Center for Computational Astrophysics, Flatiron Institute, New York, NY, USA<sup>2</sup>Department of Physics, University of Maryland, College Park, Maryland, USA; email: sashaph@umd.edu<sup>3</sup>Max-Planck Institut für Radioastronomie, Bonn, Germany; email: michael@mpifr-bonn.mpg.de

Annu. Rev. Astron. Astrophys. 2022. 60:495–558

The *Annual Review of Astronomy and Astrophysics* is online at [astro.annualreviews.org](http://astro.annualreviews.org)<https://doi.org/10.1146/annurev-astro-052920-112338>Copyright © 2022 by Annual Reviews.  
All rights reserved

## Keywords

coherent radio emission, gamma-ray sources, pair discharges, magnetic reconnection

## Abstract

The discovery of pulsars opened a new research field that allows studying a wide range of physics under extreme conditions. More than 3,000 pulsars are currently known, including especially more than 200 of them studied at gamma-ray frequencies. By putting recent insights into the pulsar magnetosphere in a historical context and by comparing them to key observational features at radio and high-energy frequencies, we show the following:

- Magnetospheric structure of young energetic pulsars is now understood. Limitations still exist for old nonrecycled and millisecond pulsars.
- The observed high-energy radiation is likely produced in the magnetospheric current sheet beyond the light cylinder.
- There are at least two different radio emission mechanisms. One operates in the inner magnetosphere, whereas the other one works near the light cylinder and is specific to pulsars with the high magnetic field strength in that region.
- Radio emission from the inner magnetosphere is intrinsically connected to the process of pair production, and its observed properties contain the imprint of both the geometry and propagation effects through the magnetospheric plasma.

We discuss the limitations of our understanding and identify a range of observed phenomena and physical processes that still await explanation in the

[www.annualreviews.org](http://www.annualreviews.org)

- Download figures
- Navigate cited references
- Keyword search
- Explore related articles
- Share via email or social media

future. This includes connecting the magnetospheric processes to spin-down properties to explain braking and possible evolution of spin orientation, building a first-principles model of radio emission and quantitative connections with observations.

## Contents

1. INTRODUCTION .....	496
2. HISTORICAL OVERVIEW OF THEORETICAL MODELS .....	498
3. BASIC MAGNETOSPHERIC THEORY .....	501
3.1. Force-Free Electrodynamics .....	501
3.2. Time-Dependent Force-Free Electrodynamics Solutions .....	504
3.3. Limitations of Force-Free Electrodynamics .....	506
4. MODERN KINETIC MODELING OF MAGNETOSPHERES .....	507
4.1. Motivation: Gamma-Ray Observations of Pulsars .....	507
4.2. Kinetic Simulations of Magnetospheres: Radiative Particle-in-Cell Method .....	509
4.3. Ghost: The Disk-Dome Solution .....	510
4.4. Magnetospheric Structure with Pair Production .....	512
4.5. Time-Dependent, Dynamic Regions in the Magnetosphere .....	517
5. COHERENT RADIO EMISSION .....	526
5.1. Essential Phenomena to Be Explained .....	526
5.2. Features of Radio Observations .....	527
5.3. “Rosetta Stones” of Observational Results .....	535
5.4. Old and New Ideas on Radio Emission and Propagation Effects .....	541
6. A SUMMARY OF OUR UNDERSTANDING, ITS LIMITS, AND OUTLOOK .....	548

## 1. INTRODUCTION

Pulsars are cosmic lighthouses. The electromagnetic radiation of these rotating neutron stars is visible across the entire spectrum (**Figure 1**), making neutron stars exceptional as being detectable in every acquired window to the cosmos—including that of gravitational waves. Less than 90 years after the prediction of the existence of neutron stars (Landau 1932, Baade & Zwicky 1934)<sup>1</sup> and less than 60 years after the proof of their reality with the discovery of pulsars (Hewish et al. 1968), neutron stars have become an important research field, entangling a wide range of physics. And yet, the pulsar magnetosphere, i.e., the plasma-filled surrounding of the neutron star that is dominated by a strong magnetic field, is not yet fully understood. Its basic structure became clear within less than ten years after the discovery by Bell, Hewish and others (see Section 2). Progress then slowed down, but with the advent of powerful numerical computations, the problem became tractable, and in the last 10 to 15 years or so, remarkable advancements have been made (see **Figure 1** for the up-to-date schematic model and Sections 3 and 4 for more details). In the past, theoretical advance had usually been outpaced by observational results, especially in the radio regime, where the mechanism responsible for the radio emission has still not been identified.

<sup>1</sup>See Yakovlev et al. (2013) for a historical discussion.

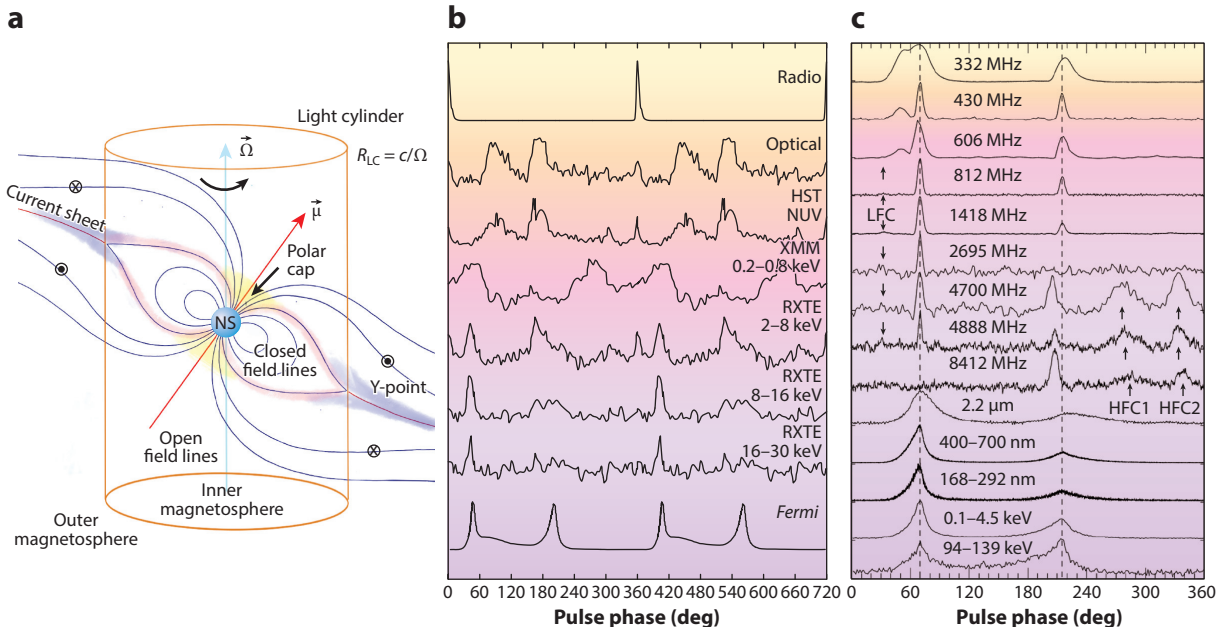


**Figure 1**

(a) Basic structure of the pulsar magnetosphere and indication of the location of the magnetospheric emission (blue lines represent magnetic field lines; see Section 2 for definitions of other quantities), as seen, for instance, for (b) the Vela pulsar with light curves adopted from and aligned as in Kuiper & Hermans (2015) and Spolon et al. (2019), with the radio profile taken from the EPN database (see <http://www.epta.eu.org/epndb/>). (c) The radio components of the Crab pulsar differ from those of normal pulsars and mostly originate from locations near those of the high-energy emission. Panel c provided by Tim Hankins.

Five pulsars have confirmed optical emission of magnetospheric origin (e.g., Shearer & Golden 2002). In contrast, nearly 100 rotation-powered pulsars have been detected in the X-ray band (Becker 2009, Guillot et al. 2019). Here, the emission is typically a combination of nonthermal magnetospheric emission (dominating especially in young and energetic pulsars) and hot thermal emission from the polar cap (dominating in older pulsars). In the former, the X-ray luminosity scales with  $L_X \propto \dot{E}$  (Becker & Trümper 1997, Becker 2009), where  $\dot{E}$  is the rate at which the pulsar loses its rotational energy (Section 2). The opening of the gamma-ray sky because of the *Fermi Gamma-ray Space Telescope* (Abdo et al. 2009) provided crucial observational data points that could be more clearly connected to magnetospheric physics (Section 4), as the emission product and its properties seem to be a more direct consequence of the underlying processes. The insight that was enabled by this refreshed comparison among observations, theory, and numerical simulations has now come full circle, and it seems possible that soon also radio pulsar properties may be understood (Section 5).

Since the discovery of CP1919 (aka PSR B1919+21), more than 3,000 further pulsars have been discovered (see <https://www.atnf.csiro.au/research/pulsar/psrcat/>; Manchester et al. 2005). About 7% are detectable at gamma-ray frequencies (Abdollahi et al. 2020). In addition to relatively slowly rotating, young pulsars with average spin periods of about 0.6 s and magnetic fields of approximately  $10^{12}$  Gauss, in 1982 the class of recycled, fast spinning “millisecond pulsars” was discovered by Backer et al. (1982), with rotational periods of a few milliseconds and magnetic fields of about  $10^8$  Gauss. Then, in 2006, a magnetar, i.e., a slowly rotating, extremely magnetized neutron star, was discovered as a transient radio pulsar (Camilo et al. 2006). Although about

**(Normal) pulsar:**  
nonrecycled radio pulsar spinning down after its formation with canonical periods of  $\sim 0.6$  s and spin-down rates of  $\dot{P} \sim 10^{-15}$

**Millisecond pulsar:**  
recycled old pulsar spun up by mass transfer from a binary companion to rotational periods of typically a few milliseconds

**Magnetar:** neutron star mostly visible during high-energy outbursts powered by extremely large magnetic fields

### Fast radio burst (FRB):

millisecond-long burst of radio emission of unknown origin at cosmological distances

300 millisecond pulsars are now known (i.e., about 10% of the total population of known neutron stars), we are only aware of about 30 (i.e., about 1% of the population) magnetars. Even fewer of them (a handful) are detectable as transient radio sources. Nevertheless, with these manifestations of neutron stars, the observed parameter space that magnetospheric physics has to cover is  $10^4 \times 10^7$  in spin period and magnetic field space, with 10 orders of magnitude variation in spin-down luminosity and with yet another factor of  $10^{16}$  for the range of timescales in observed emission. The fact that—despite an unexpectedly small number of distinct differences in observed properties—we can identify overall very comparable observed properties across these many orders of magnitude is truly remarkable.

It is appropriate to review the current understanding of pulsar magnetospheres. Revisiting the recent progress and contrasting it with our past understanding and our current knowledge of observational facts (see Section 5) are timely not only because of the described advancements but because neutron stars, especially magnetars, are also thought to be responsible for fast radio bursts (FRBs; Lorimer et al. 2007) and other transients (e.g., McLaughlin et al. 2006). We do not cover FRBs,<sup>2</sup> but the physics described here will obviously serve as important material in corresponding discussions.

The plan of this review is as follows. We continue with a historic overview of the magnetospheric models (Section 2) before we present their basic ingredients in Section 3 and their modern representations in Section 4. We compare those models with the observed radio emission, which still provides the bulk of the observational data (Section 5). We conclude by reflecting on the limits of our understanding and attempt an outlook into the future (Section 6).

## 2. HISTORICAL OVERVIEW OF THEORETICAL MODELS

The earliest model of the pulsar magnetosphere (Pacini 1967, Gunn & Ostriker 1970) applied vacuum electrodynamics to a rotating perfect conductor endowed with a magnetic dipole moment  $\mu$  at the center of the neutron star, which is inclined with respect to the rotational axis by an angle  $\chi$ . A rotating dipole in vacuum radiates an electromagnetic wave that carries energy and angular momentum flux outward, which leads to the spin down of the pulsar. The net radiated Poynting flux is  $L = (2/3)(\mu^2 \Omega^4 / c^3) \sin^2 \chi$  (Landau & Lifshitz 1975), where  $\Omega = 2\pi/P$  is the rotation rate of the pulsar,  $P$  is the spin period, and  $c$  is the speed of light. The 3D solution of Maxwell's equations in vacuum for a finite stellar radius by Deutsch (1955)<sup>3</sup> describes the full electromagnetic field structure outside the star.

For the simplest case of the aligned rotator,  $\chi = 0$  deg, the electric field structure can be found as a solution of Poisson's equation in vacuum,  $\nabla^2 \Phi = 0$ , where  $\Phi$  is an electric potential. The neutron star is approximated well by a perfect conductor. Thus, the electric field in the corotating frame inside the star vanishes, which leads to the following expression in the pulsar (laboratory) frame:  $\mathbf{E}^{\text{star}} = -(\boldsymbol{\Omega} \times \mathbf{r}) \times \mathbf{B}/c$ , where  $\mathbf{B}$  is the magnetic field, and  $\mathbf{r}$  is the position vector. The continuity of the tangential component of the electric field,  $E_\theta^{\text{star}} = -(\Omega R_*/c) B_r$ ,  $E_\phi^{\text{star}} = 0$ , sets the boundary condition at the stellar surface,  $r = R_*$ . Here,  $B_r = 2\mu \cos \theta / R_*^3$  is the radial component of the dipolar field at the stellar surface and  $\theta$  is a latitude angle also used in the spherical coordinate system aligned with the spin vector,  $(r, \theta, \phi)$ . The solution of Poisson's equation describes a quadrupolar electric field:  $(E_r, E_\theta, \text{ and } E_\phi) = (\Omega R_*/c)(\mu/R_*^3)(R_*/r)^4(1 - 3 \cos^2 \theta, -\sin 2\theta, 0)$ . The radial component of the electric field is not continuous, implying the presence of a surface charge,

<sup>2</sup>For a detailed discussion of FRBs, we refer to the recent reviews by Cordes & Chatterjee (2019), Petroff et al. (2019), and Caleb & Keane (2021).

<sup>3</sup>Some typos were later corrected by Michel & Li (1999).

$4\pi\Sigma = E_r - E_r^{\text{star}} = -2(\Omega R_*/c)(\mu/R_*^3)\cos^2\theta$ , which is negative over the whole surface (Mestel 1971). For a zero total charge of the star, this requires the stellar interior to be positively charged (see Section 4.3 for implications; also Michel & Li 1999).<sup>4</sup>

The component of the electric field along the magnetic field,  $E_{\parallel}$ , as determined from  $\mathbf{E} \cdot \mathbf{B} = -4\cos^3\theta(\Omega R_*/c)(\mu/R_*^3)^2$ , points inward at all latitudes. A free charged particle would be accelerated to enormous energies by these electric fields. Despite still being used as a description of the magnetic field structure for the radio and high-energy emission modeling, the vacuum description of the magnetosphere has a fatal flaw. Namely, radio observations of the synchrotron emission in the pulsar wind nebulae (PWNe) implicitly infer that a large density of the plasma has to be present in the magnetosphere (e.g., Bucciantini et al. 2011). Such dense plasma is able to easily “screen” the accelerating electric fields of the vacuum model and drastically modify the magnetic field structure.

Goldreich & Julian (1969) considered the first model of a plasma-filled magnetosphere of the aligned rotator,  $\chi = 0$  deg. They realized that large parallel electric fields in the vacuum model,  $\mathbf{E} \cdot \mathbf{B} \neq 0$ , easily overcome the gravitational acceleration toward the stellar surface and lead to extraction of charges from the upper layers of the neutron star. Polarization currents in this plasma drive electric fields that are directed opposite to the externally imposed electric field; these fields effectively screen the  $\mathbf{E} \cdot \mathbf{B} \neq 0$  regions of the vacuum model. In a steady state, the electric field in the frame of the moving plasma vanishes, which corresponds to the well-known frozen-in condition in the pulsar frame,  $\mathbf{E} = -\mathbf{v} \times \mathbf{B}/c$ , where  $\mathbf{v}$  is the plasma velocity, and  $\mathbf{E} \cdot \mathbf{B} = 0$ . The time of synchrotron losses in magnetic fields near the magnetic pole of a regular pulsar,  $B_* \sim 10^{12}$  G, is extremely short,  $\sim(1/\omega_B)(c/\omega_B r_e) \sim 10^{-15}$  s (Landau & Lifshitz 1975); hereafter,  $\omega_B = eB/m_ec$  is the nominal gyrofrequency of the electron and  $r_e = e^2/m_ec^2$  is the classical electron radius. This restricts plasma particles to only move along magnetic field lines and experience an  $\mathbf{E} \times \mathbf{B}$  drift perpendicular to them.

In a state with  $\mathbf{E} \cdot \mathbf{B} = 0$  everywhere, the electric field has to satisfy the condition  $\mathbf{E} = \mathbf{E}_{\text{cor}} = -(\boldsymbol{\Omega} \times \mathbf{r}) \times \mathbf{B}/c$  in the whole magnetosphere (Section 3.1.2), which leads to corotation of the plasma with the star. Rigid rotation becomes impossible at large distances from the rotation axis,  $\geq R_{\text{LC}}$ , where the rotation velocity exceeds the speed of light. Hereafter,  $R_{\text{LC}} = c/\Omega \approx 4,775$  km (P/0.1 s) is called the light cylinder radius. Magnetic field lines originating at the stellar surface that cross the light cylinder have to open up to infinity, whereas the other field lines remain closed. The size of the open field line region around the magnetic poles, called the polar cap, can be estimated using magnetic flux conservation and assuming that the magnetic field in the closed zone remains nearly dipolar,  $R_{\text{PC}} \approx R_*\theta_{\text{PC}} \approx R_*\sqrt{R_*/R_{\text{LC}}}$ , where  $\theta_{\text{PC}}$  is the latitude of the last open field line. Plasma can leave the magnetosphere along the open magnetic field lines, whereas in the closed zone particles mainly corotate with the star. In order to sustain corotation, magnetospheric plasma has to be locally charged with a charge density  $\rho_{\text{GJ}} = \nabla \cdot \mathbf{E}_{\text{cor}}/4\pi \approx -\boldsymbol{\Omega} \cdot \mathbf{B}/2\pi c$ , called the Goldreich–Julian charge density. It corresponds to a number density  $n_{\text{GJ}} \sim \rho_{\text{GJ}}/e \sim 10^{12}(B_*/10^{12}\text{ G})(P/0.1\text{ s})^{-1}\text{ cm}^{-3}$  near the pulsar. The flow of charged particles along the open field lines then drives a characteristic current density,  $j_{\text{GJ}} \approx \rho_{\text{GJ}}c$ . The total current in the open field line region can be found as  $I = j_{\text{GJ}}(\pi R_{\text{PC}}^2) \sim \mu\Omega^2/c$ . It induces a toroidal component of the magnetic field,  $B_\phi = 2I/cR$ , where  $R$  is the cylindrical radius. The result is a charge-separated wind, which carries the Poynting flux,  $(c/4\pi)(\mathbf{E}_{\text{cor}} \times \mathbf{B}_\phi)$ , outward. The total rate of particle injection into the wind is  $\dot{N}_{\text{GJ}} \sim I/e \sim 2 \times 10^{32}(B_*/10^{12}\text{ G})(P/0.1\text{ s})^{-2}\text{ s}^{-1}$ , where we assumed  $R_* = 12$  km. The

---

**Light cylinder radius,  $R_{\text{LC}}$ :** the location in the magnetosphere where the corotation velocity equals the speed of light

**Polar cap:** the location on the surface where the open magnetic field lines originate from

**Goldreich–Julian charge density:** charge density required to screen parallel electric fields in the magnetosphere

---

<sup>4</sup>The polarization of the star due to rotation is a result of the same mechanism operating in a Faraday disk (unipolar induction).

**$\gamma_{\text{PC}}$ :** Lorentz factor of a particle experiencing the full vacuum potential drop across the polar cap

**$\gamma_{\text{th}}$ :** minimal Lorentz factor of a particle, which is necessary to emit a curvature photon that can produce a  $e^{\pm}$  pair

**Pair “discharge”:** the process of particle acceleration in the unscreened electric field, accompanied by emission of photons and copious creation of  $e^{\pm}$  pairs

**Gap:** the region close to the stellar surface where the parallel electric field is not fully screened, i.e.,  $E_{\parallel} \neq 0$ .

**Multiplicity parameter,  $\lambda$ :** the ratio of the pair density to the Goldreich–Julian density

**$\gamma_{\text{sec}}$ :** typical Lorentz factor of produced  $e^{\pm}$  pairs

wind is electromagnetically dominated; i.e., the Poynting flux vastly exceeds the particle energy flux.

To quantify the pulsar spin-down rate, the net Poynting flux through the light cylinder can be estimated as  $L_0 \approx cR_{\text{LC}}^2 E_{\text{cor}} B_{\phi}$ , where both  $E_{\text{cor}}$  and  $B_{\phi} \approx 2I/cR_{\text{LC}}$  are comparable with the dipolar field at the light cylinder. Thus, we obtain

$$L_0 \approx \mu^2 \Omega^4 / c^3 \sim 4 \times 10^{35} \text{ erg s}^{-1} (B_{*}/10^{12} \text{ G})^2 (P/0.1 \text{ s})^{-4}. \quad 1.$$

Although this result is within an order of magnitude similar to the vacuum case, the plasma-filled magnetosphere has an exceptional difference: There is a net Poynting flux even in the case of the aligned pulsar, whereas the vacuum configuration predicts none. Currents at the surface of a neutron star,  $\mathbf{J}_s$ , which close the volumetric currents circulating in the magnetosphere, lead to a nonzero torque of the Ampère’s force,  $\mathbf{J}_s \times \mathbf{B}/c$ . As a consequence, the pulsar spins down. The rate of spin down is determined as  $\dot{E} = I\Omega\dot{\Omega} = -L_0 \approx -\mu^2 \Omega^4 / c^3$ , where  $I$  is the moment of inertia of a neutron star. This equation allows for finding<sup>5</sup> the strength of the dipolar field at the pole from observed  $P$  and  $\dot{P}$ ,  $B_{*} = 2\mu/R_{*}^3 \sim 10^{12} \sqrt{P(\dot{P}/10^{-15})} \text{ G}$ , where we assumed  $I = 10^{45} \text{ g} \times \text{cm}^2$ . Observational evidence for this scenario is presented in Section 5.3.3.

The Goldreich–Julian picture was modified by Sturrock (1971), who realized the possibility of electron–positron plasma creation near pulsars. The qualitative picture here is as follows: The vacuum electric potential across the polar cap,  $\Phi_{\text{PC}} \sim (\Omega R_{\text{pc}}/c)B_{*}R_{\text{pc}} \sim \mu\Omega^2/c^2 \sim I/c \sim \sqrt{L_0/c}$ , leads to acceleration of electrons to enormous Lorentz factors,  $\gamma \sim \gamma_{\text{PC}} = e\Phi_{\text{PC}}/mc^2 \sim 10^9 (B_{*}/10^{12} \text{ G})(P/0.1 \text{ s})^{-2}$ . The extracted “primary” particles, however, never reach such high energies. As they accelerate along the curved dipolar magnetic field lines, they emit gamma-ray photons due to curvature radiation, with characteristic energies  $\mathcal{E}_{\text{ph}} \sim \hbar c \gamma^3/\rho_c$ , where  $\rho_c$  is the field line curvature. These photons propagate along straight lines, and the angle between their propagation direction and the dipolar magnetic field increases. In very strong magnetic fields present near the surface, these photons produce electron–positron pairs via the single-photon conversion process,  $\gamma + B \rightarrow e^- + e^+$ . The produced pairs have nonzero pitch angles and very quickly lose all of the transverse component of their momentum owing to synchrotron radiation, which contributes further to the creation of new  $e^{\pm}$  pairs. These new particles are then again accelerated and produce more photons and pairs. Quickly, the pulsar magnetosphere gets filled with dense pair plasma of density  $n_e = \lambda n_{\text{GJ}}$ , leading to the screening of the vacuum voltage and limiting Lorentz factors of primary particles at  $\gamma_{\text{th}} \sim 10^6\text{--}10^7$ . The process of particle acceleration, emission of photons, and copious pair creation is called a pair cascade or a pair “discharge.” The region with a nonzero  $E_{\parallel}$  is called a “gap”. Hereafter,  $\lambda = n_e/n_{\text{GJ}} \sim 10^3\text{--}10^5$  is the cascade multiplicity parameter. The produced, “secondary,” plasma streams along the field lines with Lorentz factors of  $\gamma_{\text{sec}} \sim 10\text{--}10^3$ . In most pulsars, except the very young ones (see Section 4.5.1), the  $\gamma + B$  pair creation channel provides most of the plasma in the magnetosphere. As the pulsar spins down, and its period increases, the polar cap voltage drops, and at some point  $\gamma + B$  pair creation becomes impossible. Pulsars enter this regime by crossing the death line, expected for polar voltages  $\Phi_{\text{PC}} \lesssim 10^{12} \text{ V}$ , assuming the cascade is driven by curvature radiation gamma rays (Sturrock 1971). The fact that the observed radio pulsar death line roughly coincides with this condition suggests

<sup>5</sup>We use this equation to draw constant  $B_{*}$  lines in the  $P$ – $\dot{P}$  diagram in Section 6. It is formally applicable only for the plasma-filled magnetosphere of an aligned rotator. Corrections due to the finite inclination angle,  $\sqrt{1 + \sin^2 \chi} \leq \sqrt{2}$ , bring only modest uncertainty (see Section 3.2). This equation also does not constrain the strength of a possible nondipolar field near the surface, which does not contribute to the spin-down torque.

that pulsar activity (in particular, generation of coherent radio emission) is directly connected with the process of pair creation (Ruderman & Sutherland 1975).

It was debated whether both electrons and ions can be freely extracted from the surface of the neutron star. Initial studies concluded that the work function, i.e., the energy required to pull an electron or ion out of the condensed surface of a neutron star crust, may be significant for ions (Ruderman 1974). More detailed calculations showed that typical surface temperatures,  $T_s$ , of pulsars provide sufficient surface emission of both electrons and ions (Mueller 1984, Jones 1986). In fact, for typical parameters of young pulsars,  $T_s \sim 10^6$  K and  $B_* \lesssim 10^{13}$  G, the likely state is not a condensed surface but a gaseous atmosphere (Potekhin 2014), the upper layers of which should freely provide charges. Detailed models of the polar gap with free escape of particles were first considered by Arons and colleagues (e.g., Arons & Scharlemann 1979). Such models were constructed under the assumption of a steady state. Analytically, the current through the pair production region has been found to be very close to the Goldreich–Julian current,  $j_{GJ}$  (Arons & Scharlemann 1979).

Later theoretical developments focused on constructing global magnetospheric solutions with overly simplified assumptions (e.g., with the field-aligned component of the current that either was zero or depended linearly on the magnetic flux, as in Beskin et al. 1983) and models of particle acceleration and production of high-energy emission in the slot gap (the region near the last open field line; e.g., Arons 1983, Muslimov & Harding 2004) and outer gap (the region around the surface  $\rho_{GJ} = 0$ , where a potential drop has to develop in a charge-separated outflow; e.g., Cheng et al. 1986, Romani 1996). We do not summarize these efforts, but rather focus on modern approaches, which we think are significantly more promising for explaining pulsar phenomena. In retrospect, we have to conclude that before the rise of the available computational power, which enabled detailed numerical calculations in the early 2000s, not much progress had been made in trying to find a quantitative, self-consistent structure of the pulsar magnetosphere, even under the assumption of the fully screened parallel electric field,  $\mathbf{E} \cdot \mathbf{B} = 0$ , everywhere in the magnetosphere. In the absence of a reliable global model, progress in identifying the locations where the observed emission is produced has proven to be remarkably challenging.

---

**Force-free electrodynamics (FFE):** a set of equations describing the dynamics of the electromagnetic field in a magnetically dominated plasma

---

### 3. BASIC MAGNETOSPHERIC THEORY

#### 3.1. Force-Free Electrodynamics

Although the existence of regions with unscreened electric field is required to fill the magnetosphere with dense pair plasma,  $\lambda \gg 1$ , it is reasonable to study the global field geometry of magnetospheres with  $\mathbf{E} \cdot \mathbf{B} = 0$  as a starting point. This assumption demands that deviations from the screening condition are small and are localized to small regions in the magnetosphere, where our discussions would not apply. Assuming that the neutron star has a dipolar magnetic field, the ratio of the particle kinetic energy density,  $\epsilon_{\text{kin}}$ , in the magnetosphere to the energy density of the magnetic field,  $\epsilon_B$ , at the distance  $r$  can be estimated as  $\epsilon_{\text{kin}}/\epsilon_B \sim (\rho_{GJ}/e)(\lambda m_e c^2 \gamma_{\text{sec}})/(B^2/8\pi) \sim 10^{-11} P^{-1}(\lambda/10^5)(\gamma_{\text{sec}}/10^2)(B_0/10^{12} \text{ G})^{-1}(r/R_*)^3$ . This ratio is small within the light cylinder of pulsars, where the assumption of the dipolar field holds. Thus, it is well justified to neglect the plasma pressure and inertia terms in the plasma momentum equation everywhere in the magnetosphere. The plasma is then described by the “force-free electrodynamics” (FFE), a highly magnetized limit of the ideal relativistic magnetohydrodynamics (MHD). Plasma dynamics are governed by the electromagnetic force balance,

$$\rho \mathbf{E} + \mathbf{j} \times \mathbf{B}/c = 0, \quad 2.$$

which is a relativistic generalization of the force-free equation,  $\mathbf{j} \times \mathbf{B} = 0$ , used to describe, e.g., the solar corona (e.g., Wiegelmann & Sakurai 2021). This condition fixes the components of the

plasma current across the magnetic field while leaving the current along the magnetic field,  $j_{\parallel}$ , unspecified:

$$\mathbf{j} = c\rho \frac{\mathbf{E} \times \mathbf{B}}{B^2} + j_{\parallel} \frac{\mathbf{B}}{B}. \quad 3.$$

Here, the first term describes the advection of the charge density,  $\rho = \text{div}\mathbf{E}/4\pi$ , with the  $\mathbf{E} \times \mathbf{B}$ -drift velocity, which is subluminal by the assumption of relativistic magnetohydrodynamics,  $E < B$ , and the second term is the field-aligned component of the current. Two approaches were used for studying the magnetospheric geometry in the FFE limit: quasi-stationary, usually applied to magnetospheres of axisymmetric magnetospheres, and general time-dependent.

**3.1.1. Axisymmetric magnetospheres.** In the axisymmetric case, Scharlemann & Wagoner (1973) and Michel (1973) derived a relativistic FFE extension of the Grad–Shafranov equation, which was constructed a decade earlier to describe MHD equilibria of axisymmetric toroidal plasma configuration in tokamaks. In this approach, the poloidal magnetic field is described by the magnetic flux function,  $\Psi$ , in cylindrical coordinates,  $(R, z)$ , where the axis is aligned with both the magnetic dipole and the rotational axis. The toroidal field component is described by the current function,  $I$ , such that  $\mathbf{B} = \nabla\Psi \times \mathbf{e}_{\phi}/2\pi R + 2(I/cR)\mathbf{e}_{\phi}$ . With this choice, Maxwell's equation  $\nabla \cdot \mathbf{B} = 0$  holds automatically. It is readily seen that  $\mathbf{B} \cdot \nabla\Psi = 0$ , and thus the condition  $\Psi(R, z) = \text{constant}$  actually defines magnetic flux surfaces. The coefficient of proportionality is chosen so that the quantity  $\Psi$  coincides with the magnetic flux inside the tube. In the steady state, Faraday's law implies that  $\nabla \times \mathbf{E} = 0$ . In axisymmetry, the poloidal component of this equation then gives  $E_{\phi} = 0$ . Given the orthogonality of electric and magnetic fields,  $\mathbf{E} \cdot \mathbf{B} = 0$ , one finds  $\mathbf{E} = -\Omega_F \nabla\Psi / 2\pi c$ . Substituting this choice into  $(\nabla \times \mathbf{E})_{\phi} = 0$  gives  $\mathbf{B} \cdot \nabla\Omega_F = 0$ , so that  $\Omega_F$  has to be constant on flux surfaces,<sup>6</sup>  $\Omega_F = \Omega_F(\Psi)$ . In the perfectly conducting magnetosphere, boundary conditions at the surface yield  $\Omega_F(\Psi) = \Omega$ . In the stationary version, Equation 2 reduces to  $\mathbf{E} \cdot (\nabla \cdot \mathbf{E}) + (\nabla \times \mathbf{B}) \times \mathbf{B} = 0$ , and by plugging in these choices for the electromagnetic field, one obtains the “axisymmetric pulsar equation,”

$$\left(1 - \frac{R^2}{R_{LC}^2}\right) \nabla^2\Psi - \frac{2}{R} \frac{\partial\Psi}{\partial R} + \frac{16\pi^2}{c^2} I(\Psi) \frac{\partial I}{\partial\Psi} = 0, \quad 4.$$

a single equation for two unknowns,  $\Psi(R, z)$  and  $I(\psi)$ . It is supplemented with boundary conditions at the stellar surface that define the normal component of the magnetic field,  $\Psi(r = R_*, \theta) = \Psi_0(\theta)$ , where  $r$  is a spherical radius. The current function,  $I(\psi)$ , has to be determined by the smoothness of the solution at the critical (singular) surface,  $R = R_{LC}$ . Historically, this uncertainty in the magnitude of the magnetospheric current has been a major theoretical problem, which has only been resolved in the self-consistent way in the era of time-dependent numerical simulations.

Given the complexity of Equation 4, and the unspecified nature of the function  $I(\Psi)$ , its analytical solution is known only in rare cases. An important example is Michel's split-monopole solution,  $B_r = B_*(R_*/r)^2 \text{sign}(\pi/2 - \theta)$ ,  $E_{\theta} = B_{\phi} = -(\Omega R/c)B_r$ , which has proven to be a reasonable approximation of the pulsar wind at distances beyond the light cylinder,  $r \gg R_{LC}$  (Michel 1973). A numerical solution to Equation 4 with dipolar boundary conditions at the stellar surface has been obtained first by Contopoulos et al. (1999) using an iterative algorithm, and later reproduced by Gruzinov (2005) and Timokhin (2006). Results have been obtained by solving this equation separately inside and outside the light cylinder for a trial current function and adjusting  $I(\Psi)$  to ensure that the solution is smooth across the light cylinder. For a resulting flux function  $\Psi$ , the solution passes smoothly through the light cylinder, as is shown in **Figure 2a** (Timokhin

---

<sup>6</sup>This represents a specific example of Ferraro's isorotation theorem (Ferraro 1937).

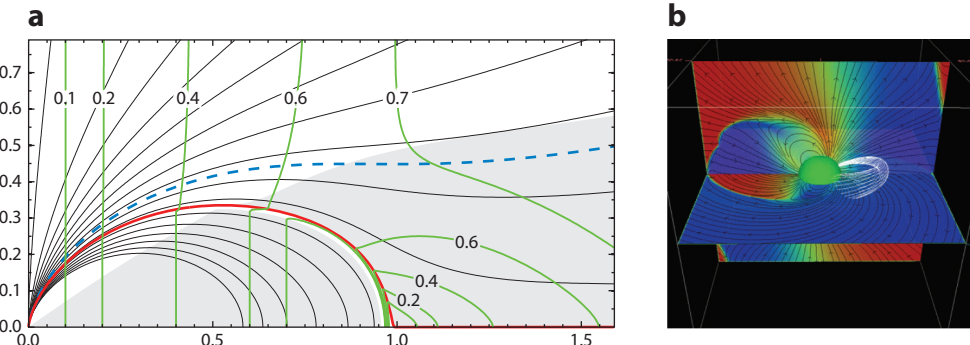


**Figure 2**

Magnetospheric structure in the FFE approximation. (a) Axisymmetric magnetosphere. Thin solid lines show constant flux surfaces; the labeled green lines are contours of the drift velocity in units of the speed of light, the gray area is the domain where Goldreich–Julian charge density is positive. The dashed line separates regions with direct (*above the line*) and return (*below the line*) volume currents. The separatrix is shown by a thick solid red line. Distances are measured in the units of the  $R_{LC}$ . (b) Slices through the FFE magnetosphere of a 60-deg-inclined pulsar. The color on the vertical plane shows the in- and out-of-plane magnetic field component on the horizontal plane–toroidal field. A sample flux tube emerging from the polar cap is traced in white from the polar cap. Panel *a* adapted from Timokhin (2006). Panel *b* adapted from Spitkovsky (2006). Abbreviation: FFE, force-free electrodynamics.

2006). It reproduces many features hypothesized by Goldreich & Julian: the presence of open and closed field line regions, and the current flow concentrated in the polar cap. The field-aligned current and the toroidal component of the magnetic field are zero in the closed field region, which is set by the condition  $\Psi > \Psi_{PC} = 1.23\Psi_0$  at the stellar surface, where  $\Psi_0 = \mu/R_{LC}$  is the flux through the polar cap for an unperturbed dipole. The larger size of the open field line region compared to the vacuum case is caused by the inflation of the poloidal field lines by the toroidal current,  $J_\phi = \rho v_\phi$ , in the closed zone.

The magnetosphere features a Y-shaped current sheet. Within the light cylinder, the jump of the toroidal field at the boundary of the closed field line region is supported by a thin “separatrix” return current layer. All magnetic field components change their sign across the equator beyond the light cylinder, forming a strong equatorial current sheet, where magnetic reconnection takes place. The current sheet carries most of the return current in the magnetosphere, which ensures that the net current through the star vanishes, and the stellar charge does not grow. The outer edge of the polar cap supports a volume return current,  $j_\parallel/\rho_{GJ}c < 0$ , and the solution requires  $|j_\parallel/\rho_{GJ}c| \leq 1$  in the bulk of the polar cap outside of the thin separatrix return current layer. Timokhin (2006) noticed that these features contradict the steady-state discharge theories, which predicted  $j_\parallel \sim \rho_{GJ}c$  (Arons & Scharlemann 1979). The Poynting flux energy losses of the solution were found to be  $L_0 = (1.0 \pm 0.1)(\mu^2 \Omega^4/c^3)$ , which is consistent with the order-of-magnitude estimate in Section 2. Timokhin (2006) also realized that steady-state solutions can be constructed for any position of the Y-point,  $R_Y$ , within the light cylinder. These solutions have higher spin-down losses,  $\sim (R_{LC}/R_Y)^2$ , reflecting a larger fraction of magnetic flux opening to infinity.

**3.1.2. Oblique magnetospheres.** In the more general oblique geometry of the magnetosphere, when the magnetic dipole moment and rotational axis are misaligned, the progress in analytical modeling has been particularly challenging. A few attempts were made (Beskin et al. 1983, Mestel et al. 1999), which only succeeded in constructing solutions for overly simplified field-aligned current distributions. We only emphasize one important analytical finding, which later proved to

**Current sheet:** a thin surface outside the light cylinder that separates regions with opposite magnetic polarities

**Separatrix return current layer:** a thin layer of intense current at the boundary between the open and the closed field lines

be useful to describe the results of three-dimensional simulations. Assuming a quasi-stationary solution, i.e., depending on time and azimuthal angle only in the combination  $\phi' = \phi - \Omega t$ , one can substitute the time derivative of the arbitrary vector field,  $\mathbf{A}$ , with its spatial derivatives (see, e.g., Beskin 2010):  $(1/c)d\mathbf{A}/dt = -(\boldsymbol{\beta}_R \cdot \nabla)\mathbf{A} + \boldsymbol{\Omega} \times \mathbf{A}/c$ , where  $\boldsymbol{\beta}_R = \boldsymbol{\Omega} \times \mathbf{r}/c$ . Because  $\nabla \cdot \boldsymbol{\beta}_R = 0$ , this expression can be rewritten as  $(1/c)d\mathbf{A}/dt = \nabla \times (\boldsymbol{\beta}_R \times \mathbf{A}) - (\nabla \cdot \mathbf{A})\boldsymbol{\beta}_R$ . Time-dependent Maxwell's equations then take the following form in the quasi-stationary state:  $\nabla \times (\mathbf{E} + \boldsymbol{\beta}_R \times \mathbf{B}) = 0$  (Faraday's law), and  $\nabla \times (\mathbf{B} - \boldsymbol{\beta}_R \times \mathbf{E}) = (4\pi/c)(\mathbf{j} - c\rho\boldsymbol{\beta}_R)$  (Ampère's law), where we used  $\nabla \cdot \mathbf{E} = 4\pi\rho$  and  $\nabla \cdot \mathbf{B} = 0$ . Faraday's law, together with the frozen-in boundary condition at the stellar surface, results in  $\mathbf{E} = -\boldsymbol{\beta}_R \times \mathbf{B}$  everywhere in the magnetosphere, and in a new form of the expression for the magnetospheric current,  $\mathbf{j} = \rho c\boldsymbol{\beta}_R + \Lambda\mathbf{B}$ . Plugging this expression into Ampère's law, we get a form of the pulsar equation that is valid for the arbitrary inclinations (Mestel 1973):

$$\nabla \times (\mathbf{B} + \boldsymbol{\beta}_R \times \boldsymbol{\beta}_R \times \mathbf{B}) = \Lambda\mathbf{B}. \quad 5.$$

The unspecified function  $\Lambda$  is then constant along magnetic field lines,  $\mathbf{B} \cdot \nabla \Lambda = 0$ , similar to the current function,  $I(\Psi)$ , in the axisymmetric case. Although Equation 5 has never been solved directly, the conserved quantity  $\Lambda = (\mathbf{j} - \rho c\boldsymbol{\beta}_R) \cdot \mathbf{B}/B^2$ , which is the ratio between the field-aligned component of the current in the corotating frame and the local magnetic field strength, is useful for visualizing the current distribution in the steady state of three-dimensional magnetospheres (see Section 3.2.2).

### 3.2. Time-Dependent Force-Free Electrodynamics Solutions

Despite the attractiveness of the axisymmetric stationary solution by Contopoulos et al. (1999), questions remained about its stability and applicability to real oblique pulsars. Significant progress in time-dependent modeling of FFE magnetospheres of oblique rotators came with the advent of modern supercomputers and yet another theoretical formulation. In particular, Gruzinov (1999) and Blandford (2002) found that the current component along the magnetic field in Equation 3 can be expressed directly from the conditions  $\mathbf{E} \cdot \mathbf{B} = 0$  and  $\partial_t(\mathbf{E} \cdot \mathbf{B}) = (c\nabla \times \mathbf{B} - 4\pi\mathbf{j}) \cdot \mathbf{B} - (c\nabla \times \mathbf{E}) \cdot \mathbf{E} = 0$ , arriving at the expression for the full FFE current as a function of electromagnetic field components only:

$$\mathbf{j} = c \frac{\nabla \cdot \mathbf{E}}{4\pi} \cdot \frac{\mathbf{E} \times \mathbf{B}}{B^2} + \frac{c}{4\pi} \frac{(\nabla \times \mathbf{B}) \cdot \mathbf{B} - (\nabla \times \mathbf{E}) \cdot \mathbf{E}}{B^2} \mathbf{B}. \quad 6.$$

This expression for the magnetospheric current allows for a time-dependent numerical solution of Faraday's and Ampère's laws, with initial and boundary conditions at the stellar surface, e.g., a frozen-in condition. The beauty of this approach is that time-dependent equations do not have a singular surface at the light cylinder, and, thus, the solutions of these equations naturally produce a unique current distribution in the magnetosphere, which breaks the degeneracy of the quasi-stationary approach. Despite the complexity, multiple numerical methods were developed to solve this formulation, including the one first applied to oblique pulsar magnetospheres by Spitkovsky (2006). Significant differences in the methods appear in how they treat current sheets, which are a very generic feature of the FFE evolution. In current sheets, magnetic fields can go through zero. This violates the conditions of FFE validity (neglecting both plasma pressure and inertia terms, and the assumption of magnetic dominance), and requires adding dissipative terms into Equation 6, to restore  $E < B$  and  $\mathbf{E} \cdot \mathbf{B} = 0$ .

**3.2.1. Magnetospheric substructure and spin-down losses.** Applications of these numerical methods by Spitkovsky (2006; and later by Kalapotharakos & Contopoulos 2009 and Pétri 2012)

unraveled the time-dependent aspects of aligned and oblique FFE magnetospheres. In particular, it was found that time-dependent evolution generally leads to a solution with the Y-point localized near the light cylinder, resulting in a state with minimal pulsar spin down. The obtained magnetospheric structure of the oblique rotator shares the general properties of the aligned solution (see **Figure 2b** for a visualization of the numerical solution of a 60-deg-inclined rotator), with open and closed field line regions separated by a Y-shaped current sheet. For an oblique rotator, the current sheet outside the light cylinder has the shape of a ballerina skirt (“striped wind,” a relativistic analog of the Parker current sheet around the Sun). It oscillates around the equatorial plane with the angular amplitude  $\chi$  and a wavelength of  $2\pi R_{LC}$ . FFE simulations computed the spin-down power for an arbitrary inclination angle,  $L \approx L_0(1 + \sin^2 \chi)$  (Spitkovsky 2006; see the **Supplemental Text** for the explanation of this dependence).

$\alpha$ : ratio of the field-aligned current density to the Goldreich–Julian current density

## Supplemental Material >

**3.2.2. Magnetospheric current flow.** Time-dependent FFE simulations predict the distribution of the field-aligned current in the magnetosphere and in the polar cap, which is interesting in the context of modeling pair production in the open field line region. As we discuss in Section 4.5.1, a crucial quantity that defines the operation of polar cap discharge is the ratio between the field-aligned current and the Goldreich–Julian charge density, which defines the characteristic amount of charge that can be extracted from the stellar surface,  $\alpha = j_{||}/(\rho_{GJ}c)$  (Mestel et al. 1985, Beloborodov 2008, Timokhin & Arons 2013). Two qualitatively different behaviors are possible. If  $0 \leq \alpha < 1$  is satisfied along the magnetic field line, the charge-separated flow extracted from the surface and pushed to mildly relativistic velocities,  $v/c = \alpha < 1$ , is able to alone provide magnetospheric charge density and current, without the need for pair production. For field lines with super-Goldreich–Julian currents,  $\alpha \geq 1$ , or return currents,  $\alpha < 0$ , the charge-separated flow extracted from the polar cap is not sufficient. Lack of plasma leads to the appearance of vacuum gaps with nonzero  $E_{||}$ , particle acceleration, and copious creation of  $e^\pm$  pairs (see Section 4.5.1). At distances  $r \lesssim R_{pc}$ , where the acceleration of primary particles occurs in the case  $\alpha > 1$ , the effects of general relativity (GR) need to be accounted for. To the lowest order in stellar spin, the exterior metric of a rotating neutron star coincides with the Kerr metric, and the most important GR effect is frame dragging. It reduces the Goldreich–Julian charge density at the pole compared to the flat-space value (Beskin 1990, Muslimov & Tsygan 1992):  $\rho_{GJ} \approx -(\Omega - \omega_{LT})B_*/(2\pi c\alpha_{GR})$ , where  $\alpha_{GR}$  is the lapse function,  $\omega_{LT} = (2/5)\Omega(r_s/R_*)$  is the Lense–Thirring angular frequency near the stellar surface, and  $r_s = 2GM_*/c^2$  is the Schwarzschild radius.<sup>7</sup> However, current density in the polar region is set by the twist of the magnetic field lines at the light cylinder, which is located far enough from the star to be unaffected by GR effects. Thus, by fitting the current distribution in the FFE special-relativistic simulation results, best represented with the conserved quantity  $\Lambda$ , and using an analytical expression for  $\rho_{GJ}$ , one can calculate the distribution of  $\alpha$  in the polar cap for the arbitrary obliquity of the pulsar (Gralla et al. 2017).

The conserved quantity  $\Lambda$  is essentially converged with the ratio of the stellar radius and light cylinder,  $\epsilon = R_*/R_{LC}$ , in the sense that  $\Lambda/\epsilon$  changes very little for  $\epsilon \lesssim 0.1$ . In **Figure 3**, we show the distribution of  $\alpha$  in the polar cap for different inclination angles and the compactness parameter  $C = 2GM/(c^2 R_*) = 0.5$ . For nearly aligned rotators, the addition of the frame-dragging effect makes the current in the region around the magnetic axis exceed the Goldreich–Julian current,  $\alpha > 1$  (Philippov et al. 2015a, Belyaev & Parfrey 2016, Gralla et al. 2016). Presence of the  $\alpha > 1$  region is generic for all obliquity angles. For sufficiently inclined rotators,  $\chi \geq 40$  deg, a large

<sup>7</sup>For purposes of describing the electrodynamics in the pair production region, the metrics can be safely approximated to the first order in stellar spin,  $ds^2 = \alpha_{GR}^2 c^2 dr^2 - (dr^2/\alpha_{GR}^2 + r^2 d\theta^2 + r^2 \sin^2 \theta d\phi^2) + 2g_{ti} dt dx^i$ , where  $\mathbf{g}_t = \boldsymbol{\omega}_{LT} \times \mathbf{r}$  and  $(t, r, \theta, \phi)$  are the Boyer–Lindquist coordinates.

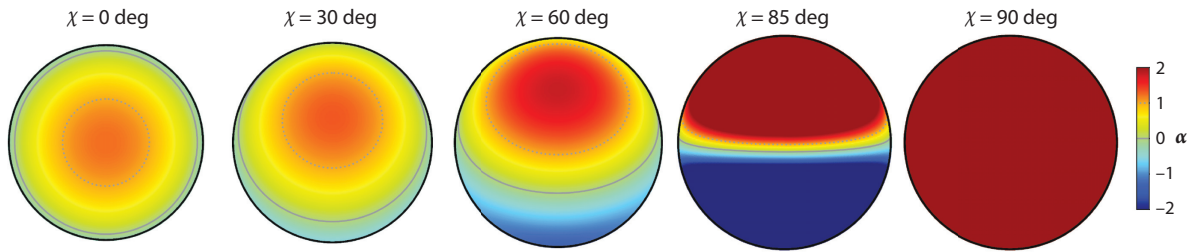


**Figure 3**

Distribution of the volumetric field-aligned magnetospheric current normalized to the Goldreich–Julian current,  $\alpha = j_{\parallel}/(c\rho_{\text{GJ}})$ , in the polar cap of the force-free electrodynamics dipolar magnetosphere for different inclination angles: 0, 30, 60, 85, and 90 deg; calculated using analytical fits to the current distribution from Gralla et al. (2017) for the neutron star compactness,  $C = 0.5$ , and a period corresponding to J1906+0746,  $P = 0.14$  s (see Section 5.3.2). The dotted and thick gray lines mark the boundaries of the regions  $\alpha > 0$  and  $\alpha < 0$ , where the pair production is expected. The solid black line shows the boundary of the polar cap, where there is a thin separatrix return current layer for all inclinations. For all inclinations but the orthogonal rotator ( $\chi = 90$  deg), the null surface does not cross the polar cap and  $\rho_{\text{GJ}}$  does not change sign. This figure was provided by A. Galishnikova.

portion of the polar cap is occupied by a volume return current,  $\alpha < 0$ . The orthogonal rotator,  $\chi = 90$  deg, presents an interesting case. Here, the Goldreich–Julian charge density,  $\sim \Omega B_* \theta_{\text{PC}} / 2\pi c$ , is anomalously small, whereas the total current across the polar cap is comparable with the aligned case,  $j_{\parallel} \sim \Omega B_*/2\pi$ . Thus, for nearly orthogonal rotators, the whole polar cap is occupied by the  $\alpha \sim 1/\theta_{\text{PC}} \gg 1$  region (Beskin 2018). For all inclinations, there is a thin current layer at the boundary of open and closed magnetic field line regions. The distribution of the current in the polar cap is important for interpreting the shape of the radio beam and thermal X-ray emission from the surface heated by the backflow of accelerated particles produced in the discharge or falling back from the Y-point (Section 4.5.1). Searches to find corresponding observational signatures using simultaneous radio and X-ray observations are discussed in Section 5.3.3.

### 3.3. Limitations of Force-Free Electrodynamics

FFE and its numerical solutions describe the general structure of the (mostly ideal, magnetically dominated) magnetosphere. However, they fail to provide information on plasma conditions in regions where nonthermal pulsar radiation presumably originates. The magnetospheric current sheet was hypothesized as a source of multiwavelength, high-energy emission by Lyubarskii (1996b), even before the first self-consistent magnetospheric solution became available. In particular, FFE misses the physics of magnetic reconnection in the equatorial current sheet (e.g., Parfrey et al. 2012, Mahlmann et al. 2021), where the neglected plasma pressure and inertia terms become important. An obvious extension is to consider the full set of equations of relativistic MHD (e.g., Komissarov 1999), which capture the conversion of magnetic energy into plasma pressure in the current sheet. Such studies were performed for both aligned (Komissarov 2006) and oblique (Tchekhovskoy et al. 2013) rotators. However, the very low density of plasma in the magnetosphere, and, thus, its collisionless nature, implies that collisional fluid-based theories cannot correctly capture the physics of plasma production in the discharge and of reconnection in the current sheet. In particular, local studies of reconnection in pair plasma revealed that the anisotropic pressure tensor of heated pairs is important in setting the reconnection dynamics (Bessho & Bhattacharjee 2005). Thus, the  $E > B$  regions are possible at plasma microscales, and nonthermal particle distributions can be easily produced (Guo et al. 2014, Sironi & Spitkovsky 2014). Furthermore, the existence of the FFE solutions relies on the abundant supply of electron–positron pairs

---

#### Magnetic reconnection:

a process occurring in plasmas during which magnetic topology is changed; it is accompanied by the conversion of magnetic energy into kinetic and thermal energy of the plasma

---

everywhere in the magnetosphere. This requires the presence of regions with unscreened electric field that can sustain particle acceleration and pair production. These regions are not described by FFE or relativistic MHD. Such limitations motivate the development of kinetic models, which are able to describe the dynamics of collisionless plasmas,<sup>8</sup> particle acceleration, photon emission, pair production, and plasma feedback on the magnetospheric structure, all self-consistently, as described in the next section.

## 4. MODERN KINETIC MODELING OF MAGNETOSPHERES

### 4.1. Motivation: Gamma-Ray Observations of Pulsars

Observations by *Fermi* have increased the number of detected gamma-ray pulsars from the 6 EGRET (Energetic Gamma-ray Experiment) detections (Thompson 2004) to more than 200 (Abdollahi et al. 2020). The observed population consists of two classes: young pulsars with large spin-down rate,  $\dot{E} \gtrsim 10^{34}$  erg s<sup>-1</sup>, and millisecond pulsars. **Figure 4a** shows the distribution of gamma-ray luminosities,  $L_\gamma$ , as a function of  $\dot{E}$ . The luminosity is calculated as  $L_\gamma = 4\pi d^2 f_\Omega G_{100}$ , where  $d$  is the distance to the pulsar,  $G_{100}$  is the observed energy flux in the 0.1- to 100-GeV band, and  $f_\Omega$  is the correction factor (“beaming fraction”) used to extrapolate the flux to the full sky for some beam shape model and is typically set to unity. The observed distribution shows that in gamma-ray pulsars, a significant fraction, ~10%, of the spin-down power is converted into high-energy photons. Whereas at low  $\dot{E}$  the gamma-ray radiative efficiency,  $L_\gamma/\dot{E}$ , is nearly independent of  $\dot{E}$ , it drops for higher values of the spin-down losses,  $\dot{E} \gtrsim 10^{36}$  erg s<sup>-1</sup>, commonly approximated as  $L_\gamma \sim \sqrt{\dot{E}}$  (**Figure 4a**). The gamma-ray spectrum in the range above 100 MeV shows a hard power law with an exponential cutoff (see example spectra in **Figure 4c**). The value of the cutoff is nearly insensitive to pulsar parameters, in particular, to the strength of the magnetic field at the light cylinder (**Figure 4b**).

The absence of a superexponential cutoff in the spectrum, which should be present if there were absorption of gamma rays in the magnetic field, disfavors polar cap models and suggests the outer magnetosphere as the location where the high-energy emission is produced (e.g., Abdo et al. 2010). This is further strengthened by the fact that the gamma-ray profiles are usually not in phase with radio profiles.<sup>9</sup> Light curves typically show two separated very sharp peaks, sometimes with significant intensity between them, also referred to as the bridge emission (see example light curves in **Figure 4d**). Various geometric models have been constructed to reproduce the observed behavior of light curves. Models based on realistic force-free magnetospheric structure assume the emission location to be in the separatrix current layer close to the light cylinder and in the current sheet beyond it (Bai & Spitkovsky 2010, Kalapotharakos et al. 2014). They find that photons emitted at different points along the trajectory of a particle moving nearly radially outward, close to or inside the current sheet, arrive simultaneously to the observer. Such photons pile up in a caustic in the skymap. Properties of the resulting light curves are qualitatively consistent with the observations.

The high radiative efficiency of *Fermi*-detected gamma-ray emission suggests that, for the first time in pulsar research, observations opened the window into an energetically significant process

**Collisionless plasma:**  
a plasma in which the mean free path for the Coulomb collisions of charged particles is significantly larger than the size of the system of interest

**Beaming fraction:**  
fraction of the sky illuminated by a rotating pulsar’s high-energy or radio beam accounting for nonisotropic emission

<sup>8</sup>In such a plasma, particles interact through the mutually created electromagnetic fields.

<sup>9</sup>There are notable exceptions to this rule, including very young pulsars (for example, the Crab pulsar; see **Figure 1** and Section 5.3.1) and a few millisecond pulsars, which show phase alignment of the high energy and some components of the radio light curves. In this case, a separate, outer-magnetospheric source of radio emission is operating. See Sections 5.2.5 and 5.4.

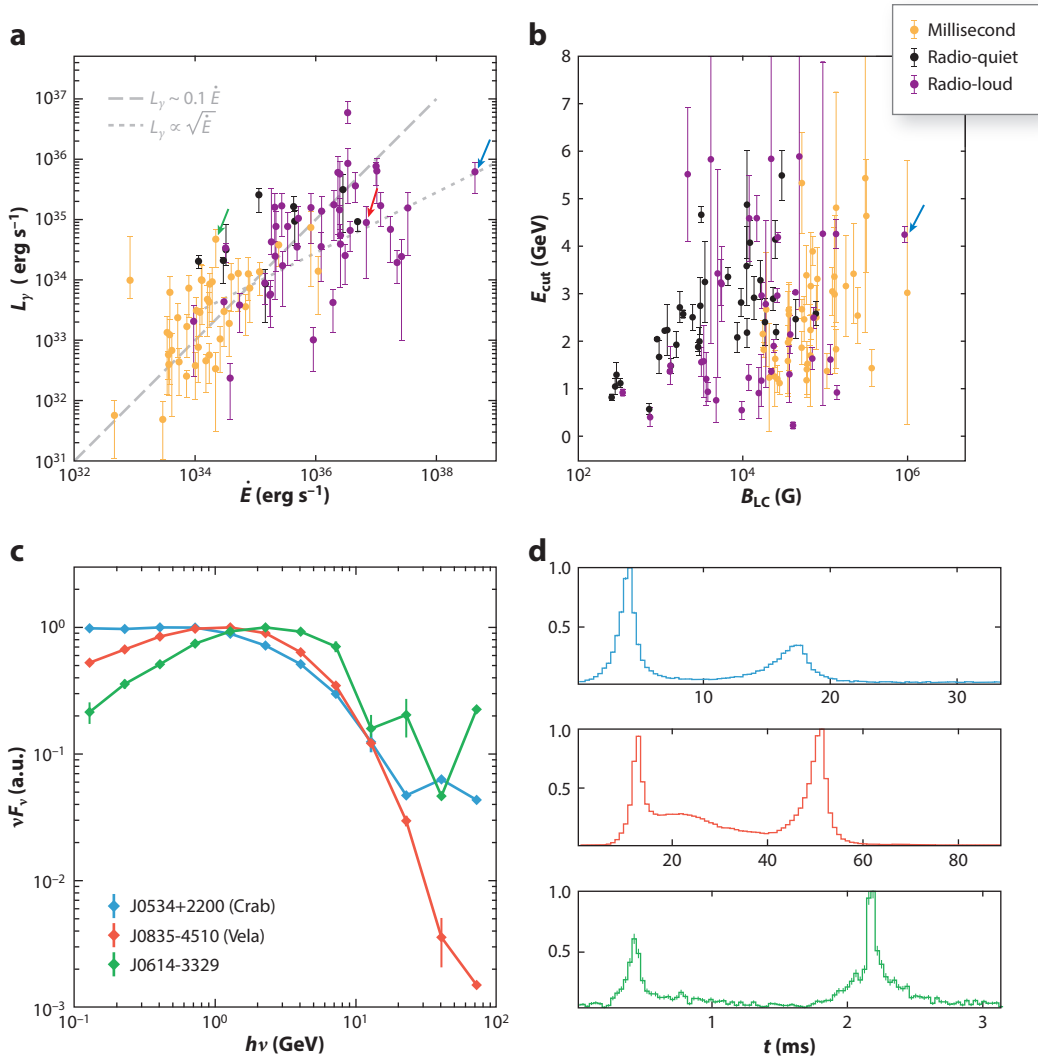


**Figure 4**

Summary of the main properties of gamma-ray emission from pulsars. (a) Gamma-ray luminosities plotted against the spin-down values. The inferred luminosities above the spin-down energy losses,  $L_\gamma \geq \dot{E}$ , are caused by a combination of incorrect distance measurements and beaming assumptions. The lines  $0.1\dot{E}$  and  $\propto\sqrt{\dot{E}}$  are plotted to guide the eye. (b) Dependence of the cutoff energy of the phase-averaged gamma-ray spectrum on the magnetic field strength near the light cylinder. (c) Examples of typical phase-averaged spectra; shown are pulsars J0534+2200 (Crab), J0835-4510 (Vela), and J0614-3329 (millisecond pulsar). (d) Gamma-ray light curves of the same pulsars. The data from this plot are taken from the second *Fermi* catalog (Abdo et al. 2013).

operating in the magnetosphere. These observations called for a new level of understanding of pulsar magnetospheres, which we review below. In particular, the equatorial current sheet, where the Poynting flux emitted by the rotating star can be efficiently converted into kinetic energy of plasma particles and, ultimately, to high-energy photons, emerged as the most promising origin of the observed gamma rays (Lyubarskii 1996b). We review the current sheet physics in Section 4.5.2.

## 4.2. Kinetic Simulations of Magnetospheres: Radiative Particle-in-Cell Method

The most general theory to describe collisionless plasma, as one expects in the pulsar magnetosphere, is the Vlasov–Maxwell system of equations (e.g., Lifshitz & Pitaevskii 1981). It describes a self-consistent evolution of the distribution function of every particle species, coupled through the electromagnetic fields that are sourced by plasma currents. Because continuum kinetic equations are formulated for the distribution function in the six-dimensional phase space,  $f(\mathbf{r}, \mathbf{p})$ , their numerical solution is challenging. A simpler method is to use the representation of plasma with a fixed number of charged particles, called macroparticles or superparticles, known as the particle-in-cell (PIC) method<sup>10</sup> (Dawson 1983). Each simulated macroparticle represents a large number of real particles that would be following approximately the same path in phase space. The macroparticles move in the discretized grid under the action of the Lorentz force. Currents imposed by this motion are deposited in every cell on the grid and used as sources to solve Maxwell's equations. The updated electromagnetic fields are then extrapolated to the position of macroparticles to evaluate the Lorentz force for the next time step. This method presents the most fundamental way to computationally study plasma physics. In contrast to fluid approximations, this method makes no simplifying approximations at microscales, i.e., plasma skin depth,  $d_e = c/\omega_p$ , where  $\omega_p$  is the plasma frequency, and particle Larmor radius,  $r_L = v_\perp/\omega_B$ , where  $v_\perp$  is the component of the particle velocity transverse to the magnetic field, and  $\omega_B = eB/(m_e c \gamma)$  is the gyrofrequency of relativistic pairs. This technique has been successfully applied to understand physics of collisionless shocks, magnetic reconnection, and various plasma instabilities (e.g., Hoshino et al. 1992, Sironi & Spitkovsky 2014, Riquelme et al. 2015).

**PIC:** particle-in-cell

In contrast to local studies of these fundamental plasma physics phenomena, PIC simulations of pulsars must be truly global; i.e., they must include the full magnetosphere in the simulation domain. The current sheet, where the multiwavelength high-energy emission likely originates, cannot be studied in isolation from the rest of the magnetosphere. This is because various regions in the magnetosphere are intrinsically connected. For example, the current sheet is fed by the pair plasma from the discharge near the polar cap, whereas the dynamics of the discharge is regulated by the global current that is set by the magnetospheric structure close to the light cylinder, which in itself depends on the current sheet physics. In addition to the dynamics of plasma in the magnetosphere, PIC pulsar simulations need to model a number of other physical processes. These include the free escape of particles from the surface, emission and propagation of energetic gamma-ray photons, their feedback on energetic particles (radiation reaction force), pair production, and effects of GR. We summarize the simulation technology in **Supplemental Text Section 1**.

As is typical for astrophysical simulations, global PIC simulations of pulsar magnetospheres (and multidimensional local simulations of discharges and reconnection) are limited to a significantly rescaled version of the problem. The important length scales are the neutron star radius,  $R_* \sim 12$  km, the plasma skin depth calculated for the Goldreich–Julian density at the stellar surface,  $d_e = c/\sqrt{2\Omega\omega_B} \sim 1$  cm ( $B_*/10^{12}$  G) $^{-1/2}$ ( $P/0.1$  s) $^{1/2}$ , and the size of the light cylinder,  $R_{LC} = c/\Omega \approx 4,774$  km ( $P/0.1$  s). The Larmor radii of particles is completely negligible in the bulk of the magnetosphere (outside of the magnetospheric current sheet) due to the enormous strength of

**Supplemental Material >**

<sup>10</sup>The PIC method is a numerical technique for studying the dynamics of collisionless plasmas. In PIC simulations, electromagnetic fields are evolved on a fixed computational grid, whereas plasma distribution function is represented by an ensemble of moving particles.

the magnetic field, and a guiding center approximation can be employed (Bacchini et al. 2020). For example, the full potential drop across the polar cap can be expressed through dimensionless ratios of these scales,  $\gamma_{\text{PC}} \sim (1/4)(R_*/R_{\text{LC}})(R_*/d_e)^2 \sim 10^{10}(B_*/10^{12} \text{ G})(P/0.1 \text{ s})^{-2}$ . Pair production and radiation processes add additional energy scales, mainly, the threshold energy,  $\gamma_{\text{th}} \sim 10^7$ , at which the high-energy particles start to radiate pair-producing curvature photons, and the energies of secondary particles,  $\gamma_{\text{sec}} \sim 10^2$ , such that  $\gamma_{\text{sec}} \ll \gamma_{\text{th}} \ll \gamma_{\text{PC}}$ . Due to the limitation of the necessity to resolve the skin depth close to the stellar surface on the simulation grid, while still having a healthy separation of scales respecting the hierarchy in the pulsar problem,  $d_e \ll R_* \ll R_{\text{LC}}$ , 3D simulations are limited to  $(R_{\text{LC}}/d_e) \lesssim 500$  and  $(R_{\text{LC}}/R_*) \lesssim \text{few}$ . This leads to the energy scale ordering of  $\gamma_{\text{PC}} \sim 10^3$ ,  $\gamma_{\text{th}} \sim \text{few} \times 10$ , and  $\gamma_{\text{sec}} \sim \text{few}$ . Importantly, both the scale and energy hierarchies of real pulsars are respected by the PIC simulations. Whereas, as numerous simulation results indicate, the magnetospheric structure shows little dependence on the ratio  $R_{\text{LC}}/R_*$  as long as it is above approximately a few, the dependence on microscales is less trivial. Thus, interpreting pulsar observations in light of PIC simulations requires a nontrivial extrapolation, and not all aspects of this rescaling have been examined yet. Nonetheless, as the discussion in the following sections shows, modern kinetic simulations offer tremendous new insight into pulsar magnetospheres. What is the self-consistent structure of the pulsar magnetosphere? Where and how does the polar cap discharge operate? Where are the particle acceleration sights in the outer magnetosphere? Where and how is the high-energy emission produced? PIC simulations address all these long-standing questions from first principles.

### 4.3. Ghost: The Disk-Dome Solution

Before we describe the magnetospheric structure including the physics of pair production, it is instructive to consider the solution under the original assumptions of Goldreich & Julian, i.e., the free escape of particles, both electrons and ions, from the neutron star surface, and no pair creation. With these assumptions, Krause-Polstorff & Michel (1985) have identified a ghost behind the elegant picture by discovering a completely different magnetospheric solution. The qualitative picture here is as follows: In vacuum, and for an initially uncharged conductor with a dipolar field, the unipolar induction generates a quadrupolar electric field in the magnetosphere. Just above the stellar surface, the accelerating component of the electric field,  $E_{\parallel}$ , points inward at all latitudes (as described in Section 2). If both signs of charge are injected just above the surface and are available for the extraction, this electric field pulls electrons outward and pushes ions toward the star, for the case of aligned magnetic dipole moment and rotational axis. As a result, the star charges up positively, and a monopolar field of the central charge starts to pull out ions in the equatorial region. Once the charged particles populate the magnetosphere, they provide enough charge to start screening the accelerating electric field, until it becomes zero at the stellar surface,  $\mathbf{E} \cdot \mathbf{B} = 0$ . At this point, the surface injection stops and the magnetosphere reaches a steady state. In this state, and near the stellar surface, the charge density is close to the Goldreich-Julian density,  $\rho \sim \rho_{\text{GJ}} \sim \Omega B_*(1 - 3\cos^2\theta)/4\pi c$ , which changes its sign at the so-called null surface,  $\cos\theta = 1/\sqrt{3}$ . The polar region, called the dome, contains electrons. They are extracted by the residual of the quadrupolar electric field at the stellar surface and are attracted back toward the star further away by the monopolar field of the central charge. The equatorial disk contains trapped ions. The resulting charge density structure obtained from a 3D PIC simulation is shown in **Figure 5a**. The total extent of the charged clouds is about a few stellar radii. In contrast to the Goldreich-Julian picture and numerical FFE solutions, the disk-dome configuration produces neither significant magnetospheric current nor the expected Poynting flux-dominated outflow.

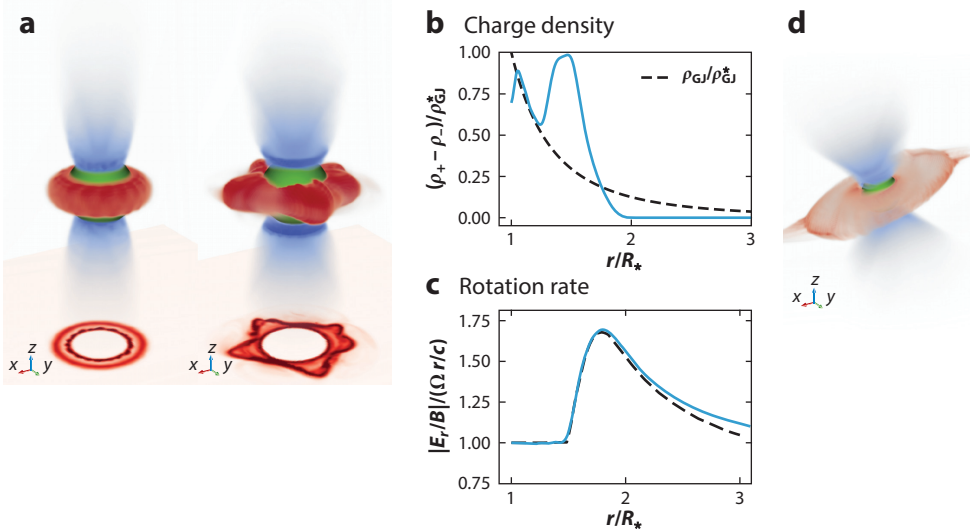


**Figure 5**

The disk-dome solution from a particle-in-cell simulation. (a) Volume rendering and equatorial slices of the charge density in the aligned magnetosphere, before and during the onset of the diocotron instability. (b,c) Comparison of the charge density and rotation rate profiles in the equatorial plane with analytical solutions by Pétri et al. (2002). (d) Volume rendering of the charge density in the 30-deg-inclined magnetosphere. This figure was provided by H. Hakobyan.

The resulting configuration is, however, unstable (e.g., Spitkovsky & Arons 2002), because the equatorial ion disk rotates differentially. This is because some field lines, which thread the disk, also pass through the vacuum region between the dome and the disk, so they are not equipotentials. As a result, the  $\mathbf{E} \times \mathbf{B}$  velocity is different on these field lines (see Figure 5 for the result of a 3D simulation with the *Tristan-MP v2* code<sup>11</sup> and a comparison with the analytical model by Pétri et al. 2002). Differential rotation seeds a shearing instability, known as diocteron instability in the case of a nonneutral plasma (Davidson 1990). This instability is intrinsically three-dimensional as it grows nonaxisymmetric modes. The growth rate of this instability for pulsar conditions,  $\omega_b^2/\omega_p^2 \gg 1$ , and a trapped plasma in the disk with a density of the order of the Goldreich–Julian density, is comparable to a rotational period. The instability leads to nonaxisymmetric modulations of the charge density and an outward transport of charge across the poloidal magnetic field lines (see Figure 5a for the equatorial slice of the charge density), due to the perturbed  $\mathbf{E} \times \mathbf{B}$  drift. However, though some equatorial charges reach the light cylinder, the current flow is insufficient to significantly modify the dipole magnetic field structure. This picture remains qualitatively the same in the case of oblique rotators, as shown in Figure 5d for the case of the 30-deg-inclined rotator. Although the parallel electric field,  $\mathbf{E} \cdot \mathbf{B}$ , is fully screened at the stellar surface, large accelerating gaps exist in the vacuum regions between the domes and the disk, together with an extended region of  $E > B$  at large cylindrical radii away from the star. These features are the consequence of the charge-separated nature of the solution. The disk-dome configuration is a likely state of every neutron star below the death line (a “dead” pulsar), which is not capable of actively producing  $e^\pm$  pairs in the polar discharge.

<sup>11</sup>Available at <https://github.com/PrincetonUniversity/tristan-mp-v2>.

**Magnetization parameter,  $\sigma_{LC}$ :** ratio of the magnetic energy density to the rest mass energy density of the plasma at the light cylinder

## 4.4. Magnetospheric Structure with Pair Production

The analysis of the Goldreich–Julian pulsar, which results in a charge-separated configuration of the magnetosphere, concludes that an active pulsar requires pair production. We first review the magnetospheres of young pulsars, with direct applicability to rapidly rotating pulsars like the Crab and most known gamma-ray pulsars. They sustain active pair production both in the polar cap and in the outer magnetosphere. We then discuss magnetospheres of older pulsars for which pair formation is possible only close to the star.

**4.4.1. Solutions with active pair production in the outer magnetosphere.** Philippov & Spitkovsky (2014) were the first to use a 3D PIC simulation of an aligned rotator to show that abundant pair supply everywhere in the magnetosphere does lead to an FFE-like solution, with a comparable Poynting flux and a Y-shaped current sheet. Their simulations also showed that magnetic reconnection in the current sheet beyond the light cylinder leads to a significant particle energization, up to  $\gamma \sim \sigma_{LC} = B_{LC}^2 / 4\pi nm_e c^2 \sim \gamma_{PC}/\lambda$ , where  $\lambda$  is the multiplicity of the flow in the upstream of the current sheet, and  $\gamma_{PC}$  is the particle Lorentz factor corresponding to the full potential drop across the polar cap. Hereafter,  $\sigma_{LC}$  is a magnetization parameter near the current sheet and close to the light cylinder, an important parameter which defines the available magnetic energy per particle.

Chen & Beloborodov (2014) were the first to include simplified physics of pair production both in the polar discharge, where the photon mean free path is short,  $l_{mfp} < R_*$ , and in the outer magnetosphere, where  $l_{mfp} \sim R_{LC}$ , into an axisymmetric simulation of an aligned rotator. When both pair creation channels were activated, they found a state resembling the FFE solution. Consistent with the expectations from the FFE model, the polar discharge was activated only in the separatrix return current layer, where  $\alpha < 0$  demands active pair production, whereas the sub-GJ current in the bulk of the polar cap,  $0 < \alpha < 1$ , did not lead to any significant acceleration of particles extracted from the surface. The charge-separated outflow on these field lines extended to infinity. Simulations showed that most of the particle acceleration, high-energy photon emission, and pair production happen in the Y-shaped current sheet, within and beyond the light cylinder.

Philippov et al. (2015b) performed simulations of oblique rotators with a prescribed particle energy threshold,  $\gamma_{th}$ , for the on-the-spot pair production. Solutions with inclinations of  $\lesssim 40$  deg were found to be qualitatively similar to the aligned rotator: They did not show pair production in the bulk of the open field line region, where  $0 < \alpha < 1$ . The field lines in this zone sustained a charge-separated outflow, and pair formation happened in the current sheet and return current layer only. Solutions with higher inclinations showed pair production in the open field line region with  $\alpha > 1$ , and a high density  $e^\pm$ -pair outflow. Here, the accelerating voltage fluctuated around the value set by the pair-production threshold. The size of the pair-producing region increased with inclination. At the time, the lack of polar cap activity at low inclinations was thought to be problematic for explaining the “core” component of the observed radio emission (see Section 5.2.3), which is usually considered to originate in the pair outflow from the bulk of the open field line region.

Philippov et al. (2015a) resolved this puzzle by including the GR frame-dragging effect into the simulations with a  $\gamma_{th}$ -based prescription for pair production. As described in Section 3.2.2, frame dragging decreases the Goldreich–Julian charge density near the star, whereas the current density demanded by the global magnetosphere is set by the twist of the field lines at the light cylinder and remains the same as in the flat spacetime solution. Quantitatively, one finds  $\alpha = \alpha_{\text{flat}}/(1 - 2C/5) > \alpha_{\text{flat}}$ . Although this correction leads to an increase of  $\alpha$  of only  $\sim 20\text{--}30\%$ , even for the case of the aligned rotator,  $\alpha_{\text{flat}}$  is quite close to unity near the magnetic axis. Thus, part of the region with  $0 < \alpha < 1$  easily becomes  $\alpha > 1$  when the frame dragging is included.

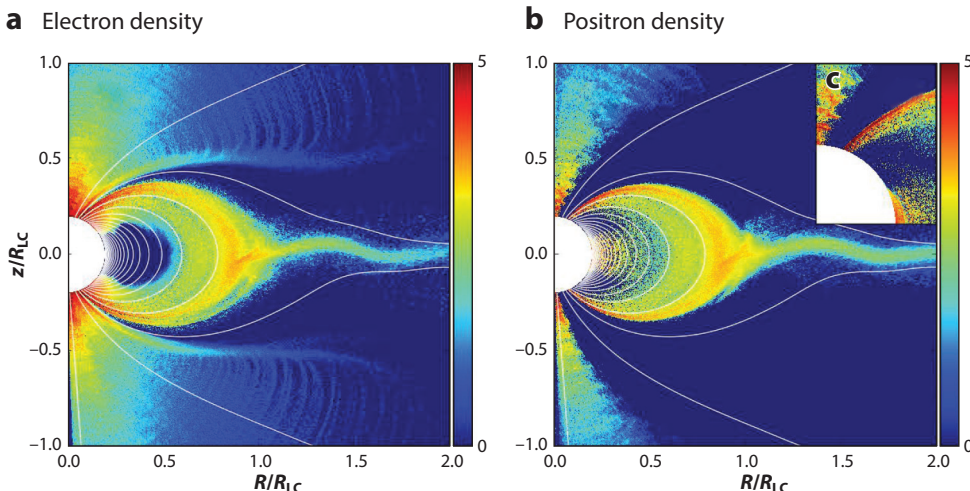


**Figure 6**

Aligned pulsar magnetosphere with the inclusion of frame-dragging effects; from particle-in-cell simulations in Philippov et al. (2015a). Color represents plasma densities on the logarithmic scale, normalized to Goldreich–Julian density at the pole. (a) Electron density; (b) positron density; (c) zoom-in view of the positron density close to the star. Figure adapted from Philippov et al. (2015a).

Indeed, GR simulations show activation of pair production on field lines close to the magnetic pole, as shown in **Figure 6**. We note that the frame-dragging effect is important for pair production in the core of the open field line region but not in the return layer, where  $|j_{\parallel}|/\rho_{GJ}c \gg 1$ . **Figure 6c** shows the positron distribution near the stellar surface, which identifies the nonstationary behavior of pair production in the polar cap. Pair plasma produced in the active phase of the discharge gets polarized and screens the accelerating component of the electric field,  $E_{\parallel}$ , inhibiting the pair formation. As the pair cloud leaves the gap region, the accelerating voltage is restored, and the cycle repeats. The timescale for this intermittency is slightly longer than the light-crossing time of the gap,  $l_{\text{gap}}/c$ , i.e., microseconds, where  $l_{\text{gap}}$  is the gap height (see Equation 7 for the estimate of  $l_{\text{gap}}$ ). Such variability, if reflected in the radio emission (see Section 5.4.3 for the discussion of the mechanism associated with a nonstationary discharge), might be the origin of the microstructure in the radio emission (Ruderman & Sutherland 1975). As Timokhin & Arons (2013) first showed with the 1D electrostatic discharge simulations, intermittency is a generic feature of pulsar pair cascades as the plasma flow adjusts to the current density demanded by the global magnetosphere.

Philippov & Spitkovsky (2018) extended these studies to inclined rotators, also including the finite mean free path of photons in the outer magnetosphere. Simulation also marked positive charges extracted from the surface as ions, which had the same charge and mass as positrons, except they were not radiatively cooled and did not emit pair-producing photons. A steady-state distribution of plasma and photon densities of the 60-deg rotator is shown in **Figure 7**. Compared to flat space solutions, the inclusion of GR effects increases the number of pair-producing field lines on the polar cap. The closed zone is not entirely charge separated. Some field lines are dominated by ions (**Figure 7d**; in the aligned rotator these field lines correspond to the ones near the magnetic equator; see **Figure 6**, where ions were included in the positron density). These ions are extracted from the star with small momentum and travel along the field line until they hit the star. Ions are also pulled off the surface in the separatrix layer, where they carry a substantial

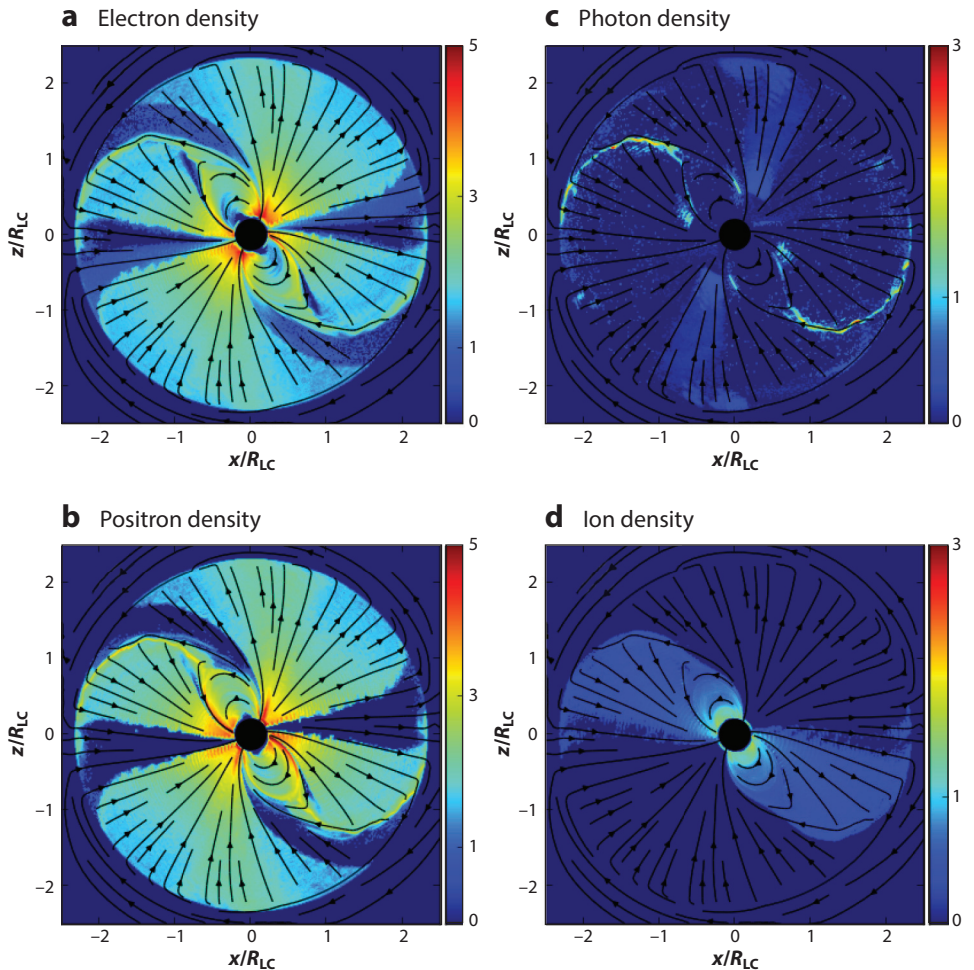


**Figure 7**

Slice through the  $\mu$ - $\Omega$  plane for the 60-deg-inclined pulsar magnetosphere. (a) Electron density, (b) positron density, (c) photon density, and (d) ion density. All densities are normalized by  $\Omega B / 2\pi ec$ . Black lines show poloidal magnetic field lines. Figure adapted from Philippov & Spitkovsky (2018).

amount of current (see also Chen & Beloborodov 2014).<sup>12</sup> Pair plasma is observed on some of the closed field lines (in the aligned rotator these field lines correspond to the ones extracting electrons at the stellar surface, above the “null” surface; see Figure 6). These pairs are produced by photons emitted in the current sheet near the Y-point and get trapped in the closed zone.

The solution for low obliquity angles and small mean free path of photons, similar to the aligned solution in Figure 6, shows a density gap above the current sheet, which coincides with

<sup>12</sup>The return current layer has an overall interesting and complicated phase space dynamics (see Philippov & Spitkovsky 2018, their figure 4c). In addition to the outflowing ions, there are energetic auroral electrons, pushed toward the star by the electric field at the Y-point, and dense pair flows both from the surface and from the Y-point region. This counter-streaming distribution may (or may not!) be interesting for modeling the coherent emission from the outer magnetosphere.

the open field lines passing through the “outer gap,” a surface where  $\rho_{\text{GJ}} = 0$ . The finite mean free path of photons emitted by energetic particles in strong current layers leads to an injection of pairs on these field lines. The amount of produced pairs, which is significantly lower compared to the dense polar outflow and current layers, can be enough to fully screen the electric field in the outer gap. For the case in which the pair injection in this region is not sufficient, for example, due to the large mean free path of photons, the observed particle acceleration in the outer gap region is much less efficient than in the Y-shaped current sheet. Regardless of whether the electric field in the outer gap region is fully screened or not, the magnetospheric current and available voltage across the outer gap are small and do not lead to any significant dissipation of the outgoing Poynting flux to explain the observed high radiative efficiencies of gamma-ray pulsars.

The Y-shaped current sheet produces most of the high-energy photons. Simulations show that for low obliquities,  $\chi < 30$  deg, the separatrix layer inside the light cylinder is an efficient photon emitter (see Chen & Beloborodov 2014, their figure 4, for the aligned rotator, and Philippov & Spitkovsky 2018, their figure 2, for the 30-deg-inclined case). However, for all inclinations, the current sheet beyond the Y-point is the most significant source of high-energy photons (and pairs) in the outer magnetosphere (the distribution of photons in the magnetosphere of the 60-deg rotator is shown in **Figure 7c**). This conclusion is expected to strengthen for realistic pulsar parameters. The reason is that the dissipation along the separatrix is caused by finite  $E_{\parallel}$ , which is induced as the plasma tries to provide the high current density in the thin separatrix layer as required by the global magnetosphere. As pair creation becomes significantly easier for realistic parameters of pulsars, the pair density increases, and the dissipation inside the light cylinder is expected to be significantly smaller. Indeed, high-resolution axisymmetric simulations for highest available values,  $\gamma_{\text{PC}} = 10^4$ ,  $\gamma_{\text{th}} = 10^2$ , show little dissipation within the light cylinder (Hu & Beloborodov 2021).

The amount of the Poynting flux dissipated in the current sheet beyond the light cylinder inside the sphere of  $2R_{\text{LC}}$ ,  $\Delta L$ , normalized to the total amount of the Poynting flux at the star,  $L_*$ , is  $\Delta L/L_* \approx 15\%$  for the aligned rotator (Chen & Beloborodov 2014, Philippov & Spitkovsky 2014, Philippov et al. 2015a). This amount decreases for higher obliquities and reaches  $\approx 2\%$  for the orthogonal rotator (e.g., Philippov et al. 2015b). Compared to the artificial dissipation due to regularization of the current in the FFE models, in PIC simulations this energy is self-consistently transferred to plasma particles. Because the radiative cooling time in the pulsar current sheet is short, most of this dissipated energy is radiated as high-energy photons. The radiative efficiencies,  $L_y/L_* \approx 1\text{--}10\%$ , observed in the simulations are broadly consistent with the observations made by *Fermi*.

The dissipation in the equatorial current sheet is typically reported to be split between the localized dissipation very close to the Y-point and a more gradual dissipation beyond it. The localized Y-point dissipation is most pronounced in axisymmetric simulations (e.g., Belyaev 2015, Hu & Beloborodov 2021). It is likely caused by the fact that the magnetospheric return current crosses magnetic field lines in a diffusion region near the Y-point in order to connect to the equatorial current sheet (see also Contopoulos 2019 and Contopoulos & Stefanou 2019). This effect creates a  $\mathbf{J} \times \mathbf{B}_{\text{pol}}$  torque in the toroidal direction, pushing the bulk of the plasma to high rotation rates (Hu & Beloborodov 2021). It remains to be seen how significant this dissipation is for larger pair multiplicities. The latter should lead to significantly smaller widths of the return current layers,  $\sim B_\phi/(n_e e)$ , where  $B_\phi \sim I/(cR_{\text{LC}})$  is the toroidal field at the light cylinder, and smaller volume of the diffusion region. The dissipation beyond the Y-point is due to magnetic reconnection. Because all magnetic field components change their sign beyond the light cylinder, the current sheet becomes unstable to tearing and plasmoid instabilities, which cause the field lines to spontaneously reconnect and release the magnetic field energy into the heating and acceleration

**Reconnection rate:**  
the rate of the transfer  
of magnetic flux  
toward the  
reconnecting current  
sheet

of the plasma. This process leads to the continuous formation and ejection of magnetic flux ropes (called plasmoids in 2D) and breathing, which is to say, inward and outward motion of the Y-point from the stationary position near the LC.<sup>13</sup> This dissipation should remain finite when the sheet width, which scales as the Larmor radius of reconnection-heated particles, becomes smaller for the larger separation of scales. This is because the rate at which opposite magnetic fluxes are advected into the layer, also called the reconnection rate (see Section 4.5.2), is not sensitive to scale separation. Even for realistic pulsar parameters,  $R_{LC}/d_e \sim 10^6$ , we expect a comparable amount of the Poynting flux to be dissipated in the current sheet beyond the Y-point.

**4.4.2. Solutions with pair production restricted to near the surface.** We now discuss older pulsars that do not have enough opacity to produce  $e^\pm$  pairs in the outer magnetosphere through  $\gamma\text{-}\gamma$  photon collisions. Sufficiently far from the radio death line, they can still produce copious pairs through the single-photon conversion,  $\gamma+B$ , near the stellar surface. Early simulations, by Chen & Beloborodov (2014) and Philippov et al. (2015a), concluded that these pulsars do not sustain an active FFE-like solution, with the structure asymptotically approaching the disk-dome state. However, as we understand it now, this was caused by artificially small values of the ratio  $\eta = \gamma_{PC}/\gamma_{th}$ . Simulations are limited to study magnetospheres with  $\eta \lesssim 200$  (Section 4.2), which may put them artificially close to the death line. This ratio determines whether pair creation can be efficient, and large values of  $\eta$  in real pulsars indicate how easy it is to convert the polar cap voltage into pairs. The second important ratio,  $\zeta = \gamma_{th}/\gamma_{sec}$ , controls the multiplicity of the secondary plasma, as the primary particle with the Lorentz factor  $\gamma_{th}$  can convert its energy at most into an  $\sim\zeta$  amount of secondary pairs. All global simulations are conducted for  $\zeta \sim 5\text{--}20$ , which, if possible due to the available voltage, allows copious pair production. Chen et al. (2020) varied  $\eta$  in the range between 25 and 150 and found that magnetospheres with  $\eta \gtrsim 100$  in fact did approach an FFE-like state, with an amount of dissipation within  $2R_{LC}$  comparable to the solutions with possible pair production in the outer magnetosphere (see Figure 8).<sup>14</sup>

An important ingredient to sustain the return current as a part of the FFE solution is the charge cloud at the Y-point, which has an overall negative charge density.<sup>15</sup> Some of the electrons are drawn back toward the star from the Y-point to help support the return current. An important contribution comes from the electrons, which are sucked into the current sheet and pushed toward the star by the reconnection-driven electric field, circling around the Y-point for a sufficiently long time (Brambilla et al. 2018, Philippov & Spitkovsky 2018).

In simulations with a lower ratio of the total voltage to the pair production threshold,  $\eta \lesssim 100$ , but still allowing pair formation, the solution was found to be cyclic (Chen et al. 2020; see also the discussion in Philippov & Spitkovsky 2018). It shows oscillations between an active state with the Y-shaped current layer and a state with a nearly depleted separatrix layer, low Poynting flux, large unscreened vacuum gaps, and a large amount of dissipation, up to  $\Delta L/L_* \approx 25\%$  inside the

<sup>13</sup>The motion of the Y-point and associated current fluctuations are communicated to the surface in the form of Alfvén waves along the return current layer on a light-crossing timescale of the magnetosphere,  $\Omega^{-1}$ , a phenomenon that is observed also in 3D simulations (H. Hakobyan, A. Philippov, and A. Spitkovsky, in preparation). It remains to be seen whether these dynamics can be of interest to interpreting the microstructure of radio emission or stochasticity in the radio pulse arrival times, as suggested by, e.g., Arons (2009).

<sup>14</sup>These results agree with numerical experiments performed with a simplified prescription of a fixed amount of plasma being injected at the surface with a mildly relativistic outward velocity along the magnetic field (Cerutti et al. 2015, Belyaev 2017, Brambilla et al. 2018).

<sup>15</sup>It is significantly easier to sustain the required charge configuration with the active pair production in this region at similar values of  $\eta$ . In particular, the simulations of Chen & Beloborodov (2014) and Philippov et al. (2015b) discussed above were performed for  $\eta \approx 25$ .

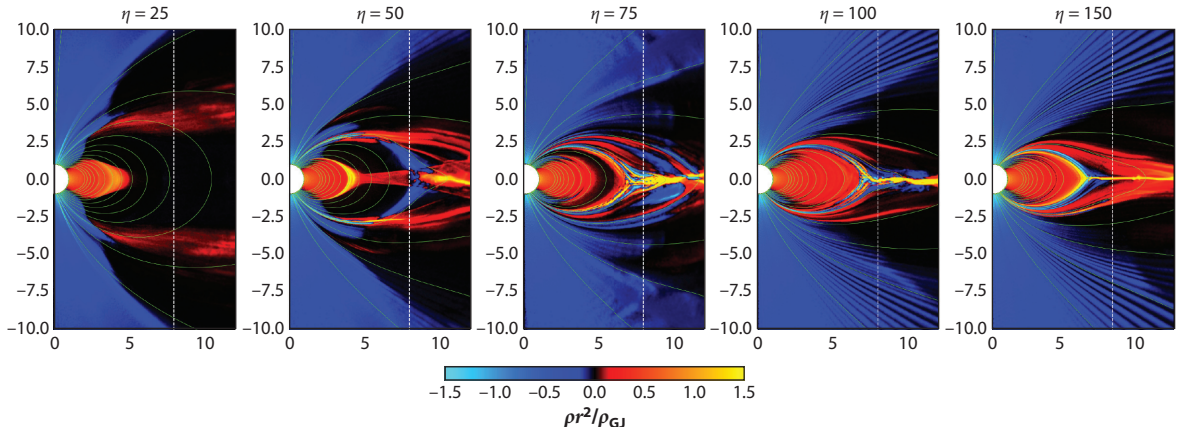


**Figure 8**

Structure of pulsar magnetosphere with pair production restricted to the pulsar surface, for various values of the parameter  $\eta = \gamma_{\text{PC}}/\gamma_{\text{th}}$ , showing activation of the force-free electrodynamics-like state at  $\eta \gtrsim 100$ . Color represents the charge density in the magnetosphere, multiplied by a factor of  $r^2$  and normalized to  $|\rho_{\text{GJ}}| = \Omega B_*/2\pi c$ . The vertical white dashed line is the light cylinder, and green curves are magnetic field lines. Figure adapted from Chen et al. (2020).

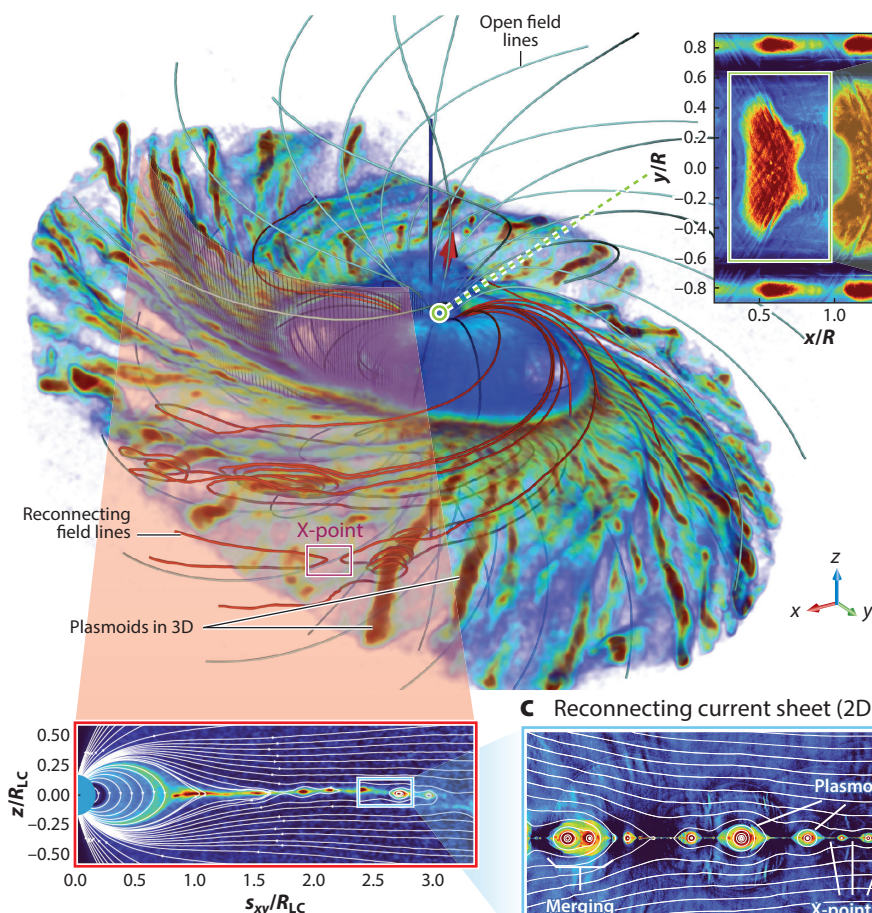
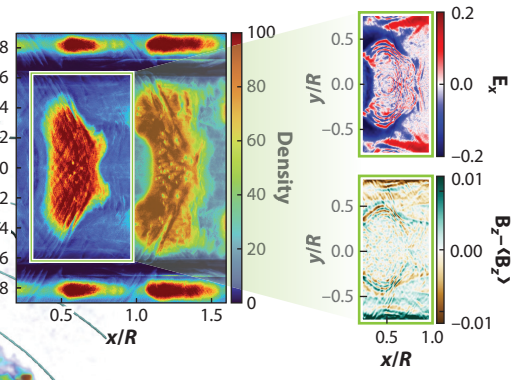
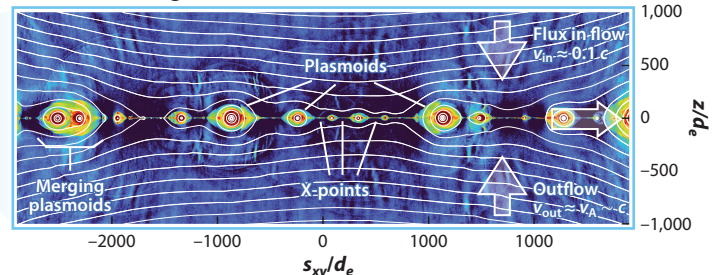
light cylinder. It is interesting to further investigate the periodicity of the magnetospheric cycles in these old-pulsar solutions, which cannot support large multiplicities in their pair cascades. In particular, it will be important to understand the scaling with  $\eta$  and  $\zeta$ , and the resulting pair multiplicity. These time-dependent dynamics are of potential interest to modeling the various observed “nulling” behavior in pulsar radio emission (see Section 5.2.3).

#### 4.5. Time-Dependent, Dynamic Regions in the Magnetosphere

As a result of the global magnetosphere modeling, two distinct regions emerge as major particle accelerators, where coherent radio emission and incoherent high-energy emission are likely to be produced. In the following section, we discuss the physics of the polar discharge and magnetic reconnection beyond the light cylinder, as well as their role in powering the observed pulsar activity. **Figure 9** summarizes the highly nonstationary behavior observed in global and local kinetic simulations of pair discharges and magnetic reconnection.

**4.5.1. Intermittent polar discharge.** The theory of the polar discharge with free escape of particles from the surface is best understood for young pulsars. In this case, the distance to accelerate particles up to the energies capable of emitting pair-producing photons in a nearly vacuum electric field, which is typical for time-dependent gaps, is much smaller than the polar cap size. For these conditions, the basics of the polar gap region can be described under the 1D approximation. We discuss the applicability of these assumptions below. The discussion in this section summarizes results by Timokhin & Arons (2013) and Timokhin & Harding (2015, 2019). For simplicity, we consider the case of an acute inclination angle below, which is to say  $\mathbf{\Omega} \cdot \mathbf{B}_* > 0$ , and  $\rho_{\text{GJ}} < 0$  in the whole polar cap for all inclinations angles not too close to orthogonal,  $\chi = 90$  deg.

As in early theories (e.g., Arons & Scharlemann 1979), the model describes the dynamics of a cold electron beam, initially at zero velocity,  $v = 0$ , which is extracted from the surface at  $x = 0$ , along the magnetic field line. The steady-state dynamics is governed by the equation of motion of the beam,  $v \cdot d(m_e \gamma v)/dx = eE_{||}$ , and Gauss’s law  $dE_{||}/dx = 4\pi(\rho - \rho_{\text{GJ}})$ , where  $e$  is the charge of the beam particles. The surface boundary conditions, assuming the beam starts nearly

**a** 3D PIC simulation of the global pulsar magnetosphere**d** Intermittent polar cap discharge (2D PIC)**c** Reconnecting current sheet (2D PIC)**b** Magnetic reconnection in the plasmoid unstable current sheet (slice from global 3D PIC)**Figure 9**

Time-dependent physics in the pulsar magnetosphere. (a) 3D PIC simulation of the global pulsar magnetosphere of the 30-deg-inclined rotator. The volume rendering shows the plasma density, gray thick lines represent open field lines, and red thick lines highlight magnetic field lines that go through the current sheet undergoing magnetic reconnection. The small magenta zoom box highlights an example X-point, where magnetic field lines break and reconnect. The dense structures in the current sheet correspond to 3D plasmoids, or flux ropes, with an example magnetic field line wrapping around the plasmoid shown right next to the X-point. (b) Slice through the 3D PIC simulation of the global pulsar magnetosphere of an aligned rotator, which shows the plasmoid unstable current sheet; for the ratio of the light cylinder to the plasma skin depth near the current sheet,  $R_{LC}/d_e \approx 150$ . The data for panels *a* and *b* are from H. Hakobyan, A. Philippov, and A. Spitkovsky, in preparation. (c) Local 2D PIC simulation of the reconnecting current sheet for  $L/d_e = 6,000$ , where  $L$  is the length of the current sheet. The color in panels *b* and *c* shows the plasma density, and thick white lines show magnetic field lines. The data for panel *c* are from Hakobyan et al. (2019). (d) Local 2D PIC simulation of the intermittent polar cap discharge. The color shows plasma density, and the zoom-in panels present the screening of the longitudinal electric field,  $E_x$ , and emission of the electromagnetic O-mode waves, which are shown in the  $B_z$  component of the magnetic field. The data for the plot in panel *d* are from Philippov et al. (2020). This figure was provided by H. Hakobyan. Abbreviation: PIC, particle-in-cell.

at rest and the electric field is screened in the atmosphere, are  $v = v_0 \ll c$  and  $E_{\parallel} = 0$ . The major difference compared to early models is that the magnetospheric current is an input parameter to the discharge theory and is determined by the overall structure of the magnetosphere—a behavior that has been confirmed by global PIC simulations, as we described in Section 4.4. This is because on the timescales typical for the discharge zone, of order or less than the light-crossing time of the polar cap (microseconds), the magnetospheric twist,  $j_m = c(|\nabla_{\parallel} \times \mathbf{B}|/4\pi)$ , is stationary. It can only change on timescales comparable with the light-crossing time of the light cylinder, i.e., tens to hundreds of milliseconds. Mathematically, this results in the following form of the induction equation,  $\partial E_{\parallel}/\partial t \approx -4\pi(j_{\parallel} - j_m)$ , which in 1D is purely electrostatic.<sup>16</sup> In a steady-state charge-separated beam solution, this equation pins down  $j_{\parallel} = \rho v = j_m$ .

The dynamics of the discharge is controlled by the dimensionless quantity  $\alpha = j_m/(\rho_{GJ}c)$  (Mestel et al. 1985, Beloborodov 2008, Timokhin & Arons 2013). In cases with  $0 < \alpha < 1$  and  $\alpha > 1$ , the electron beam starts at a very high density,  $\rho/\rho_{GJ} \gg 1$ , which is essential to conduct the required current at nearly zero velocity near the surface, where  $E_{\parallel} = 0$ . The effective charge density in this region,  $\rho - \rho_{GJ}$ , is negative and, according to Gauss's law, the magnitude of the inward directed electric field, which accelerates electrons outward, decreases. If the current density is super-Goldreich-Julian,  $\alpha > 1$ , the ratio of the beam charge density and  $\rho_{GJ}$  never drops below unity,  $\rho/\rho_{GJ} = j_m/(v\rho_{GJ}) > \alpha > 1$ ; thus, the electric field is monotonically decreasing, and the electron beam acceleration continues up to infinity. The total voltage in the charge-separated gap with  $\alpha \approx \text{constant} > 1$  is huge, namely of the order of the vacuum potential,  $\Phi \sim b^2(\rho - \rho_{GJ}) \approx b^2\rho_{GJ}(\alpha - 1)$ , where  $b$  is the gap height. This is in contrast to steady-state gap models with the free escape of particles with  $j_m \simeq j_{GJ}$ , where the voltage is regulated by small differences between  $\rho$  and  $\rho_{GJ}$ . In the case of sub-Goldreich-Julian current,  $0 < \alpha < 1$ , electrons accelerate until they can carry the current with the lower density,  $\rho/\rho_{GJ} = \alpha c/v < 1$  for  $v/c > \alpha$ , at which point the electric field weakens and eventually changes sign. It decelerates electrons, until zero velocity, and then the cycle repeats. In this region, the particles can accelerate only to slightly relativistic velocities,  $\leq p_{\max} = 2\alpha/(1 - \alpha^2)$ , unable to emit pair-producing photons. Kinetic simulations show that the oscillating cold flow is unstable, with the resulting state being an outward-propagating electron beam with velocity  $\simeq p_{\max}$ , and a low-energy quasi-thermal cloud of electrons trapped in low-amplitude electrostatic fluctuations (see **Figure 10**). The power in these oscillations,  $\lesssim 10^{-10}L_0$ , is too small to explain the observed radio emission produced in the open field line region. To conclude, for the open field lines carrying a sub-Goldreich-Julian current, the outflow consisting of just low-energy electrons extends to infinity. As described in Section 4.4, this picture has been reproduced in global simulations.

Because polar cap zones with  $\alpha > 1$  show large acceleration of the extracted electron beam, they are efficient sources of high-energy curvature radiation and pair production. First-principles 1D PIC simulations, performed for realistic parameters, show that pair formation is highly intermittent (Timokhin & Arons 2013): Episodes of particles accelerated to ultrarelativistic energies and efficient pair production are followed by a quiet phase when fresh plasma screens the electric field. As pairs leave the accelerating zone, they flow along the open field lines into the magnetosphere. When the density of the pair plasma drops below the minimum density necessary to satisfy  $j = j_m$  and  $\rho = \rho_{GJ}$  (thus, failing to screen the electric field), a gap appears, and the cycle repeats. The intermittency of pair production is similar to the case with no particle escape from

<sup>16</sup>In multiple dimensions, the induced variations in the magnetic field that accompany variable  $E_{\parallel}$  do not appear to affect the particle acceleration and discharge dynamics. This has been recently probed directly in 2D discharge simulations by Philippov et al. (2020). We note that despite this sounding negligibility, these fluctuations can power the observed coherent radio emission, as we discuss in Section 5.4.

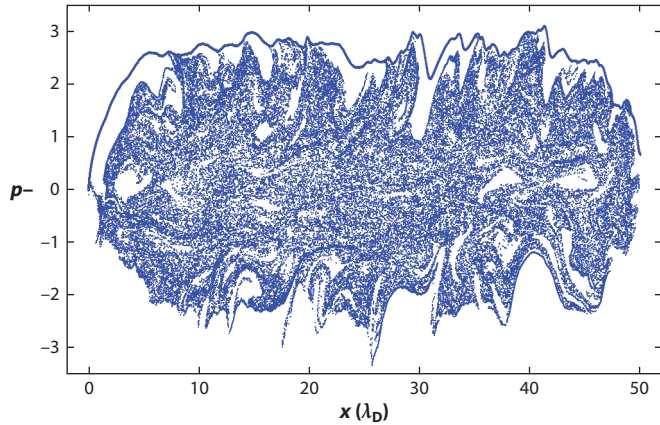


**Figure 10**

Plasma phase space along the magnetic field line in the 1D simulation of the sub-Goldreich-Julian current,  $0 < \alpha < 1$ . Blue dots correspond to electrons. The distance along the field line is measured in units of  $c/\omega_p^{\text{GJ}}$ . This figure was provided by A. Timokhin.

the surface described by Ruderman & Sutherland (1975), though the gap dynamics is different from that of the original model.

Acceleration of primary particles stops when pairs start to be produced and the electric field gets screened.  $E_{\parallel}$  in the gap increases linearly with distance,  $l$ , and, because curvature radiation reaction force is negligible in gaps of young pulsars (Timokhin & Harding 2015), the particle energy grows as  $l^2$ . For every beam particle, the distance it travels in the unscreened electric field is a sum of the acceleration distance,  $l_e$ , to reach energies capable of emitting pair-producing curvature photons and a photon mean free path,  $l_{\gamma}$ . The larger the distance the particle travels experiencing the unscreened electric field, the higher the particle energy and the energy of curvature photons it emits and the smaller the distance traveled by the photon until it gets absorbed in the strong magnetic field. The gap size,  $l_{\text{gap}}$ , is the minimum value of  $l_e + l_{\gamma}$  over the energy of the accelerated particle, because the electric field is quickly screened after the first pairs are produced. Timokhin & Harding (2015) show a result very similar to that of Ruderman & Sutherland (1975):

$$l_{\text{gap}} \simeq 0.7 \times 10^4 \chi_a^{1/7} \xi_j^{-3/7} \left( \frac{\rho_c}{10^7 \text{ cm}} \right)^{2/7} \left( \frac{P}{0.1 \text{ s}} \right)^{3/7} \left( \frac{B_*}{10^{12} \text{ G}} \right)^{-4/7} \text{ cm}. \quad 7.$$

Here,  $\chi_a \sim 0.1$  denotes the value of the quantum  $\chi_{\gamma}$  parameter<sup>17</sup> when the optical depth to pair production reaches 1. Furthermore,  $\xi_j = (j - j_m)(1 + c/v)/j_{\text{GJ}}^0$ , where  $j$  is the actual current density in the gap during the phase with the unscreened electric field,  $v$  is the velocity with which the gap moves as a whole, and  $j_{\text{GJ}}^0 = B_*/P$  is the Goldreich-Julian current density in the aligned rotator;  $\rho_c$  is the curvature radius of the magnetic field lines. The prefactor  $\xi_j$  determines whether the electric field in the gap is stronger or weaker compared to the vacuum gap in the aligned rotator, and  $\xi_j \simeq \text{const} \approx \text{few}$  is a good approximation. The maximum Lorentz factor of beam particles accelerated over  $l_{\text{gap}}$  is

$$\gamma_{\text{gap}} \simeq 7 \times 10^7 \chi_a^{2/7} \xi_j^{1/7} \left( \frac{\rho_c}{10^7 \text{ cm}} \right)^{4/7} \left( \frac{P}{0.1 \text{ s}} \right)^{-1/7} \left( \frac{B_*}{10^{12} \text{ G}} \right)^{-1/7}, \quad 8.$$

<sup>17</sup>Here,  $\chi_{\gamma} \sim (\epsilon_{\gamma}/m_e c^2)(B_{\perp}/B_Q)$ , where  $\epsilon_{\gamma}$  is the photon energy,  $B_{\perp}$  is the magnetic field component transverse to the direction of propagation, and  $B_Q$  is the Schwinger critical quantum field,  $B_Q \equiv m_e^2 c^3/e\hbar \approx 4.4 \times 10^{13} \text{ G}$ .

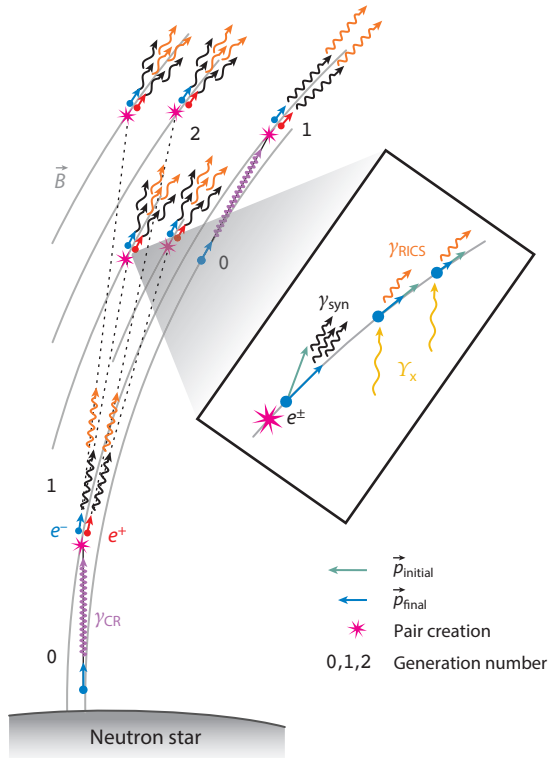


**Figure 11**

Pair cascade in the polar cap of a young pulsar with a high magnetic field strength. Annotations  $\gamma_{\text{CR}}$ ,  $\gamma_{\text{syn}}$ , and  $\gamma_{\text{RICS}}$  represent photons emitted through curvature, synchrotron, and resonant inverse Compton mechanisms, correspondingly. Figure adapted from Timokhin & Harding (2019).

where the only substantial dependence comes from the radius of curvature. The 1D approximation for the gap structure, which was assumed above, is valid for  $l_{\text{gap}} < R_{\text{pc}}$ . Using Equation 7, this condition takes the form  $\dot{P} > 4 \times 10^{-15} P^{1/4}$  and is satisfied in young pulsars with large  $\dot{P}$  (see Timokhin & Harding 2015, their appendix C). As mentioned above, Equations 7 and 8 are derived under the assumption of negligible particle radiative energy losses compared to the work done by the accelerating electric field, which is justified for most non-millisecond pulsars,  $B_* \gtrsim 10^{11}$  G (see Timokhin & Harding 2015, their appendix B).

Each curvature photon produced by an electron in the primary beam initiates a pair cascade with secondary particles emitting the next generation of pair-producing photons via synchrotron radiation and inverse Compton scattering<sup>18</sup> of soft X-ray photons from the neutron star surface (**Figure 11**). Because the electric field in the gap is screened early in the discharge, most of the secondary pairs do not accelerate to high enough energies to emit pair-producing curvature radiation photons. In contrast, as their Lorentz factors are not limited by the radiation losses, primary

<sup>18</sup>In the strong magnetic fields typical for pulsar polar caps, Compton scattering can occur in the resonant regime, when the photon energy in the electron's rest frame is equal to the cyclotron energy. Scattering in the nonresonant regime is not an efficient source of pair-producing photons. See Timokhin & Harding (2015, their appendix A).

particles continue to emit pair-producing curvature photons. These photons travel some distance before they produce pairs when the angle between their propagation and magnetic field direction becomes sufficient. The cascade initiated by a single curvature radiation photon stops at a generation at which the energy of synchrotron and inverse Compton photons emitted by secondary pairs falls below the threshold for pair formation. There are usually only 4–6 cascade generations. The high multiplicity is achieved because particles from all generations emit multiple pair-producing photons. The largest contribution is from generations 1–3, with generation 0 corresponding to the curvature photons emitted by primary particles. The final multiplicity is reached usually at distances comparable with the neutron star radius,  $r \sim R_*$ , which is substantially above the gap. Further away, the magnetic field is weaker, the energy of the primary beam particles decreases, and the pair production is not efficient because the opacity to the  $\gamma + B$  pair-production process becomes negligible.

Timokhin & Harding (2019) present detailed calculations of the cascade multiplicity. They show that the highest multiplicity is achieved for pulsars with hot,  $T > 10^6$  K, surfaces, when pair production by the inverse Compton photons adds a substantial contribution to the synchrotron photons. The maximum multiplicity is in the range of  $\lambda \sim 3 \times 10^5$ – $10^6$  for magnetic field strength of  $3 \times 10^{12}$ – $10^{13}$  G. For older pulsars, the surfaces of which have cooled down below  $10^6$  K, the density of soft photons at  $r \sim R_*$  is small, and the pair load is dominated by synchrotron photons. The maximum cascade multiplicity in this regime is approximately a few  $\times 10^5$  for  $B_* \sim 10^{12}$  G. The multiplicity is not very sensitive to pulsar parameters (period, magnetic field strength, and radius of curvature of the field lines). It varies by less than an order of magnitude for the range of pulsar parameters spanning two or more orders of magnitude. This is because in young pulsars the particle acceleration is efficiently regulated by pair creation: For pulsar parameters resulting in more efficient pair production, the size of the gap is smaller and the primary particle energy is lower and vice-versa. Timokhin & Harding (2015) present results for the spectrum of secondary pairs and the spectrum of escaping photons. They find that the secondary pair spectrum extends from  $\gamma \sim$  few up to  $\gamma \sim 10^4$ , with a peak at  $\gamma \sim$  few  $\times 10$  (Timokhin & Harding 2015, their figure 15). Their results show that the cutoff of the spectrum of escaping photons is around 10–100 MeV (Timokhin & Harding 2015, their figure 16), which is below or at the edge of the *Fermi* satellite's sensitivity limit. Observations with future instruments in the MeV band will be critical for verifying the predictions and serving as an overall test of the modern discharge theory.

The zone of  $\alpha < 0$ , i.e., the field lines carrying the return current, was also found to sustain cyclic pair production. Here, electrons are not extracted from the star, and all leptons are produced during the burst of pair formation. In contrast to the case of the super-Goldreich-Julian current, where the primary electrons extracted from the surface serve as the main cascade driver, the particles emitting the highest-energy curvature photons are the outgoing positrons, which are left in the gap from the previous burst. Simulations for the case of  $\alpha < -1$ , which corresponds to the separatrix current layer and volume return current in the nearly orthogonal rotator (see the example case of  $\chi = 85$  deg in **Figure 3**), show extraction of ions from the surface. This effect is also observed in global simulations (see Section 4.4.1). **Figure 12** summarizes the plasma and photon phase space behavior during the ignition of the discharge in cases  $\alpha < 0$  (**Figure 12a**) and  $\alpha > 1$  (**Figure 12b**).

It remains to be seen in detail how pair discharges operate in older pulsars, where the 1D approximation is inapplicable. Millisecond pulsars, where radiation reaction effects on primary particle acceleration and, potentially,  $\gamma$ - $\gamma$  pair production are important (Jones 2021), are particularly interesting. For a few of these pulsars, *Neutron star Interior Composition ExploreR Mission* (NICER) has recently provided high time-resolution observations of thermal X-ray hotspots produced by the bombardment of the stellar atmosphere by particles reversed toward the star in the

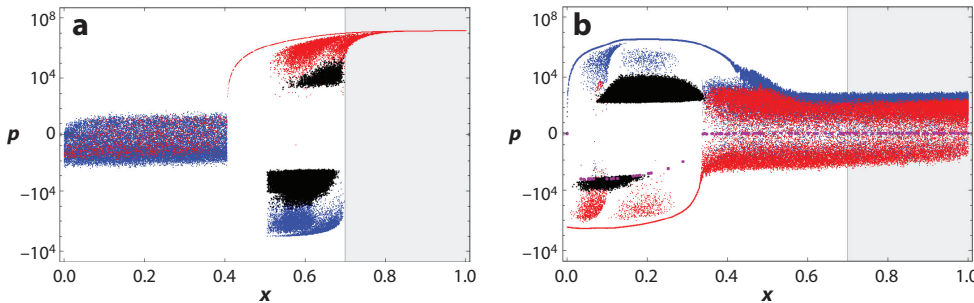


**Figure 12**

Dynamics of the plasma and photon phase space along the magnetic field line in the 1D discharge simulation. Blue, red, and black dots correspond to electrons, positrons, and photons, respectively.

(a) Anti-Goldreich-Julian current,  $\alpha < 0$ . (b) Super-Goldreich-Julian current,  $\alpha > 1$ . The distance along the field line in the panels is measured in the units of the neutron star radius. The gray shaded region indicates the zone where pair production is not allowed in the simulation. This figure was provided by A. Timokhin.

discharge (Miller et al. 2019, 2021; Riley et al. 2019, 2021). In nonstationary cascades, roughly an equal amount of energy is deposited into backward and outward-propagating plasma flows. The total thermal X-ray luminosity from the hotspot is proportional to the product of the potential drop,  $\propto \gamma_{\text{gap}}$ , and the total outflowing current,  $I$ . The luminosity per magnetic pole is then given by  $L_X = 0.5L_0(\gamma_{\text{gap}}/\gamma_{\text{pc}})$ . It has been known for a long time that the Ruderman-Sutherland-type gap substantially overproduces the total X-ray luminosity compared to observations (e.g., Arons 2009, Beskin 2018). The key to this discrepancy seems to be the strong intermittency of the cascades. The X-ray power is attenuated by the factor  $f = \tau_{\text{active}}/T$ , where  $\tau_{\text{active}}$  is the time during which the particle acceleration occurs, and  $T$  is the time between successive pair cascades. Depending on the value of  $\alpha$ ,  $f$  can be within the range of  $l_{\text{gap}}/R_{\text{NS}} \sim 10^{-2}$  to  $\sim 1/\text{few}$  (Timokhin & Harding 2015), which is sufficient to explain thermal X-ray observations (A.N. Timokhin, private communication).

**4.5.2. Reconnecting current sheet and its role in powering the high-energy emission.** Magnetic reconnection in collisionless plasmas is an old-standing fundamental problem with direct applications to fusion, solar flares, and various phenomena in astrophysics. Recent advances in theory and simulations show that in a nonlinear stage, reconnection is mediated by a hierarchical tearing, or “plasmoid,” instability in a broad range of physical conditions (see the review by Loureiro & Uzdensky 2016). A current sheet gets fragmented into a sequence of localized magnetic nulls, so-called X-points, and blob-like magnetized structures, “plasmoids” (see Figure 9). Plasmoids merge with each other, and their sizes extend from microscopic scales,  $\sim 10\rho_L$ , where  $\rho_L$  is the Larmor radius of heated particles in the current sheet, to macroscopic, “monster” plasmoids of sizes comparable with a fraction of the current sheet’s length,  $L$  (e.g., Sironi et al. 2016). The reconnection-driven electric field at the X-points leads to a drift of the background plasma with the velocity  $c(\mathbf{E} \times \mathbf{B})/B^2$ , known as the reconnection rate, into the current layer, and the inflow of fresh unconnected magnetic flux. In collisionless systems, the reconnection rate is comparable to  $0.1V_A$ , where  $V_A$  is the Alfvén speed above, in the “upstream” of, the current sheet. In collisional plasmas as described by the MHD equations with a scalar resistivity, the rate is found to be ten times lower,  $0.01V_A$  (Bhattacharjee et al. 2009, Uzdensky et al. 2010). In collisionless pair plasmas, the reconnection-driven electric field is produced by gradients of the anisotropic pressure tensor of pairs (Bessho & Bhattacharjee 2005). The picture of the plasmoid instability described above, however, is only applicable to large systems with very localized dissipation, which is to say, large

$\gamma_{\text{rad}}$ : critical particle's Lorentz factor, at which the recoil force exerted by radiation on the emitting particle, known as radiation reaction force, is comparable with the Lorentz force

Lundquist number collisional plasmas,  $S = LV_A/\eta \geq 10^4$ , where  $\eta$  is the resistivity of the plasma, or collisionless plasmas with a sufficient separation of scales,  $L/(c/\omega_p) \geq 10^2$ . We note that existing global MHD simulations of pulsar magnetospheres did not reach this regime yet because of the insufficient numerical resolution. Less stringent conditions in collisionless plasmas made it possible to observe the plasmoid instability in global PIC simulations (**Figure 9**).

In pulsars, the growth rate of the tearing instability at the light cylinder,  $\gamma_T$ , is very large compared to the pulsar rotation rate,  $\Omega$ ; i.e.,  $\gamma_T/\Omega \sim (1/\gamma_{\text{sec}})(R_{LC}/\delta') \gg 1$ , where  $\delta'$  is the width of the current layer in the comoving frame of the upstream plasma, so the above described picture is applicable. Reconnection proceeds in the relativistic regime, when the Alfvén speed in the upstream of the current sheet is close to the speed of light,  $V_A = c\sqrt{\sigma/(1+\sigma)} \approx c$ , where  $\sigma$  is the magnetization parameter in the upstream. This regime was recently studied with 2D and 3D PIC simulations (Guo et al. 2014, Sironi & Spitkovsky 2014). 3D simulations show that the plasmoid-mediated picture is directly applicable in relativistic pair plasmas, despite the growth of a competing drift-kink instability.<sup>19</sup>

Simulations show that relativistic reconnection is an efficient source of accelerated particles. Acceleration occurs in two steps: primary, by a nonideal electric field,  $E > B$ , at the X-point, and secondary, by a *Fermi*-type process in compressed growing plasmoids (in 2D; Petropoulou & Sironi 2018, Hakobyan et al. 2021) or by bouncing between converging upstream flows (in 3D; Zhang et al. 2021). The first process directly accelerates particles to energies of  $\gamma \approx \text{few} \times \sigma$ , which roughly corresponds to the potential drop across the X-point (Werner et al. 2016), whereas the second process can accelerate to much higher energies. Near the light cylinder of young pulsars, however, the strength of synchrotron cooling is large, such that radiative losses become significant at  $\gamma \sim \gamma_{\text{rad}} \sim \sigma_{LC}$ , where  $\gamma_{\text{rad}} = 10^5(B_{LC}/10^5 \text{ G})^{-1/2}$ , and secondary acceleration of pairs is not efficient. However, it can be important for the acceleration of ions extracted from the surface in the return current region (Philippov & Spitkovsky 2018, Guépin et al. 2020). Synchrotron cooling is suppressed at the X-points, because the magnetic field vanishes, so particles can be accelerated into a spectrum with a cutoff at  $\gamma \approx \text{few} \times \sigma$  even if cooling is strong,  $\gamma_{\text{rad}} \lesssim \sigma_{LC} \approx 10^6(B_{LC}/10^5 \text{ G})(\lambda/10^4)^{-1}(P/0.1 \text{ s})$  (e.g., Cerutti et al. 2013, Hakobyan et al. 2019). In this regime, called radiative reconnection (e.g., Uzdensky 2016), particles are accelerated in X-points, but radiate in plasmoids. Here, plasma particles quickly radiate a significant amount of their transverse momentum, i.e., pressure, which leads to a strong compression of the plasma to maintain the balance between the plasma and magnetic pressure across the current sheet. The resulting cross-layer pressure balance and the energy balance between reconnection-powered heating and synchrotron cooling fully set the plasma temperature, the width of the current sheet, and characteristic sizes of plasmoids (Lyubarskii 1996a, Uzdensky & Spitkovsky 2014).

Global 3D radiative PIC simulations are now used to construct light curves directly from photons produced by particles accelerated in the magnetospheric current sheet (Cerutti et al. 2016b, Kalapotharakos et al. 2018, Philippov & Spitkovsky 2018). As described above, all simulations show  $\sim 1\text{--}20\%$  efficiency of converting the Poynting flux into accelerated particles and a comparable efficiency, because of short cooling times, of radiating high-energy photons. The simulated high-energy light curves have a caustic nature (see discussion in Section 4.1) and typically have

<sup>19</sup>In some 2D axisymmetric simulations, which allow tearing instability of the  $B_r$  component but not of  $B_\phi$ , drift-kink saturates at large amplitudes owing to the small amount of the upstream plasma (see transverse wiggles of the current sheet in **Figure 6**). However, in 2D simulations with efficient pair loading (Hu & Beloborodov 2021) and 3D oblique rotator simulations (e.g., **Figure 9**; Philippov & Spitkovsky 2018, Cerutti et al. 2020), the plasmoid instability dominates. Simulations of Kalapotharakos et al. (2018) show a laminar current sheet, likely due to insufficiently large  $R_{LC}/d_e$ .

two pronounced peaks, in agreement with gamma-ray observations. Each peak appears when the equatorial current sheet crosses the observer's line of sight reflecting the geometrical origin of the caustic nature of the light curve.

The shapes of the spectra extracted from simulations resemble typical observations shown in **Figure 4**, i.e., a rising power law, due to a hard power law of accelerated particles,  $\gamma^{-\alpha}$ , where  $1 < \alpha < 2$ , and an exponential cutoff (Cerutti et al. 2016b, Philippov & Spitkovsky 2018). Because PIC simulations model a significantly down-scaled problem (see Section 4.2), extrapolation to realistic parameters is required, and many details of this rescaling are not understood yet. There are two leading competing scenarios for the radiation mechanism from the current sheet: synchrotron, i.e., particles radiating synchrotron emission as they become advected from X-points into plasmoids (Lyubarskii 1996b, Uzdensky & Spitkovsky 2014, Cerutti & Philippov 2017, Philippov & Spitkovsky 2018), and curvature radiation (Kalapotharakos et al. 2018, 2019). The first scenario predicts a cutoff at energies  $\sim \hbar\omega_B(\text{few} \times \sigma_{LC})^2 \approx 0.5 \text{ GeV}(B_{LC}/10^5 \text{ G})(\sigma_{LC}/10^5)^2$ , whereas the second one invokes curvature radiation-limited acceleration with the curvature radius of the field comparable with  $R_{LC}$  (Kalapotharakos et al. 2019). The second scenario may not be physically viable. The simulations by Kalapotharakos et al. (2018) have a very small ratio of  $R_{LC}/d_e$  and do not show plasmoid instability. For realistic pulsar conditions,  $R_{LC}/d_e \sim 10^6$ , in 3D, the current sheet is expected to be truly plasmoid-turbulent, and the local curvature of the field experienced by accelerated particles can never reach macroscopic scales and become comparable to  $R_{LC}$ . It should be comparable with the sizes of typical plasmoid-like structures, which are similar to the Larmor radius of reconnection-heated particles, effectively returning to the synchrotron scenario.

The synchrotron scenario, however, naively predicts a very steep dependence of the radiation cutoff on  $B_{LC}$ , which is not observed. An important key here is likely the pair production in  $\gamma-\gamma$  collisions of photons in the current sheet. Although the optical depth for GeV photons is low,  $\tau_{\gamma\gamma} \leq 1$ , the large dissipated energy implies a nonnegligible number of produced pairs. The broadband nature of the radiation spectrum from current sheets shows that pair production can be self-sustained; e.g., soft X-ray photons, which are targets for further pair-producing collisions with high-energy GeV photons, are produced by pairs in the sheet. This should be the case in young active pulsars, like the Crab, where the radiation energy density near the current sheet is sufficiently high. For example, the multiplicity of the plasma produced in the current sheet of Crab is likely larger than that of the polar outflow (see the **Supplemental Text Section 4**, for an estimate of the pair multiplicity; also Lyubarskii 1996b). The larger amount of plasma produced by pair production in the current sheet softens the dependence of  $\sigma_{LC}$  on  $B_{LC}$ , and, thus, the dependence of the cutoff energy, bringing it closer to the observed one, as shown by local 2D reconnection simulations by Hakobyan et al. (2019). In cases when  $\gamma_{rad} < \sigma_{LC}$ , most of the energy is radiated in X-rays, which reduces the gamma-ray efficiency for higher spin-down losses compared to the expected  $L_\gamma \propto \dot{E}$  relation, which is consistent with the observations of most energetic pulsars. More work needs to be done to understand these issues in the context of global magnetospheric simulations. It is also essential to test the above conclusions using 3D simulations with progressively larger separation of scales,  $L/d_e$ , at least for the isolated current sheets, as well as to better understand the dependencies on pulsar parameters, such as the Lorentz factor of the plasma bulk motion,  $\gamma_{rad}/\sigma_{LC}$  ratio, and the efficiency of pair production. Overall, the process of radiative reconnection with pair production was just starting to be explored (Beloborodov 2017, Hakobyan et al. 2019, Mehlhaff et al. 2021), and rapid progress is expected in the coming years.

Similarly, more work needs to be done to formulate quantitative predictions of the current sheet emission for observations in bands other than gamma rays. For example, synchrotron radiation of the produced pairs likely explains lower-energy incoherent radiation in the Crab, i.e., the optical/UV/X-ray bands (Lyubarskii 1996b). Inverse Compton scattering of low-energy photons

---

**Supplemental Material >**

by highest-energy particles close to (Harding et al. 2021) or beyond the light cylinder (Mochol & Petri 2015) is the working scenario to explain the observed pulsed up-to-a-few-TeV emission in the Crab, Vela, and other pulsars (e.g., Ansoldi et al. 2016, H.E.S.S. Collab. et al. 2018). In this regime, the energies of upscattered photons are comparable with particle energies, which indicates the presence of particles with energies  $\gamma \gtrsim \text{few} \times 10^6$ . Thus, existing and future (with High Altitude Water Cherenkov Gamma Ray Observatory and Cherenkov Telescope Array) observations in the TeV band will directly probe the highest-energy end of the particle spectrum in pulsars. Finally, polarization information of the high-energy emission with current (*Imaging X-ray Polarimetry Explorer*) and future missions will provide a new insightful probe. It may serve as an ultimate proof of the current sheet scenario because polarization is highly sensitive to the magnetic field geometry within the emitting region. Initial explorations using PIC simulations (Cerutti et al. 2016a) found a large position angle (PA) swing of the linear polarization. It is the consequence of the passage of the line of sight through the current sheet where the magnetic field flips direction over the duration of the pulse, which is consistent with the measured polarization of the optical emission in the Crab Nebula (Słowińska et al. 2009). Another prediction from numerical simulations is the smaller degree of linear polarization on-pulse compared to off-pulse, because of the formation of caustics in the observed emission pattern.

## 5. COHERENT RADIO EMISSION

Even though the energy output of pulsars in the form of radio emission is a very small fraction (typically  $10^{-6}$  to  $\sim 10^{-5}$ ) of the total energy loss, radio observations are still, by far, the dominant way of discovering and studying pulsars and their magnetospheres. Nevertheless, the mechanism responsible for the radio emission is still not identified, despite many years, many attempts, and many proposed theories. The difficulty lies in the plethora of emission properties that need to be explained, some of which may originate from the underlying emission process itself, whereas others are imprints from propagation effects in the pulsar magnetosphere (or, perhaps, in the interstellar medium). Distinguishing between them in the first place may not be trivial. In turn, studying the observed properties allows one to draw conclusions about the physical conditions and timescales prevailing in the magnetosphere. This is especially true when considering that (most) radio emission is apparently created near the magnetic polar cap, so that it may serve as a useful probe.

Since the discovery of pulsars, significant progress in characterizing the radio emission has been made and, especially also in recent time, key observations have been made. Combined, these allow us to connect many, albeit not all, emission properties to the magnetospheric processes that we discussed in the previous sections. In the following, we take a top-view approach and describe the most essential phenomena that we believe need to be explained. This is followed by a description of the general emission properties before we discuss some of the mentioned key observations. In Section 6, we undertake a critical assessment and identify the outstanding problems to be solved.

### 5.1. Essential Phenomena to Be Explained

A successful pulsar model should be able to explain a number of key features of radio emission, which we attempt to summarize as follows:

- **Coherence, brightness temperatures, micropulses, and nanoshots:** These phenomena are related to the actual nonstationary emission process and are fundamental properties that need to be explained.
- **Radio luminosity and flux density spectra:** While the radio output is small in comparison to the overall spin-down loss, the range of observed luminosities and spectra are likely to distinguish different emission models.

- **Polarization properties and frequency dependencies:** These features may be impacted by both the emission process and propagation effects in the magnetosphere. It is essential to model them in a consistent fashion.
- **Pulse shapes, stability and variability, origin of the shut-down or reconfiguration of magnetospheric processes, and timescales:** It seems to be a mystery what causes the magnetosphere to change its configuration and/or processes drastically and rapidly. At the same time, some state changes last for only a few to many million rotations. What causes these timescales?
- **Differences and similarities among the observed emission properties of normal pulsars, millisecond pulsars, and magnetars:** The parameter space is huge, the magnetic field structure may be quite different, the sizes of the magnetospheres are very different, but some basic emission features are very similar, whereas others are markedly different. Understanding what causes similarities and differences promises to be a powerful tool to distinguish between models on the way to a consistent description.

Some of these relevant features may be related to the emission process itself, whereas others may be—at least in part—due to propagation effects. We explain some of the used terminology in the following.

## 5.2. Features of Radio Observations

In the following, we provide an overview of the observed radio emission properties before we highlight particular key observations or sources, whose studies have been arguably more informative than perhaps the study of many other pulsars combined. Hence, the following aims not to be a complete listing of all possible observed emission features, which differ also from pulsar to pulsar, but to be intentionally schematic to highlight the common characteristics.

The pulsed emission from pulsars shows a rich variety of intriguing properties on an astonishingly large range of timescales, from nanoseconds to years, hence covering about 16 orders of magnitude mentioned in Section 1. Not all these timescales may have a magnetospheric origin, but understanding them promises insight into magnetospheric physics and possible connections to neutron star properties, geometry, or other factors.

Radio emission has been observed at frequencies as low as tens of MHz and as high as 150 GHz (Torne 2016), or even above 350 GHz for magnetars (Torne et al. 2022). It is a broadband phenomenon in which individual pulses have been detected with almost identical properties over many decades of frequency (e.g., Robinson et al. 1968, Karastergiou et al. 2001). However, even for seemingly simple statements like this, “exceptions to the rules” are commonly observed (e.g., Bhat et al. 2007), and we ignore those deliberately in the following in an attempt to describe the big picture.

**5.2.1. Flux density spectra.** Pulsar emission is coherent, with brightness temperatures reaching  $T_b = 10^{37}$  K (Hankins et al. 2003, Cordes et al. 2004) in so-called nanopulses lasting a few nanoseconds (see Section 5.3.1). The radio energy output peaks at a few hundred MHz (Malofeev et al. 1994, Maron et al. 2000) with flux densities at a few Janskys.<sup>20</sup> Converting this into a total energy output at radio frequencies is nontrivial. One has to take into account that the radio emission is beamed and that we (usually, but see Section 5.3.2) receive emission only from a single cut through the emission beam. Assuming typical beam widths and integrating over mean spectra, one

---

<sup>20</sup>1 Jansky corresponds to  $10^{-26}$  W m<sup>-2</sup> Hz<sup>-1</sup>.

---

**Rotating vector model (RVM):**

geometrical interpretation of the S-like variation of position angle of linearly polarized emission as a function of pulse phase

---

obtains a typical radio luminosity of  $\sim 10^{20}$  W (Lorimer & Kramer 2005), which we can compare to the spin-down luminosity representing the total energy loss per time of  $10^{26}$  W (with values up to  $10^{31}$  W being observed).

The flattest flux density spectra,  $S \propto v^\alpha$ , are typically observed for magnetars, i.e.,  $\alpha \approx 0$ , sometimes even with inverted spectra,  $\alpha > 0$  (e.g., Torne et al. 2017). The mean spectral index of normal radio pulsars is found to be  $\alpha \sim -1.6$  (e.g., Jankowski et al. 2018), although the value depends on the frequency range measured. Below the peak frequency at a few hundred MHz, the spectra are often found to turn over (e.g., Backer & Fisher 1974), whereas at high frequencies beyond a few GHz, a steepening can be observed frequently (Maron et al. 2000, Jankowski et al. 2018). A high-frequency cutoff claimed in the past (e.g., Malov & Malofeev 1991) or even recently (Jankowski et al. 2018) is simply an observational effect due to limited sensitivity at high frequencies (e.g., Kramer et al. 1997a, Torne 2016). In fact, there are indications that the spectrum may even show an upturn at millimeter wavelengths (Kramer et al. 1997b), and further observations are needed to explore this relatively unknown part of the radio frequency range. Overall, the observed radio spectrum may be dominated by the underlying emission process and/or a mechanism that leads to the coherence of the radiation. However, absorption processes may occur in the magnetosphere (e.g., Blandford & Scharlemann 1976, Lyubarskii & Petrova 1998) and may not only affect the spectrum but also observed pulse shapes (e.g., Fussell et al. 2003; see also Sections 5.2.7 and 5.4.2).

**5.2.2. Pulse properties.** Pulsar emission is elliptically polarized, and the degree of polarization can often reach 100% (e.g., Radhakrishnan & Cooke 1969). It is dominated by a linearly polarized component, but the degree of circular polarization can also reach tens of percent (e.g., Lyne & Manchester 1988) or may even become dominant at high frequencies (von Hoensbroech et al. 1998a; see **Figure 13**). This may suggest a conversion process due to propagation in the magnetosphere. Indeed, birefringence has been suggested as a mechanism (McKinnon 1997) to explain both the decrease in the degree of polarization (i.e., especially that of the linear component; Thorsett 1991, Xilouris et al. 1994) and the narrowing width of pulsar profiles with frequencies (e.g., Cordes 1978, Thorsett 1991, Johnston et al. 2008). Both effects are illustrated in **Figure 13** and further discussed in Sections 5.2.7 and 5.4.2.

Overall, the polarization properties are clearly dependent on age. Young and energetic pulsars (defined here as those with  $\dot{E} > 10^{35}$  erg s $^{-1}$ ) show typically a much larger degree of linearly polarized emission (von Hoensbroech et al. 1998a; Weltevrede & Johnston 2008). Indeed for such pulsars, the fractional polarization is well above 40% in the vast majority of the pulsars, as compared to a much smaller fraction for less energetic pulsars (Serylak et al. 2021). Given that the energetic pulsars are also those that dominate the population of gamma-ray-detected pulsars, it is worth noting that the joint radio and gamma-ray pulsar population shows the same polarization properties as the radio-only population (Serylak et al. 2021). Interestingly, for those young and energetic pulsars, the profiles are often simple and consist of either one or two prominent components. In profiles with two components, the trailing component nearly always dominates, only the trailing component shows circular polarization and the PA swing is generally flat across the leading component and steep across the trailing component (Johnston & Weisberg 2006).

The polarization orientation (i.e., the position angle) of the linearly polarized component often shows a characteristic S-like swing (Radhakrishnan & Cooke 1969), which can be explained by a geometrical effect known as the rotating vector model (RVM; see also Section 5.3.2). This interpretation is supported by the observation that the shape of the PA swing is often independent of observing frequency (see, e.g., **Figure 13a**). Modifications of the RVM comprise efforts to include special-relativistic effects (Blaskiewicz et al. 1991) and effects due to plasma propagation

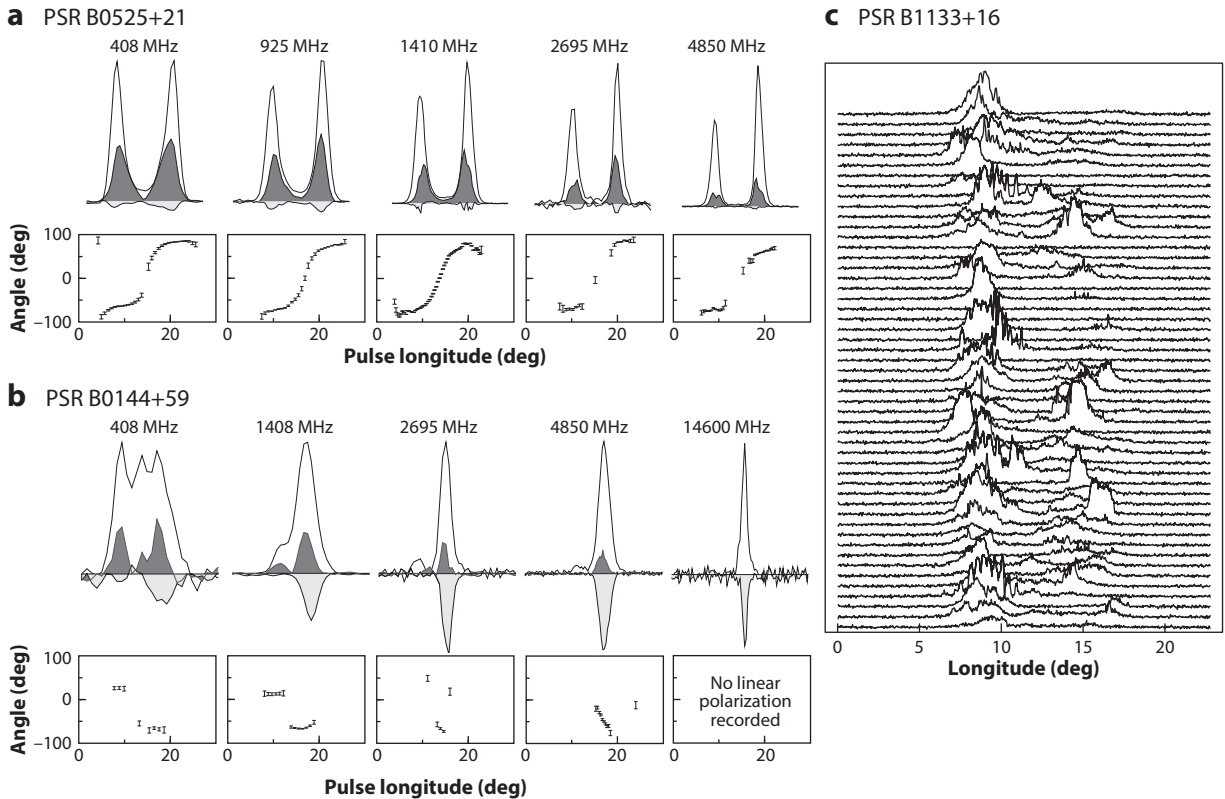


**Figure 13**

Examples for the evolution of radio polarization properties as a function of frequency (as observed by von Hoensbroeck et al. 1998a) and single-pulse emission observed with the Effelsberg 100-m telescope (M. Kramer, private communication). The dark shaded areas in the upper half of panels *a* and *b* indicate the component of linearly polarized emission. The light shaded areas show that of circular polarization. The lower half of panels *a* and *b* show the position angle of the linearly polarized component. (*a*) PSR B0525+21 as a textbook pulsar with a number of typical features: Both the pulse width and the degree of polarization decrease with increasing frequency. At the same time, the position angle remains unchanged, even though fewer points are defined at higher frequencies as the total and linearly polarized intensity diminishes, in particular, in the center of the pulse. (*b*) In contrast, PSR B0144+59 also shows a decrease in width and linear polarization, but it is somewhat atypical as the central component remains as the dominant component at high frequencies. Also unusual, but not uncommon, is the increasing fraction of circular polarization. (*c*) Sequence of single pulses of PSR B1133+16 demonstrating simultaneously the common pulse-to-pulse variation (including different short-term variation in the leading and trailing pulse components), periodic micropulses (sometimes superimposed on featureless subpulses), and the phenomenon of nulling, when the pulsar stops emitting all together.

or current flow (e.g., Hibschman & Arons 2001, Beskin & Philippov 2012). Although we discuss those further below, they may cause deviations from a simple S-like swing. Indeed, one also commonly observes complicated, distorted PA swings that do not resemble an RVM-like shape (e.g., Johnston et al. 2008; or see Figure 13*b*), especially for recycled pulsars (e.g., Xilouris et al. 1996). When the polarization of individual pulses is inspected, abrupt orthogonal transitions in the PA (e.g., Manchester et al. 1975) are seen. If they can be accounted for, the expected RVM behavior can be reconstructed (Gil & Lyne 1995). The existence of such orthogonal polarization modes (OPMs) and the frequency dependency of their occurrence point to propagation effects in the pulsar magnetosphere as their origin (see Section 5.4.2). Such effects may also be responsible for some of the general behavior of the circularly polarized emission that tends to be at maximum

**Orthogonal polarization modes (OPMs):** observed jumps of the position angle by 90 deg interpreted as different electromagnetic modes in the plasma

**Pulse profile:** pulse shape obtained after averaging hundreds to thousands of pulses

**Moding:** changes between a small number of stable pulse shapes for typically hundreds of periods

**Nulling:** omission of detectable radio emission for a certain period of time, typically lasting tens to hundreds of periods

**Intermittent pulsars:** pulsars with intermittent periods of ceased radio emission lasting for weeks, months, or even years

**Subpulses:** basic components of radio emission comprising the individual radio pulses

**Microstructure:** short-duration quasi-periodic pulses often superimposed on a broader subpulse envelope

or shows a sign reversal (i.e., a change in handedness) near the pulse center, where the steepest gradient of an S-like PA swing can be found.

**5.2.3. Time-variable properties.** Individual pulses of a given pulsar show a large variety in shape and intensity (**Figure 13**). They manifest themselves in a number of features and timescales observable in single pulses. We can expect that these features, which we introduce further below, are a direct consequence of the dynamic processes in the magnetosphere that were discussed in Section 4.5. Despite this variety, computing the average pulse shape by summing up (or averaging) a few hundred to thousands of pulses (regardless of intensity and shape) leads to an (average) “pulse profile” that is characteristic for a given pulsar at a given frequency. It may be surprising that in the presence of the single-pulse variety, a small number (typically between one and five: Rankin 1983, Lyne & Manchester 1988; exceptionally more: see, e.g., Kramer 1994) of distinct profile components can be identified, pointing to a preferred position of emission activity along the observer’s line of sight through the pulsar beam or, alternatively, to a certain spatial scale of plasma activity within the open field line region. Some similarities among—and differences between—central and outer profile components (e.g., central components are called cores and tend to have steeper spectra and a larger degree of circular polarization in contrast to outer “conal” components) result in often systematic changes in pulse shape when changing observing frequency. This has led to a number of phenomenological models suggesting, for instance, concentric cones of emission (Rankin 1990), whereas a random location of emission features within the beam are also suggested (Lyne & Manchester 1988). Recent data in Section 5.3.2 provides insight here.

Individual pulses can be considered a reflection of “magnetospheric weather” (see Sections 4.5), whereas the pulsar profile is dominated by long-term “climate” (i.e., those basic features discussed in Section 3) and in particular geometrical effects, i.e., how the pulsar is orientated to the observer and where the emission beam is cut. Since the early days of pulsar research, it was noticed that several stable states of such climate may exist though, as pulsars were found to abruptly switch their pulse profile between a small number (typically two to three) of shapes that remain in place for hundreds (or more) of pulsar rotations (so-called moding; Backer 1970c), and that some pulsars completely switch off their emission for a similarly long period of time (so-called nulling; Backer 1970a) (see **Figure 13**). The phenomenon is clearly very broadband with emission stopping simultaneously across a wide frequency range (e.g., Gajjar et al. 2014). This may suggest that nulling may indicate the absence of pair cascade for a certain period of time. Moding and nulling are apparently related (e.g., Wang et al. 2007) and seem to be linked to more global processes in the magnetosphere, which occur also on timescales of weeks or even years in the case of “intermittent pulsars” as discussed further in Section 5.3.3.

Inspecting the individual pulses with increasing time resolution shows them to be usually comprised of clearly identifiable subpulses (Backer 1970b; see **Figure 13**). Often the location of the subpulses changes in a systematic and periodic pattern from pulse to pulse, “drifting” across the pulse window as defined by the extent of the pulse profile (e.g., Drake & Craft 1968, Edwards & Stappers 2002, Hassall et al. 2013). This allows one to define additional timescales, e.g., until a similar subpulse pattern is reached.

With sufficient time resolution, one can also detect in many (but not all) subpulses further structure of spiky, narrow “micropulses”, collectively known as microstructure. These narrow pulses often occur with a quasi-periodicity that is roughly twice their width (e.g., Cordes et al. 1990; see **Figure 13**). The width and also the quasi-periodicity of micropulses scale linearly with the pulse period (Cordes 1979, Kramer et al. 2002). The phenomenon of microstructure may be related to the processes discussed in Section 4.4.1.

**5.2.4. Magnetospheric origin of radio emission from observations.** As argued in Section 4.5 the polar cap region of the magnetosphere emerged as a second region, next to regions near the light cylinder, where coherent radio emission is likely to be produced. One can use a number of observational facts of “normal pulsar emission” to support this notion.

First, the pulse window given by the average radio pulse profile is usually much narrower than the duration of the observed high-energy pulses. Radio pulses of nonrecycled (“normal”) pulsars (see Section 5.2.5 for a comparison with recycled pulsars) have a mean duty cycle of only a few percent. This fact alone suggests that radio emission is confined to a narrow, well-defined region in the magnetosphere, with a location that is different from the origin of magnetospheric high-energy emission. Direct observational evidence for emission originating close to the polar cap is provided, interestingly, by the emission of the young pulsar J0737–3039B in the double pulsar system (Lyne et al. 2004). The pulsar wind of the recycled, more energetic companion, PSR J0737–3039A, blows away half of the magnetosphere of pulsar B, requiring the observed radio emission of pulsar B to originate from low altitudes (see, e.g., Kramer & Stairs 2008 for a review of the system properties).

A number of methods have been used to determine actual altitudes, from which the emission may emerge to reach the observer. The derived estimates are often called emission heights, suggesting that the observed radiation was created there. But, more generally, these may be altitudes at which the observed emission decouples and escapes from the magnetospheric plasma, after having propagated from a lower altitude in particular plasma modes (see Section 5.4).

One method to determine such altitudes is the use of the observed pulse width (especially when corrected for geometrical viewing effects) and matching it to the opening angle of an emission beam filling the open field line region, as done in **Figure 14**. Results indicate altitudes of hundreds to thousands of kilometers above the magnetic pole and the polar cap region (see also, e.g., Lorimer & Kramer 2005). It is useful to express these emission heights in terms of the light cylinder radius,  $R_{LC}$ . For normal pulsars the value is typically  $0.1R_{LC}$ , whereas for fast spinning pulsars, including millisecond pulsars, the derived altitudes are a significant fraction of  $R_{LC}$  (see **Figure 14** and Section 5.2.5). Interpreting the often observed delays of the center of the PA swing relative to that of the total intensity pulse as the result of special relativistic effects (Blaskiewicz et al. 1991, Hibschman & Arons 2001, Dyks 2008; see also Section 5.3.2) leads to similar estimates.

The fact that the pulse width usually decreases with increasing frequency (see Section 5.2.2, and also, e.g., Phillips & Wolszczan 1991) has led to the proposal of a frequency-dependent emission height known as radius-to-frequency mapping (Cordes 1978). However, evidence for such models is rather weak. Attempts to measure retardation of the emission between frequencies (e.g., Phillips & Wolszczan 1991, Kramer et al. 1997b) were not successful. The most stringent constraints come from Hassall et al. (2012). Using simultaneous observations between 40 MHz and 8.3 GHz, they conclude for slowly rotating pulsars that the emission originates from within a few hundred kilometers or less in the magnetosphere, which is consistent with previous estimates. The need for radius-to-frequency mapping disappears if one ascribes the change in pulse width with frequency to propagation effects in the magnetosphere such as refraction (McKinnon 1997). We discuss further observational evidence for propagation effects in Section 5.4.2 and discuss the current theoretical understanding in Section 5.4.

**5.2.5. Recycled versus nonrecycled pulsars.** When comparing normal pulsars (i.e., nonrecycled pulsars) with so-called millisecond pulsars (i.e., recycled pulsars), we increase the period space to be covered by our considerations by four orders of magnitude and the estimated surface magnetic field space by seven orders of magnitude. And yet, the radio emission observed among these groups seems to be similar in many respects. Differences exist also, though, they are ultimately

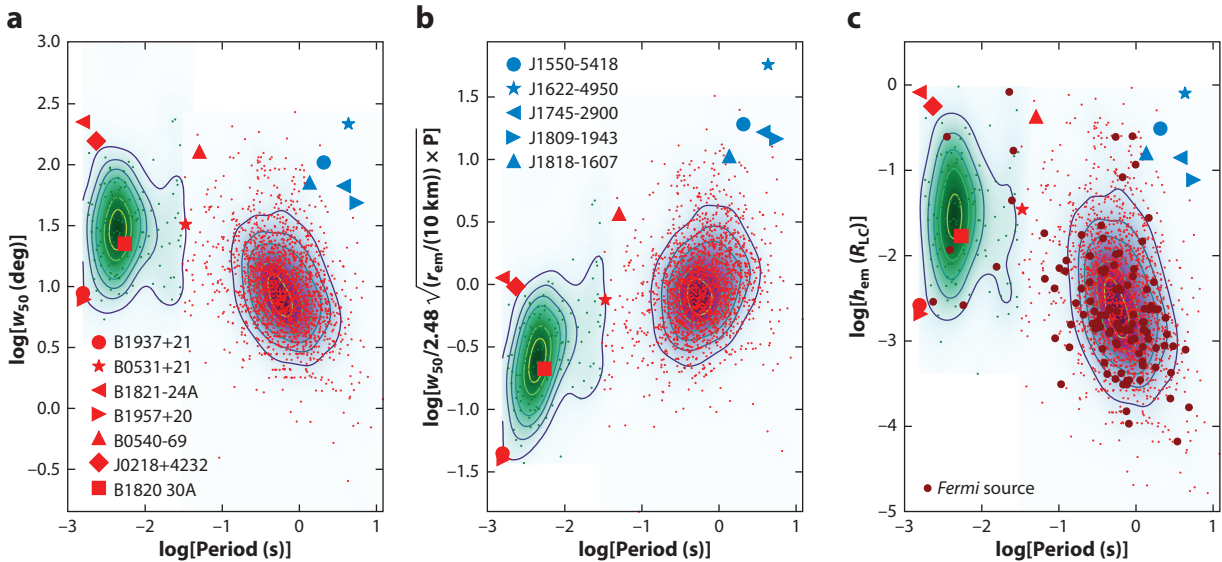


**Figure 14**

Radio pulse widths as a function of pulse period normalized in different ways. Nonrecycled pulsars are marked in red, and recycled pulsars are in green. The pulse widths shown here are measured at a 50% intensity level as recorded in the ATNF pulsar catalog. We note that this quantity may underestimate the real pulse width in cases with a strong central component (see, e.g., Posselt et al. 2021), but it is available for all pulsars. (a) Pulse widths measured in degree of rotational longitude. It is visible that millisecond pulsars tend to have wider pulse profiles. (b) Pulse widths normalized by twice the value of the opening angle of the last open field lines in a dipolar magnetic field for an emission height of 100 km. Although geometrical effects are ignored (e.g., the observed width does not correspond to the diameter of the beam unless one encounters a central cut across the pole), it can nevertheless be noted that the observed pulse widths for normal pulsars are consistent with emission heights of 100 km within factors of a few. We also note the recycled pulsars seem to underfill their open field line region for such a height. (c) Assuming that all pulsars fill their open field line region, one can convert the observed width into an emission height expressed in a fraction of the light cylinder radius. This plot shows that recycled pulsars tend to emit at larger fractional heights in their compact magnetosphere compared to normal pulsars. We mark the radio-loud gamma-ray-detected sources in dark red, which are broadly consistent with the bulk population of radio pulsars. We also mark the classical giant-pulse emitters (*red symbols*) and radio-loud magnetars (*blue symbols*) in all plots. The legend in panel *a* lists the giant-pulse emitters in order of decreasing magnetic field strength at the light cylinder.

caused by the much more compact magnetospheres (for instance, leading to a nondipolar field due to twists near the much closer light cylinder; see Section 5.4.2) but potentially also as a result of the different evolutionary history. As matter has been accreted during the recycling process, not only the magnetic field strength but perhaps also the magnetospheric structure may have been altered.

The average spectral index measured for millisecond pulsars between, say, 600 MHz and 3,000 GHz appears to be very similar to that of normal pulsars, with both showing an index of  $\alpha \approx -1.8$  (e.g., Kramer et al. 1999, Dai et al. 2015, Spiewak & et al. 2022). Interestingly, the spectra of millisecond pulsars tend to show fewer low-frequency turnovers or high-frequency breaks (Kondratiev et al. 2016; Kramer et al. 1998, 1999) than in the case of normal pulsars (Maron et al. 2000, Bilous et al. 2016). Interestingly, though the luminosity of recycled and nonrecycled pulsars appears to be very similar, once accounting for selection effects (Kramer et al. 1998), it has been noted that isolated millisecond pulsars tend to be less luminous (Bailes et al. 1997, Kramer et al. 1998); this is a trend that seems to hold as the observed sample grows larger (Burgay et al. 2013).

Comparing the pulse profiles of recycled pulsars across the sample and observing frequencies, three things are very noticeable. First, millisecond pulsar profiles evolve much less in frequency, with the shape, width, and component separation usually hardly changing from the lowest to the highest frequencies (Kramer et al. 1999, Kondratiev et al. 2016) (although prominent counterexamples do exist, e.g., PSR J1022+1001; Ramachandran & Kramer 2003). This is not unexpected as the magnetosphere of fast spinning pulsars is much more compact, suggesting that height-dependent or propagation effects have less impact. Second, the pulse profiles typically are wider in units of pulse phase, but when trying to account for geometrical and line-of-sight effects, the estimated active open field line region appears to be smaller than that of nonrecycled pulsars (Kramer et al. 1998; see **Figure 14**). Overall, the pulse shapes appear to essentially fall into two categories, those that look similar to profiles of nonrecycled pulsars with a similar number of identifiable pulse component numbers (Kramer et al. 1998, Lorimer & Kramer 2005) and those that are very complex, are very wide, and show multitudes of separate components (see, e.g., Spiewak & et al. 2022 for an impressive display). Third, a feature that has been pointed out early (Kramer et al. 1998, 1999) and that persists throughout an increased sample (Dai et al. 2015, Spiewak & et al. 2022) is the observation of additional low-intensity pulse components and so-called pre- and postursors to the main pulse (MP). These may be the result of additional radio emission sites in the magnetosphere or, perhaps, imprints of a substantially nondipolar field configuration. Interestingly, NICER observations of thermal X-ray surface hotspots provide evidence for a quadrupolar magnetic field geometry in the millisecond pulsar J0030+0451 (Miller et al. 2019, Riley et al. 2019).

Unlike in nonrecycled pulsars, the PA swing of the linearly polarized component hardly ever resembles an S-like swing in recycled pulsars. Generally, they often appear flat over a rather wide pulse phase range (Xilouris et al. 1996, Kramer et al. 2021, Spiewak & et al. 2022), with the slope tending to increase with pulse period (Kramer et al. 2021). With sufficient time resolution, a complex underlying structure can frequently be recognized (e.g., Dai et al. 2015). At this moment in time, it is unclear whether these complex PA swings result from overlapping beamlets with OPMs, other propagation effects, twisted field lines in the otherwise compact magnetosphere, or a combination of the above. Any emission height may be dominated by magnetic multipoles near the surface and/or twists of the fields near the small light cylinder. We return to some of these questions in Section 5.4.2.

**5.2.6. Magnetic-field versus rotation-powered pulsars.** It is believed that the energy output by magnetars is fed by the magnetic field energy of these neutron stars, rather than by the loss in rotational energy. A handful of magnetars have been observed at radio frequencies, though their phase as radio emitters appears to be of transient nature, apparently triggered by high-energy outbursts (Kaspi & Beloborodov 2017). The observed radio emission properties show similarities to but also distinct differences from those of rotation-powered pulsars. Most strikingly, magnetar emission shows an extremely large degree of linear polarization, mostly up to 100% (e.g., Camilo et al. 2007b, Kramer et al. 2007, Levin et al. 2010, Eatough et al. 2013, Dai et al. 2019, Champion et al. 2020), and even up to frequencies as high 100 GHz or more (Torne et al. 2017, Liu et al. 2021).

The highest frequencies at which magnetar pulsed radio emission, and, indeed, any radio emitting neutron stars, has been detected are 250 GHz (Torne et al. 2020) and even 350 GHz (Torne et al. 2022). These high-frequency detections of magnetars are possible owing to unusually flat flux density spectra, which is another common feature that is different than in normal pulsars (Camilo et al. 2006, Serylak et al. 2009, Torne et al. 2015, Dai et al. 2019), with variations in the single-pulse spectra (Lazaridis et al. 2008, Serylak et al. 2009, Torne et al. 2015) that are larger than those of normal pulsars (e.g., Kramer et al. 2003).

Unlike normal pulsars, the single pulses are often composed of very narrow spiky emission features, distributed over an often wide pulse window (Camilo et al. 2007a, Kramer et al. 2007, Torne et al. 2015). Longitude-resolved modulation indices reveal a high degree of intensity fluctuations on short and long timescales (Serylak et al. 2009), leading to varying shapes of average pulse profiles (Camilo et al. 2007a, Levin et al. 2019, Champion et al. 2020). The recent discovery of giant pulses in XTE J1810–197 (Caleb et al. 2021) provides an interesting link between magnetar emission and that of rotation-powered giant pulse emitters (see Section 5.3.1).<sup>21</sup>

The PA swing observed in magnetar radio emission also changes with time, sometimes between frequencies, but not always for all pulse components at the same time (Kramer et al. 2007). The wide profile, the changing of pulse shape and PA swing and the variability of the emission overall, may indicate that the emission originates at a different place or under different magnetic field configurations than in normal pulsars. On the longer timescales, profile changes are often associated with changes in the spin-down behavior (Camilo et al. 2007a, Champion et al. 2020). Overall, the magnetars show a high degree of timing noise with timing irregularities and glitches (Kaspi & Beloborodov 2017).

The radio emission of magnetars, after being triggered by an outburst, tends to become weaker with time before it eventually disappears (Kaspi & Beloborodov 2017). The magnetar in the Galactic center is currently the one with the longest record of radio detections (Liu et al. 2021). Reappearances of magnetar emission after a long period of inactivity have also been observed (Dai et al. 2019, Levin et al. 2019), whereas the radio emission of normal pulsars is intrinsically mostly very steady (e.g., Kumamoto et al. 2021).

**5.2.7. Evidence for plasma propagation effects.** The existence of orthogonally polarized emission modes indicates the presence of propagation effects in the magnetosphere. Indeed, many of the observed polarization properties may be affected by or even be the result of propagation effects. For instance, one may encounter weak Faraday rotation across the pulse phase (see Noutsos et al. 2009, Ilie et al. 2019). But, more importantly, the frequency evolution of the pulse width may be the result of refraction in the magnetosphere as mentioned in Section 5.2.4. Obvious propagation effects are at play when the shape of a PA swing that may be intrinsically determined by a geometry-related origin (see Section 5.3.2) is distorted across pulse phase and/or radio frequency (Gil & Lyne 1995, Petrova & Lyubarskii 2000, Beskin & Philippov 2012). **Figure 15** shows an example in which the handedness of the circularly polarized emission (i.e., the sign of Stokes  $V$ ) changes only in one of three components of a pulse simultaneously observed at different frequencies. This is similar in the pulse profile of the orthogonal rotator PSR J0908–4913, where the nearly perpendicular orientation of the spin and magnetic axes allows the observation of both magnetic poles. In this particular case, the sign of  $V$  changes between 1.4 and 3 GHz, simultaneously, in both the MP and interpulse (Kramer & Johnston 2008).

In this context, it is interesting to note a strong correlation pointed out by Johnston & Kramer (2019); i.e., if the slope of the PA swing for the MP and interpulse is the same, then the sign of  $V$  is the same. Conversely, if the slope of the PA swing changes sign from MP to interpulse, then so does the sign of  $V$ . This implies that the sign of  $V$  depends on the hemisphere of the emission. There is overall evidence that the sense of circular polarized emission is correlated with a particular slope of the PA swing (Han et al. 1998, Beskin & Philippov 2012, Johnston & Kramer 2019; see also Section 5.3.2).

---

<sup>21</sup>We note that the detection of short radio bursts from SGR 1935+2154 (Bochenek et al. 2020, CHIME/FRB Collab. et al. 2020) may provide a link between the magnetospheric emission of magnetars and FRBs. Given that the emission was not seen to be persistent, we do not consider it here in detail or include the source in **Figure 14**.

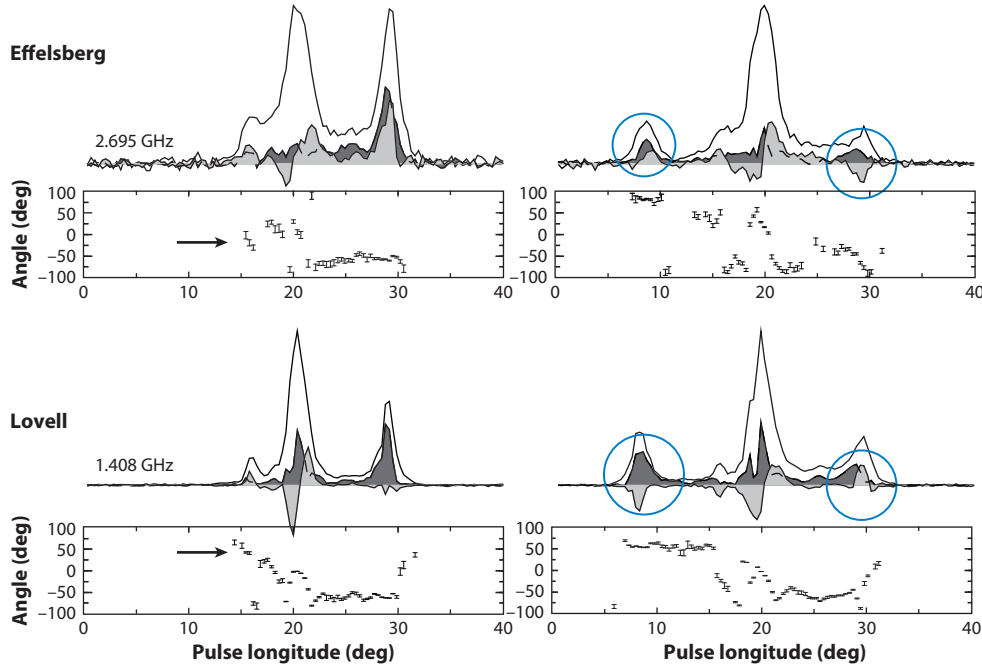


**Figure 15**

Evidence of propagation effects in the pulsar magnetosphere visible here in two single pulses of PSR B0329+54 simultaneously observed at two different frequencies. Although the PA is consistent between the frequencies (but different from pulse to pulse), the handedness of the circularly polarized emission (*light-shaded area*) shows a change at the central component consistently at both frequencies, but opposite sign for the outer components. The abrupt changes in the PA curves are due to orthogonal polarization modes, as discussed in Section 5.2.2. Figure adapted from Karastergiou et al. (2001). Abbreviation: PA, position angle.

### 5.3. “Rosetta Stones” of Observational Results

The number of different phenomena described above is rich and difficult—or even seemingly impossible—to account for by a single explanation. It helps to focus on a few individual pulsars, which appear to provide unusually deep insight into magnetospheric physics.

**5.3.1. The Crab pulsar.** The Crab pulsar differs in many ways from most other radio pulsars, but we discuss it here especially because it is notable from a number of points. With its discovery in 1968 and measurement of the pulsar’s spin period of  $P = 33$  ms (Staelin & Reifenstein 1968, Lovelace & Sutton 1969), the interpretation of pulsars as rotating neutron stars was firmly established. Its spin period remained the shortest known until the discovery of millisecond pulsars in 1982 (Backer et al. 1982). The Crab pulsar was also the first to be detected outside the radio regime (Cocke et al. 1969), and it is indeed a bright source in every part of the electromagnetic spectrum (e.g., Moffett & Hankins 1996, Hankins et al. 2015; see Figure 1). It is the brightest optically visible pulsar (Shearer & Golden 2002), embedded in a prominent nebula, providing the archetype for so-called PWNe. The PWN sits inside the famous Crab Nebula that is the remnant of a supernova explosion witnessed in 1054, making the Crab pulsar also one of the youngest pulsars known. This presumed connection of pulsars as being born in supernovae (Baade & Zwicky 1934) was firmly established with the Crab pulsar discovery. Remarkably, since its discovery in

1968, we have monitored this pulsar for  $\sim 6\%$  of its lifetime, which is much more than for any other pulsar.

---

**Giant pulses:** single, bright pulses with a mean flux density that exceeds that of the normal pulses by an order of magnitude or more

**Nanoshots:** extremely short and bright pulses of radio emission observed in the Crab pulsar

---

The radio emission is peculiar for many reasons. First, its flux density spectrum is among the steepest of any known radio pulsar, with a spectral index of  $\alpha = -3.1$ , compared to a mean spectral index of  $-1.6$  for the whole population (see Section 5.2.1). Second, it shows exceptionally bright, broadband pulses, so-called giant pulses. Furthermore, the most prominent profile components are aligned in rotational phase across all spectral windows. But additional pulse components are seen at other rotational phases and not all of them persist at all radio frequencies (see Figure 1).

At low frequencies, apart from very prominent MP and interpulse (low-frequency interpulse, LFIP), a precursor is observed that precedes the MP. The precursor vanishes around 1 GHz when it is replaced by a different, new component that is then stronger than the precursor but still much weaker than the MP. At higher frequencies, two additional components appear (“high-frequency components,” HFC1 and HCF2; Moffett & Hankins 1996). The LFIP disappears around 4 GHz and is replaced by a “high-frequency interpulse” (HFIP) that arrives a little earlier than the LFIP. The MP disappears above 8 GHz, and above 20 GHz the HFC1/2 are stronger than the HFIP (Hankins et al. 2015). Comparing these components with the high-energy light curves, the prominent components traceable from optical to gamma-ray frequencies align in rotational phase with the MP and the LFIP (and also the HFIP, despite the slightly earlier phase).

The spectral and temporal properties of these various components are strikingly different. We refer to Eilek & Hankins (2016) for a detailed description of the differences that we summarize here. First, the MP and the LFIP exhibit the giant pulses, for which average flux density exceeds that of the normal pulses by more than a factor of 10. Giant pulses are detected in about a dozen pulsars or less but in the Crab pulsar they can be resolved into strikingly narrow and bright “nanoshots.” These bursts of emission last on the order of a nanosecond (Hankins et al. 2003) and may be even still unresolved (Jessner et al. 2010, Eilek & Hankins 2016). These nanoshots are extremely bright (thousands of Janskys) with correspondingly high brightness temperatures ( $T_B \sim 10^{37}$  K) while at the same time they are relatively narrowband ( $\delta\nu/\nu \sim 0.1$ ) centered on varying frequencies. They are elliptically polarized with a dominant circularly polarized component, the sign of which changes at random from shot to shot (see also Jessner et al. 2010). Superimposed in “clumps,” they seem to make up the more commonly observed micropulses in the MP and LFIP, which are observed to be relatively broadband (Eilek & Hankins 2016).

Second, the HFIP has strikingly different properties. It does not exhibit nanopulses but the observed micropulses making up the HFIP typically last longer (by a factor of  $\sim 10$ ) and overlap each other, rather than being separable in clear components. Most peculiar, however, are the spectral properties of these overlapping micropulses. Their emission is concentrated in narrow spectral emission bands. These “zebra stripes” show no resemblance to the spectral properties of the MP or LFIP and vary from micropulse to micropulse. The spacing between the bands scales as  $\Delta\nu \sim 0.06\nu$  (Hankins et al. 2016), and one can observe a small slope of frequency with pulse duration. Interestingly, the HFIP components show a variation of dispersion measure relative to the MP, suggesting dispersion within the magnetosphere (Eilek & Hankins 2016). At the same time, HFIP pulses are linearly polarized with a nearly constant PA across the pulse.

The low-frequency precursors possibly originate from low altitudes near the polar cap, as ordinary pulsar radio emission does. For the other prominent radio emission components (MP, LFIP, and HFIP), the described properties suggest that they originate from similar magnetospheric locations as the high-energy emission, even though a slight phase offset and the much narrower appearance may indicate that the locations are not completely identical (e.g., Moffett & Hankins 1999, Eilek & Hankins 2016). The slight enhancement ( $\sim 4\%$ ) in the optical and X-ray fluxes observed during giant pulse emission (Shearer et al. 2003, Enoto et al. 2021) provides a

direct connection (see also Section 5.4.4). A recent scintillation study of the Crab’s giant pulses suggests that the giant pulse emission regions are extended, and that MP, LFIP, and HFIP arise in physically distinct regions that are resolved by the scattering screen and located near the light cylinder radius (Main et al. 2021). These results are consistent with the discussion provided in Section 4.5.2.

We finally note that during the past 22 years, the separation of the MP and LFIP showed a steady increase at a rate of  $0.62 \pm 0.03$  deg per century (Lyne et al. 2013). Although there are also secular changes in the relative strength of the components, their changing separation suggests  $\dot{\chi} > 0$ ; i.e., the Crab pulsar is becoming a more orthogonal rotator.<sup>22</sup> This is in contrast with an apparent statistical trend for other pulsars, as we highlight further in Section 6.

**5.3.2. Pulsar J1906+0746.** This binary pulsar makes this list of noteworthy sources, as it allowed unprecedented studies of the radio emission beam and its composition via relativistic spin precession. The observed pulsar, J1906+0746, is the young, nonrecycled component in a compact relativistic double neutron star system (Lorimer et al. 2006, van Leeuwen et al. 2015). The spin vector of the pulsar is inclined to the total angular momentum vector by  $104 \pm 9$  deg, which causes it to precess about the total angular momentum vector with a measured rate of  $2.17 \pm 0.11$  deg per year, which agrees perfectly with the prediction of GR (Desvignes et al. 2019). The observations do not only provide a test of GR; they also allow us to study two fundamental aspects of pulsar radio emission: the properties of the emission beam and the validity of the RVM (see Section 5.2).

The precession changes the viewing geometry and moves the line of sight across the pulsar beam, providing a “tomography” of the emission beam. As the pulsar’s magnetic axis has a fortunate nearly orthogonal orientation relative to the spin axis, our line of sight actually intersects the beam above both magnetic poles (with  $\chi_{\text{MP}} = 99.4 \pm 0.2$  deg and  $\chi_{\text{IP}} = 180$  deg –  $\chi_{\text{MP}} = 80.6 \pm 0.2$  deg). The observations provide evidence that there is no symmetry between the two poles, as the inferred beam patterns are clearly different. They have in common that while they appear to fill the open field line region in the latitudinal direction, the beams are less extended in the longitudinal direction (Desvignes et al. 2019). Similar observations of the young pulsar PSR J1141–645 (Manchester et al. 2010, Venkatraman Krishnan et al. 2019) or the recycled Hulse–Taylor pulsar, PSR B1913+16 (Kramer 1998, Weisberg & Taylor 2002, Clifton & Weisberg 2008), suggested a beam shape that is not similar to a canonical hollow cone. The observations of PSR J1906+0746 go further.

Our line of sight crossed one of the magnetic poles, i.e., that responsible for the initial interpulse emission. First, we see that the emission beam is active on either side of the pole, ruling out models that predict radio emission to be restricted to one side of the pole.<sup>23</sup> Second, the emission pattern is not symmetric in the latitudinal direction relative to the pole. Third, above the pole itself the emission is reduced, matching theoretical predictions for the current density in the polar cap for an orthogonal rotator discussed in Section 3.2.2 (see also the fourth example in Figure 3). Fourth, studying the polarization characteristics, we see that the handedness of the circularly polarized emission changes when crossing the pole (see Section 5.4.2). Fifth, the fractional linear polarization overall decreases with increasing distance from the beam center. Sixth, the emission height inferred from polarization data appears to increase from very low emission height near the

<sup>22</sup>Because of the observed coincidence of high-energy and radio profiles, a set of historical radio data was used to infer the inclination angle from the radio peak separation assuming a model appropriate for the high-energy emission.

<sup>23</sup>This applies to old models of stationary pair cascades (Arons & Scharlemann 1979) and models relying on the presence of ions extracted from the surface (Cheng & Ruderman 1980, Jones 2014).

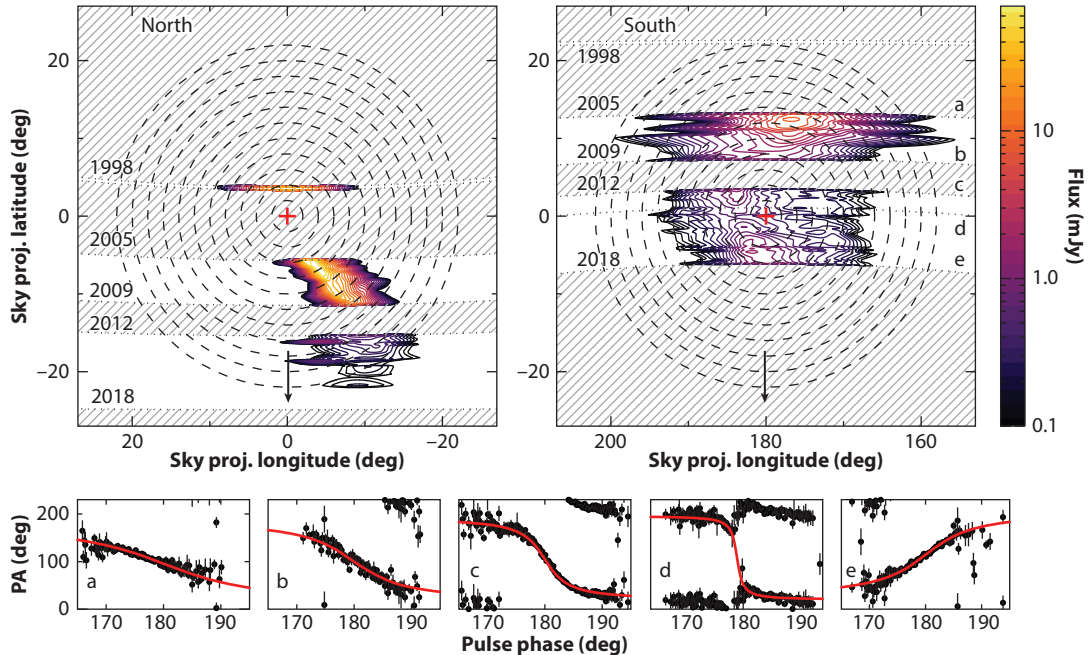


**Figure 16**

Beam pattern of the north and south magnetic poles of PSR J1906+0746 as projected on the sky and observed by Desvignes et al. (2019). The beams are sampled via the line of sight moving because of relativistic spin precession. During the observations, the line of sight moves in the direction indicated by the arrow and crosses the magnetic pole on the right. The resulting position angle (PA) swing shown on the right evolves with time (see panels *a–e*) as expected from the rotating vector model, swapping slope when crossing the pole. At the same time, the emission weakens and the circular polarization changes sign (see Desvignes et al. 2019). Furthermore, the degree of linear polarization of the main pulse decreases with increasing distance from the pole, whereas some unpolarized pulse components appear and disappear on timescales of months close to the beam edge.

pole to emission heights of about 320 km or, in the case of this 144-ms pulsar,  $0.046 \times R_{LC}$ , which has also been predicted (Yuen & Melrose 2014) and seen in other pulsars (Gupta & Gangadhara 2003, Johnston & Kramer 2019). Finally, and perhaps most importantly, the PA swing follows a canonical S-like swing that becomes steeper for lines of sight close to the pole, swaps its sign in slope when crossing the pole, and becomes flatter again moving away from the pole (Desvignes et al. 2019; see Figure 16), as predicted by the RVM. This pulsar therefore provides unequivocal evidence that the origin of the S-like swing is geometrical. And indeed, the inferred viewing geometry leads to a perfectly consistent description of the pulsar, the binary orientation, and predictions of GR (Desvignes et al. 2019). One can use the apparent lack of strong propagation effects in this pulsar in return to constrain the parameters of the magnetospheric plasma. Galishnikova et al. (2020) show that plasma parameters are qualitatively consistent with theories of plasma production in polar cap discharges. Specifically, for PSR J1906+0746, they constrain the pair multiplicity  $\lambda \sim 10^3$  and the Lorentz factor of a secondary plasma,  $\gamma_{sec}$ , to be a few hundred.

**5.3.3. Pulsar B1931+24, other intermittent pulsars, and rotating radio transients.** The phenomenon of nulling had been known since the early days of pulsar research (Backer 1970a; see Section 5.2), describing a period of time (typically a few tens to a hundred, but up to a thousand, pulsar rotations) when pulses cannot be registered before emission restarts again. In 2006, the phenomenon of “intermittency” was established with the prototypical case of PSR B1931+24.

Kramer et al. (2006) showed that this otherwise ordinary pulsar (i.e., with a period of 814 ms, a nonunusual pulse shape, and a position in the middle of the  $P$ - $\dot{P}$  diagram as shown in Section 6) is detectable for a period of about one week, before becoming undetectable for a period of about one month, to then become visible again, in a quasi-periodic fashion. The number of pulsar rotations without detected pulses is very much larger than that for nulling, here a few million rotations, and for further detected “intermittent pulsars” (e.g., PSR J1832+0029, Lorimer et al. 2012; or PSR J1841–0500, Camilo et al. 2012) even longer still (i.e., for a period of two to three years, or many tens of millions of rotations). The long duration of the “on” and “off” periods of many days, if not longer, allows for testing of a crucial question that already arises with nulling: Is the complete magnetospheric radio emission or only a fraction of the magnetosphere including the observer’s line of sight quenched, or is the radio emission still active and our telescopes miss the pulsar beam for other reasons, e.g., due to precession? Kramer et al. (2006) were able to rule out precession, as observations showed that the radio emission ceases within (at most) a few rotations (the limit given by the requirement to obtain a sufficient signal-to-noise ratio), which is too fast for a beam to move out of our line of sight (see also Mottez et al. 2013). Orbital motion of a body could also be excluded (Rea et al. 2008). Instead, Kramer et al. (2006) showed by comparing the pulsar spin down before and after a radio-quiet interval that the pulsar spins down 50% faster when the radio emission is on, rather than off. This increase in spin-down rate is a feature that is consistently present in all other intermittent pulsars, with increases as large as 150% being observed (Lyne et al. 2017). The most natural explanation is that during the on periods, plasma is generated that not only eventually produces the observed radio emission but also provides an additional spin-down torque due to the resulting current in the magnetosphere. This additional torque increases the spin-down rate over a state in the magnetosphere when the plasma generation is switched off (Kramer et al. 2006). These observations clearly provide evidence that the spin down is related to plasma currents in the magnetosphere as already discussed in Section 2. Similar to the initial proposal by Kramer et al. (2006), Li et al. (2012) modeled the off state using nearly vacuum conditions on the open field lines and nearly ideal force-free conditions on the closed field lines, where plasma can remain trapped even in the absence of active pair production. They find that toroidal advection of plasma in the closed zone in the off state causes spin downs that are compatible with the values observed.

The null periods in normal nulling pulsars are too short to measure a difference in spin down between the two emission states, but it can be expected that the phenomena of nulling and intermittency are related. If both phenomena are indeed related to a state change in the magnetosphere, then the spin down during a null will also be different. Going further, if the phenomenon of mode changes (moding; Section 5.2) is a similar signpost of a temporary reconfiguration of magnetospheric processes, then all three phenomena may be related. Lyne et al. (2010) showed for a sample of pulsars exhibiting moding, nulling, or intermittency that all behaved identically by showing a clear correlation between the spin down and the observed magnetospheric state changes. The extended monitoring of Lyne et al. (2010) revealed that even if pulsars switch states rapidly as in the case of moding or nulling, the fraction of time spent in the different states often varies with time, resulting in a visible long-term effect. Although moding and nulling seem to be related to intermittency, they clearly differ in the timescale and/or the magnitude of the changes in the magnetospheric currents. In particular, whereas pair production appears to cease in intermittent pulsars and probably nulling pulsars, plasma is still created continuously in moding pulsars.

Simultaneous radio and X-ray observations during nulls and mode changes have been conducted to look for observable consequences related to the heating of the polar cap as a result of the intermittent discharges and pair cascades discussed in Section 4.5.1. Unfortunately, PSR B1931+24 is too far away and deep in the Galactic plane, but studies were made of PSR B0823+26 (Hermsen et al. 2018), PSR B0943+10 (Hermsen et al. 2013, Mikami et al. 2016)

**Rotating radio transients (RRATs):** extreme class of nulling pulsars which show only sporadic pulses

and PSR B1822–09 (Hermes et al. 2017). All of them show mode changing by exhibiting a radio-bright and radio-weak mode each. Although no indication for synchronous X-ray and/or radio moding was found for PSR B1822–09, a clear synchronous radio and X-ray switching is seen for the former two pulsars. However, their respective behavior is seemingly contradictory. Pulsar B0943+10 is much more X-ray bright in its weak radio mode than when it is in its radio-bright mode (Hermes et al. 2013, Mikami et al. 2016). In contrast, PSR B0823+26 shows prominent pulsed X-ray emission when it is radio bright, but remains undetected when it is radio weak (Hermes et al. 2018). Obviously, the viewing geometry and moding timescales in all three cases are different, and there is no complete shutdown of radio emission, so that changes in the magnetospheric processes observed here may again be somewhat localized rather than necessarily global.

The above studies were made for nonrecycled pulsars, and it is naturally more difficult to detect such phenomena in much faster spinning recycled pulsars. Nevertheless, importantly, Lyne et al. (2010) demonstrated a close relationship between the change in spin-down rate and the magnitude of the rate itself, indicating that the spin-down rate changes by about 1% of its magnitude during switch. This implies that similar magnetospheric phenomena may also exist for millisecond pulsars. Even though changes would be smaller by five to seven orders of magnitude, and perhaps happening so fast that we cannot easily observe them, they may explain a low level of timing noise seen in a number of millisecond pulsars (e.g., Chalumeau et al. 2021).

Related to intermittent and nulling pulsars are the so-called rotating radio transients (RRATs), which are a subset of neutron stars that appear as sporadically repeating sources of radio pulses (Keane & McLaughlin 2011). At first thought to be a different class of neutron stars (McLaughlin et al. 2006), continued observation revealed that there is a characteristic underlying period associated with RRAT pulses that increases with time (McLaughlin et al. 2009). Keane et al. (2011) concluded that RRATs are therefore not a distinct and separate population but another extreme class of ordinary pulsars related to nulling or intermittent pulsars, which happen to be discovered more easily via their single pulsars rather than their periodicity due to the sporadicity of their emission. At the time of writing, more than 130 RRATs are known, about 30 of which have a measured spin-down derivative.<sup>24</sup> The range of cataloged periods and period derivatives places them toward the upper right corner of the  $P-\dot{P}$  diagram, continuing the distribution that is seen for intermittent and nulling pulsars as shown in the  $P-\dot{P}$  diagram in Section 6. We note that the identification of a source such as an RRAT is not always straightforward, as the detection of emission (or the lack thereof) depends on the sensitivity of the observing telescope (Keane & McLaughlin 2011), so that a pulsar with a high modulation in the single-pulse flux density may appear as an RRAT if observed from larger distances or with less sensitive telescopes (Weltevrede et al. 2006). Such a source is, for instance, J1554–5209, which was classified as an RRAT (even though it was occasionally detectable in periodicity searches and in every observation with the Parkes telescope; see Keane et al. 2011), whereas MeerKAT (Meer-Karoo Array Telescope) observations reveal continuous emission (S. Johnston, private communication).<sup>25</sup>

Overall a consistent picture appears to emerge that relates the phenomena of intermittent pulsars, nulling pulsars, and RRATs to the physical processes discussed in Section 4.5. We summarize this in Section 6 when we also discuss the  $P-\dot{P}$  diagram.

**5.3.4. The Vela Pulsar.** The pulsar is located in the Vela supernova remnant and has also been observed across the electromagnetic spectrum at optical, X-ray, and gamma-ray frequencies (see

<sup>24</sup>See <http://astro.phys.wvu.edu/rratalog/>.

<sup>25</sup>For this reason, we do not include this source in the  $P-\dot{P}$  diagram in Section 6.

**Figure 1).** At frequencies above 1 GHz, it is the brightest pulsar known. This is even the case at frequencies as high as 90 GHz (Liu et al. 2019), where the very high degree of polarization seen at low radio frequencies (nearly 100% linear polarization with significant circular polarization) has dropped to 20%. Across all radio frequencies, Vela shows the identical textbook-like S-like swing of the PA, inspiring the crucial development of the RVM (see Section 5.2.2) that was unambiguously validated by the observations of PSR J1906+0746 (see Section 5.3.2). Within the RVM, the absolute PA at the fiducial pulse phase (defined by the plane that contains spin axis, magnetic axis and the viewing vector of observer) can be identified with the direction of the spin vector projected on the plane of the sky. Studying this first in Vela (and then in other pulsars) indicated that young pulsars show an alignment between pulsar spin and velocity vector, which is most likely not caused by magnetospheric processes but by the birth event of pulsars (Johnston et al. 2005).

**Glitch:** step-like increase in rotational frequency mostly observed in young pulsars and presumably related to an internal reconfiguration of the neutron star's moment-of-inertia

Vela is also known for its frequent rotational glitches, i.e., sudden increases in spin frequency, presumably due to an exchange of angular momentum between the superfluid liquid in the interior and the solid crust of the neutron star during the release of pinned vorticity (e.g., Anderson & Itoh 1975). During a glitch registered on December 12, 2016, the pulsar was “caught in the act” by being observed with flux density, polarization, and single-pulse time of arrival measurements. During the glitch, the spin frequency was seen to increase by  $\Delta\nu/\nu = 1.431 \times 10^{-6}$  (Palfreyman et al. 2018). A glitch of this large size is not uncommon for Vela (Espinoza et al. 2021). Remarkably, however, Palfreyman et al. (2018) reported sudden changes in the pulsed emission coincident with the glitch event. The changes included a broadening of a pulse, a null for one period, and low linear polarization for two further pulses. Furthermore, for about 30 rotations, the pulses arrived later than expected from the preglitch timing model, before the increase in spin frequency became apparent. This is the first time that such a clear interaction between the neutron star interior and the magnetosphere was observed, and models have been proposed to explain how the radio emission was quenched during the event (Bransgrove et al. 2020, Yuan et al. 2021). Although some earlier results already seemed to link profile state changes to glitches in other pulsars (Weltevrede et al. 2011, Keith et al. 2013), Vela may well be the key for understanding the trigger of nulling, moding, and intermittency.

## 5.4. Old and New Ideas on Radio Emission and Propagation Effects

Our understanding of the physics of radio emission is still far from complete. In what follows, we revisit the current status of the key pieces of the theory and emphasize new advancements brought by modern magnetospheric models.

**5.4.1. Normal modes.** Whatever the emission mechanism is, only the radio waves corresponding to the normal modes allowed by the plasma can propagate and ultimately escape from the pulsar magnetosphere. Pulsar plasma supports a very limited set of eigenmodes because of the equal masses of electrons and positrons and because in strong fields charged particles can only move along the magnetic field lines. Under the simplest assumption of cold plasma, the wave dispersion relation in the rest frame of the plasma is  $(\omega^2 - c^2 k^2) \cdot [(\omega^2 - c^2 k_{\parallel}^2)(1 - \omega_p^2/\omega^2) - c^2 k_{\perp}^2] = 0$ , where  $\omega_p$  is the plasma frequency,  $\omega$  is the frequency of the wave, and  $k_{\parallel}$  and  $k_{\perp}$  are the wave vector components parallel and perpendicular to the background magnetic field, respectively (Arons & Barnard 1986, Beskin et al. 1993). Here, all quantities are calculated in the rest frame of the plasma that streams along the magnetic field lines at Lorentz factor  $\gamma_{\text{sec}}$ . We assumed the limit of infinite magnetic field strength,  $\omega_B \gg (\omega_p, \omega)$ , which is appropriate in the inner magnetosphere. For the propagation at an angle with respect to the background magnetic field, this equation describes

**X-mode:** normal mode with the electric field vector being perpendicular to the wave vector and the background magnetic field

**O-mode:** normal mode in highly magnetized plasma with the electric field vector in the plane of the wave vector and the background magnetic field

**Landau damping:** damping of subluminal waves caused by interaction with plasma particles with velocities close to the phase speed of the wave

three linearly polarized waves<sup>26</sup>: extraordinary, X-mode, and  $\omega = ck$ , with the electric field vector being perpendicular to both the wave vector,  $\mathbf{k}$ , and the background magnetic field,  $\mathbf{B}$ , and two modes on the ordinary, O-mode, branch. The ordinary branch consists of the superluminal mode and the subluminal Alfvén mode, with the electric field in the  $\mathbf{k}$ - $\mathbf{B}$  plane. Polarization of the X-mode identifies it as the fast magnetosonic wave of FFE, which freely propagates across magnetic field lines. This mode cannot be excited by the longitudinal (along the field lines) plasma currents. The Alfvén mode propagates along magnetic field lines and suffers from Landau damping for oblique propagation, i.e., nonzero  $k_{\perp}$  (Arons & Barnard 1986). The superluminal O-mode is not damped by the Landau mechanism, so it can freely propagate in the pulsar plasma. At small angles between the direction of propagation and the background magnetic field, the O-mode is quasi-longitudinal and is significantly affected by the plasma. As the O-mode wave propagates in a plasma of decreasing density, and as the angle between the wave propagation and background magnetic field increases, it becomes a freely propagating electromagnetic mode. Thermal effects lead to quantitative corrections to the wave dispersion but do not change the qualitative behavior of the modes (Rafat et al. 2019, Mikhaylenko et al. 2021). Thus, the extraordinary X-mode and the superluminal O-mode are the building blocks of the observed OPMs.

**5.4.2. Propagation effects.** The presence of dense pair plasma in the pulsar magnetosphere makes the interaction between the plasma and radio waves unavoidable. Accounting for the polarized transfer of waves through the plasma is necessary to compute the characteristics of the outgoing radiation (Lyubarskii & Petrova 1999, Wang et al. 2010, Beskin & Philippov 2012). As long as the emission is produced well within the light cylinder, the normal modes of the plasma are linearly polarized. The X-mode propagates along the straight line, but the superluminal O-mode has to experience substantial refraction (Barnard & Arons 1986). It happens deep inside the magnetosphere, where the angle between the wave propagation and the background magnetic field is small, and the O-mode properties have significant plasma corrections. Here, the characteristic scales are larger than the radiation wavelength, so the geometrical optics approximation holds. Qualitatively, waves of smaller frequencies refract more strongly, because deviations of the refractive index from unity are larger, leading to a broader pulse width. Quantitatively, results are sensitive to the gradients of the plasma density transverse to the magnetic field lines (Lyubarskii & Petrova 1999), which are most uncertain. Improvements in modeling refraction are of importance, because the observed pulse width and its dependence on frequency are significantly affected, and may in fact be entirely dominated, by the refraction in the magnetosphere (Beskin et al. 1993, Lyubarskii & Petrova 1999). Availability of numerical 3D magnetospheric structure, as well as future more accurate understanding of the nonuniformity of the plasma flow, should facilitate further progress.

In the vicinity of the emission point, and ignoring the curvature of the magnetic field, the normal modes propagate independently, and their polarization quickly adjusts to the orientation of the  $\mathbf{k}$ - $\mathbf{B}$  plane, in agreement with the geometrical optics approximation. Along the trajectory, the angle between the wave vector and the magnetic field increases due to magnetic line curvature, and the plasma density decreases. When the radiation enters into the region of a sufficiently low-density plasma, the wave polarization decouples from the orientation of the external magnetic

<sup>26</sup>Formally, in the rest frame of the plasma there are three waves propagating away from the pulsar and three identical waves propagating toward it. In the laboratory (pulsar) frame, one of the backward-propagating waves in the plasma frame may transform into an additional forward-propagating wave (Beskin et al. 1993), making the total amount of forward-propagating waves to be four (superluminal O-mode, X-mode, and two Alfvén-like subluminal waves); see recent discussion by Rafat et al. (2019) and Mikhaylenko et al. (2021).

field. This implies that the geometrical optics approximation conditions become inapplicable at a certain distance. This phenomenon is known as the limiting polarization effect (Budden 1952, Zheleznyakov 1970). The polarization-limiting radius,  $r_p$ , where polarization freezes, can be estimated from the relation:  $k(\Delta n) \sim d\beta_B/dr$ , where  $\Delta n$  is the difference between the refractive indexes of the O- and X-modes,  $k$  is the wavenumber, and angle  $\beta_B$  defines the orientation of the magnetospheric magnetic field in the plane perpendicular to the direction of the wave propagation. Quantitative estimates for the plasma parameters expected in young pulsars give  $r_p/R_* \sim 1.6 \times 10^3 (\lambda/10^4)^{2/5} (\gamma_{sec}/10^2)^{-6/5} (B_*/10^{12} \text{ G})^{2/5} (\nu/1 \text{ GHz})^{-2/5} (P/0.1 \text{ s})^{-1/5}$ . When this condition is satisfied, the length scale for the beat between the normal modes,  $\sim 1/(k\Delta n)$ , becomes comparable with the scale of variations in the plasma and the field characteristics, and the normal modes are no longer independent. As a result, mode coupling occurs, and the escaping emission becomes partially circularly polarized (Cheng & Ruderman 1979).<sup>27</sup> The PA of the escaping radiation is then roughly determined by the orientation of the magnetospheric magnetic field at the polarization-limiting radius.

Radiative transfer simulations allow calculations of the properties of the outgoing radiation, i.e., PA swing and circular polarization, self-consistently (Wang et al. 2010, Beskin & Philippov 2012). Naturally, significant deviations in the PA swing from the RVM are accompanied by a high circular polarization, as both are the consequences of a mode coupling. For typical plasma parameters, the degree of circular polarization is in the range of 1–10%, which is consistent with observations. The observed phase shift of the PA swing due to aberration (Blaskiewicz et al. 1991) is attributed to the  $\mathbf{E} \times \mathbf{B}$  drift of the plasma particles in the polarization-limiting radius. It leads to a shift of the polarization ellipse with respect to the magnetic field orientation in the plane transverse to the ray propagation (Lyubarskii & Petrova 1999, Beskin & Philippov 2012). Numerical calculations show that in most cases the sign of the circular polarization is symmetric across the pulse and is determined by the sign of the derivative of the PA swing, which is consistent with the general trend observed by Johnston & Kramer (2019) and observations of J1906+0746 (see Section 5.3.2). The sometimes observed asymmetrical profile of the circular polarization, i.e., changing its sign near the center of the pulse, can also be reproduced (e.g., Hakobyan et al. 2017, their figures 2 and 3). This is because the change in the PA swing due to aberration, dominant in the outer magnetosphere, leads to a different sign of the circular polarization compared to the change in the PA due to the varying magnetic field orientation. Because the plasma density is nonuniform across the magnetic field lines, the polarization-limiting radius is phase-dependent, and both effects can be at play separately at different phases. Simulations show that the PA shift due to aberration weakly depends on frequency, and this aligns with the observational evidence.

Large RVM-like PA swings observed in many normal pulsars favor a small polarization-limiting radius. For example, polarized transfer modeling by Galishnikova et al. (2020) of different observational epochs of J1906+0746 requires a somewhat low plasma multiplicity value,  $\lambda \sim 10^3$ , to match both the circular polarization at  $\sim 5\%$  level and a perfect S-like PA swing. The most likely explanation is a significant cross-field nonuniformity of the plasma flow; i.e., the

---

<sup>27</sup>An alternative explanation of the partially circular polarization is the dispersive property of a not completely symmetric pair plasma, i.e., the distribution functions of positrons and electrons being not identical, in a finite magnetic field (von Hoensbroech et al. 1998b). The normal modes propagating at small angles to the magnetic field are circularly polarized; however, well inside the magnetosphere the magnetic field strength is so high that this effect is small (Petrova & Lyubarskii 2000). In fact, numerical calculations that take into account both effects show that the circular polarization from the mode coupling completely dominates over the prediction from the properties of normal modes (Beskin & Philippov 2012).

polarization may be freezing at lower altitude if the emission escapes through the local underdense plasma zone, which can be seen as effectively lower density of a uniform flow. In compact magnetospheres of millisecond pulsars the polarization-limiting radius is inevitably located in the vicinity of the light cylinder, where the magnetic field becomes progressively toroidal. The implication is a flat PA swing (Barnard 1986, Beskin & Philippov 2012), in agreement with observations described in Section 5.2.5.

Radio waves can be absorbed because of the cyclotron absorption, which happens when the wave frequency in the particle rest frame is close to the cyclotron frequency,  $\gamma\omega(1 - \beta\cos\theta_{\text{res}}) = \omega_B$  (Blandford & Scharlemann 1976, Mikhailovskii et al. 1982). Here,  $\beta$  and  $\gamma$  are the velocity and Lorentz factor of resonant particles, respectively, and  $\theta_{\text{res}}$  is the angle between the wave propagation and external magnetic field at the resonance radius,  $r_{\text{res}}/R_* \sim 2 \times 10^3 (B_*/10^{12} \text{ G})^{1/3} (\nu/1 \text{ GHz})^{-1/3} \gamma^{-1/3} \theta_{\text{res}}^{-2/3}$ . The optical depth to this process,  $\tau \sim \lambda(1 - \cos\theta_{\text{res}})(r_{\text{res}}/R_L)$ , appears to be large,  $\sim 100$ , when assuming the plasma outflow to be uniform across the field lines. However, near the magnetic pole the plasma creation is suppressed because of the inefficient curvature radiation. In a rotating magnetosphere, a significant amount of ray trajectories escape through this hole in the plasma density, eliminating the catastrophic absorption issue (Beskin & Philippov 2012). For a quasi-symmetric pulsar plasma, i.e., the electrons and positrons having almost identical densities and distribution functions, the cyclotron absorption almost does not affect polarization characteristics (Wang et al. 2010, Beskin & Philippov 2012).

To conclude, the basic physics of propagation effects inside the magnetosphere is well understood. However, it is fair to claim that more detailed, quantitative comparisons with observations of particular sources, especially of the frequency evolution of polarization characteristics (such as shown in Figure 13), are still lacking.

**5.4.3. Radio emission mechanisms.** Since the 1970s, three classes of emission mechanisms from the inner magnetosphere were discussed: (a) coherent curvature radiation by charged bunches, (b) maser amplification of curvature radiation and related plasma instabilities associated with the plasma flow along the curved magnetic field lines, and (c) nonlinear conversion of waves produced by the beam-plasma instabilities (Ginzburg & Zhelezniakov 1975, Melrose 2017). Here, we summarize these ideas and their criticisms. A more thorough analysis of these ideas as general mechanisms for pulsar radio emission can be found in recent papers by Melrose (2017) and Melrose et al. (2021b).

The first class envisions that charged bunches of particles are somehow formed in the outflow in the open field line region, and the large number of particles in the bunch collectively emits curvature radiation in phase. The frequency of curvature radiation corresponds to the radio range for the Lorentz factor of the secondary plasma,  $\gamma_{\text{sec}} \sim 100$ . Despite the attractiveness, there are many severe theoretical problems with this approach (e.g., Melrose 1981, Melrose et al. 2021b). Most of the studies simply postulate the formation of bunches, and ignore that, even if they somehow form and can be maintained, their radiation is suppressed by the surrounding plasma.<sup>28</sup> The least controversial models involve formation of charged solitons as a result of two plasma instabilities: a beam-driven instability that generates Langmuir-like waves, and a modulational instability that leads to these waves forming solitons (e.g., Melikidze et al. 2000). It is questionable whether the assumed beam instability is efficient (see below).

A more self-consistent approach, that of the second class, is focused on identifying a possible plasma instability in the outflow that can lead to maser amplification of the curvature radiation.

---

<sup>28</sup>Recently, similar ideas were applied to the coherent emission of FRBs. Serious theoretical problems of this model are extensively discussed by Lyubarsky (2021).

This can happen if a seed wave, which satisfies the dispersion relation in the medium, triggers currents that emit in phase with the seed wave, which leads to its amplification. In principle, this is possible (Blandford 1975, Melrose 1978, Zheleznyakov & Shaposhnikov 1979, Chugunov & Shaposhnikov 1988, Luo & Melrose 1992). Goldreich & Keeley (1971) found an instability for the flow of plasma along the infinitely strong circular magnetic field. Asseo et al. (1983) and Larroche & Pellat (1987) argued that the instability develops only if the flow is sharply bounded and that the necessary conditions are unlikely to be satisfied in pulsars. Beskin et al. (1988b) derived the dielectric tensor of an inhomogeneous cold plasma in the infinitely strong magnetic field and found unstable modes. Their approach has been criticized (Larroche & Pellat 1987, Nambu 1989, Machabeli 1991), although most of the criticism has been rigorously addressed (Beskin et al. 1988a, Istomin 1994, Nambu 1996, Bornatici & Kravtsov 2000). Among other problems (see, e.g., Lyutikov 2021), even a small velocity dispersion was argued to significantly suppress coherent curvature radiation (Melrose 1992, Melrose & Gedalin 1999, Melrose et al. 2021b). To conclude, a universally accepted solution has never appeared for this class of proposed mechanisms.

There exists a more straightforward instability associated with the motion of relativistic plasma particles in the curved magnetic field (Zheleznyakov & Shaposhnikov 1979). As particles stream away from the pulsar, they experience acceleration directed toward the local center of curvature of the field line. The acceleration is due to the component of the Lorentz force associated with the curvature drift velocity,  $\beta_{\perp,c} = \gamma m_e c^2 / eBR_c$ , the latter being directed across the field lines. The outflow consisting of the primary highly relativistic beam,  $\gamma_b \sim 10^7$ , and the secondary plasma can be unstable to a curvature-drift instability. It may lead to the wave growth when the subluminal mode of the secondary plasma gets into the resonance with the low-density, high-energy beam particles,<sup>29</sup> i.e.,  $\omega = kc(1 - \delta) = \mathbf{k} \cdot \mathbf{v}_b \sim kc(\beta_{\perp,c} \sin \theta + \beta_{\parallel,b} \cos \theta)$ . Here,  $\beta_{\parallel,b} = (1 - \beta_{\perp,c}^2 - 1/\gamma_b^2)^{1/2}$  is the beam velocity component along the magnetic field;  $\omega$  and  $k$  are the frequency and the wave vector, respectively;  $\theta \ll 1$  is the angle of propagation with respect to the magnetic field; and  $\delta \sim \omega_p^2 / (4\omega_B^2 \gamma_s^3) \ll 1$  is the difference between the phase speed of the normal mode and the speed of light for a nearly aligned propagation (Kazbegi et al. 1991, Lyutikov et al. 1999). The optimal conditions for the instability are achieved near the light cylinder, where the drift velocity and  $\delta$  are maximal. Kaganovich & Lyubarsky (2010) show that even though the waves could be amplified, the amplification factor remains small, and this mechanism is not a viable option to explain pulsar emission.

In the models of the third class, it is thought that the beam-plasma (or a streaming-type; some of these scenarios were recently explored with PIC simulations by Benáček et al. 2021a,b) instability powers subluminal waves through resonances,  $\omega = \mathbf{k} \cdot \mathbf{v}_b$ . These waves are then converted to the escaping modes via various nonlinear processes or inhomogeneities (e.g., Istomin 1988, Lyubarskii 1996a). There are three scenarios for the beam formation in the open field line region: (a) the primary beam moving through the secondary plasma, (b) relative streaming between secondary positrons and electrons associated with the magnetospheric current, and (c) overlap of distinct plasma clouds. However, the instability growth rates and the inhomogeneous structure of the outflowing plasma lead to further constraints. The growth rate in the first scenario is severely suppressed by the large Lorentz factor of the beam,  $\gamma_b \sim 10^7$ , which makes the instability too slow to grow within the light cylinder. The large thermal spread of particle distributions suppresses the instability in the second scenario (Benford & Buschauer 1977). Assuming a strongly nonsteady pair creation produces separate plasma clouds, the third scenario involves

<sup>29</sup>This and other instabilities discussed in this section are of the same Cherenkov type; i.e., they involve a particle beam that moves faster than a normal mode of the plasma.

faster particles in a trailing cloud (which can be considered as a beam) overtaking slower particles in a leading cloud (considered as a background plasma). Melrose et al. (2021b) show that for realistic spreads of particle distribution functions in the clouds, i.e.,  $\langle \gamma \rangle \leq 10$  in the rest frame of the secondary plasma, it is problematic to form a powerful enough beam within the light cylinder.

Recent ideas by Philippov et al. (2020) and Melrose et al. (2021a), motivated by the progress in numerical modeling of nonstationary discharges, discuss emission mechanisms that directly produce superluminal O-mode waves. Using local 2D simulations of the polar cap discharge, Philippov et al. (2020) showed that the nonsteady discharge produces broadband electromagnetic emission. Parallel, field-aligned, electric field fluctuations are naturally produced during screening of the electric field by freshly produced plasma (already observed in 1D discharge simulations by Timokhin 2010 and Timokhin & Arons 2013). The nonuniformity of pair production across the magnetic field lines results in inhomogeneity of the parallel electric field, which in turn leads to the creation of a fluctuating perpendicular component of the magnetic field and excitation of an electromagnetic wave (see **Figure 9**). This wave is a superluminal O-mode, which naturally transforms into an escaping electromagnetic wave as the plasma density drops along the wave trajectory. The nonuniformity of pair production is most pronounced near polar cap edges (where the accelerating electric field sharply jumps at the return current layer) and near magnetic poles (where the radius of curvature of magnetic field lines rapidly approaches infinity), which makes these regions the most efficient generators of radio emission (Philippov et al. 2020; see also Cruz et al. 2021).

The spectrum and the power of the O-mode emission are controlled by the dynamics of the discharge. As the pair formation in the discharge continues, the skin depth decreases, and the range of wavelengths of the produced waves increases. Hence, the emergent coherent radiation from a highly nonuniform pair cloud will be broadband. The highest frequency of coherent radiation produced by this mechanism can be roughly estimated as  $v \simeq \sqrt{4\pi e^2 \kappa n_{\text{GJ}}(1/\gamma^3)/m_e}/2\pi \approx 30\sqrt{\kappa_5 B_{12}/[(r/2R_*)^3 P_{0.1} \gamma_{10}^3]} \text{ GHz}$ , where  $\kappa_5$  is the final pair multiplicity normalized to  $10^5$ ,  $B_{12} = B/10^{12} \text{ G}$ ,  $P_{0.1} = P/0.1 \text{ s}$ ,  $r$  is the distance from the neutron star, and  $\gamma_{10} = \gamma/10$  is the Lorentz factor of final pair generation. 2D PIC simulations with the reduced scale separation show that a typical radio luminosity is in the range of  $10^{-6}\text{--}10^{-4}L_0$ , where  $L_0$  is the spin-down luminosity (Philippov et al. 2020, Cruz et al. 2021). A detailed 1D theory of the discharge shows that this estimate persists for realistic pulsar parameters (Tolman et al. 2022).

Melrose et al. (2021a) discuss superluminal O-mode waves excited by current imbalances in the magnetosphere. These waves are emitted strictly along magnetic field lines and experience refraction in cross-field-inhomogeneous plasma. They become oblique and escape as electromagnetic waves as the plasma density drops along their trajectory.

The observed emission in the X-mode should be a result of propagation effects. Proposed explanations are the mode coupling in the curved magnetic field close to the emission point (Gil et al. 2004) and linear mode conversion in the regions of the quasi-parallel (with respect to the local magnetic field) propagation, where refractive indexes of modes are close to each other (Petrova 2001). The observed widths of pulsar profiles, which imply observed emission heights significantly above the stellar surface, should be substantially affected by refraction in the magnetosphere. To summarize, the new ideas relying on the nonlinear dynamics of the pair cascade hold promise to explain the coherent radio emission from first principles. The detailed quantitative predictions using 3D simulations and extrapolations across the pulsar population, including millisecond pulsars, will be a subject for the active theoretical work in the next decade.

**5.4.4. Radio emission from the outer magnetosphere.** Observations of radio emission at the same rotational phase as the high-energy emission in some pulsars call for a separate radio

radiation mechanism, which operates in the outer magnetosphere. Because this emission is sometimes resolved into giant pulses, and into high-power nanoshots in the case of the Crab pulsar (see Section 5.3.1), the underlying physical process is intrinsically nonstationary.

When considering plasma instabilities in the outer magnetosphere, one has to study the limit of finite magnetic field, which extends the range of possibilities. A prominent case is the beam-driven instability at the anomalous-cyclotron resonance,  $\omega - k_{\parallel}v_{\parallel} = -\omega_B/\gamma_b$  (Kazbegi et al. 1991, Lyutikov et al. 1999).<sup>30</sup> The instability is driven by the transverse gradient of the distribution function in the momentum space,  $\partial f / \partial p_{\perp} < 0$ , which is satisfied for the radiatively damped 1D distributions in the magnetosphere. However, in the open field line region, the frequency of resonantly excited waves,  $\omega \sim \omega_B/(\delta\gamma_b)$ ,  $\delta \ll 1$ , turns out to be too high even for the primary beam,  $\gamma \sim \gamma_b \sim 10^7$  (e.g., Melrose 2017). It is interesting to explore whether similar instabilities can be efficiently excited in the return current layer, where there is a multistreaming particle distribution, and thus the properties of the normal modes can be quite different. Although emission of multiple resonant harmonics seems appealing to explain the zebra pattern in the HFIP of the Crab (Lyutikov 2007), the very high number of bright observed bands,  $\sim 30$ , seems implausible to be explained by this mechanism. It is unclear whether the zebra pattern is a feature of the emission mechanism or a consequence of propagation effects.

Lyubarsky (2019) and Philippov et al. (2019) proposed a new mechanism that powers coherent radiation from the current sheet. This emission appears in phase with the high-energy emission produced by particles accelerated in the current sheet, i.e., gamma rays, in agreement with observations of the Crab and other pulsars with very high magnetic field strengths at the light cylinder showing phase-aligned radio and high-energy emission. The basic physics here is as follows. As we discuss in Section 4.5.2, the current sheet beyond the light cylinder gets fragmented into a dynamic chain of plasmoids, which undergo successive coalescence. Mergers of sufficiently large plasmoids produce secondary perpendicular current sheets, which also get fragmented. Coherent emission is then produced by time-dependent plasma currents that appear at the interfaces of merging plasmoids. Collisions of plasmoids with each other and with the upstream magnetic field eject fast-magnetosonic (i.e., X-mode) waves, which propagate upstream across the background field and successfully escape from the plasma as electromagnetic waves. The model naturally produces pulses with  $v\tau \sim \text{few}$ , where  $v$  is the typical frequency and  $\tau$  is the pulse duration, which is reminiscent of observed nanoshots in the Crab pulsar. Mergers of big, monster-type, plasmoids produce secondary current sheets and emit clumps of nanoshots, potentially explaining the observed micropulses in the Crab's MP and LFIP. The frequency of the observed radiation in the comoving frame of the upstream plasma is set by the typical size,  $a' \sim 10 \text{ m} (B_{LC}/10^6 \text{ G})^{3/2}$  (Uzdensky & Spitkovsky 2014, Lyubarsky 2019), of small plasmoids in the chain,  $v \propto c/a'$ . In the pulsar frame it was shown to fall into the GHz range for the magnetic field at the light cylinder of order  $B_{LC} \sim 10^6 \text{ G}$ . For smaller magnetic field strength, the radiative compression of plasmoids is less significant, which makes their size larger, and produces smaller characteristic frequencies. This potentially explains why giant pulse-type emission in phase with gamma rays has been only observed from pulsars with a high field strength at the light cylinder (see the  $P-\dot{P}$  diagram in Section 6). The model also reproduces the observed brightness temperatures. The observed circular polarization of nanoshots can be a natural consequence of propagation effects (see Section 5.4.2), which for high- $B_{LC}$  pulsars implies that the limiting-polarization radius is located beyond the

---

<sup>30</sup>An important difference with instabilities discussed in Section 5.4.3 is that anomalous-cyclotron instability involves a change in the pitch angle: During the wave growth, particles in the beam undergo a transition up in Landau levels, which is impossible in the inner magnetosphere.

light cylinder. As pointed out in Section 5.3.1, optical (Shearer et al. 2003) and recent NICER X-ray (Enoto et al. 2021) observations show an increase of  $\sim 4\%$  in the luminosity of the Crab coincident with the giant pulse arrivals, indicating significantly larger total energy release than the one measured in radio and favoring magnetic reconnection in the current sheet beyond the light cylinder as the powering mechanism.

## 6. A SUMMARY OF OUR UNDERSTANDING, ITS LIMITS, AND OUTLOOK

In this review, we focused on the structure of the inner magnetosphere of pulsars and their observed radiation across the electromagnetic spectrum. Over the past 20 years, there was a lot of exciting progress on many long-standing questions, such as magnetospheric electrodynamics and origin of the high-energy emission. It seems possible that soon the origin and properties of the coherent radio emission may be understood. Few very important issues, such as the origin of the shutdown or reconfiguration of magnetospheric processes and associated observed timescales, are yet to be addressed.

Our understanding of the observed population is summarized in the  $P$ – $\dot{P}$  diagram (Figure 17). The region bounded by the conditions  $10^{11} \text{ G} < B_* < 10^{13} \text{ G}$  (the polar field strength is computed as described in Section 2) and  $l_{\text{gap}} < R_{\text{pc}}$  contains nonrecycled energetic pulsars that were shown to sustain nearly force-free magnetospheres and efficient pair discharges near the stellar surface. The most energetic pulsars in this group, and millisecond pulsars with large  $B_{\text{LC}}$ , also efficiently produce pairs in the reconnecting current sheet beyond the light cylinder. Magnetospheres of pulsars in this group are described by the theory and PIC simulations summarized in Section 4.5. This population includes all young *Fermi*-detected pulsars. Discharges in nonrecycled pulsars below the line  $l_{\text{gap}} = R_{\text{pc}}$  are intrinsically not 1D and, perhaps, prone to intermittent behavior on longer timescales. In this respect, it is interesting to note that all intermittent pulsars, pulsars showing nulling behavior (with firmly established nulling fractions larger than 2%) and RRATs, except one source, nulling pulsar B1822-14, are located below the line  $l_{\text{gap}} = 0.5R_{\text{pc}}$ . It remains to be seen how pair production couples to the global electrodynamics of the magnetosphere for conditions in old nonrecycled and millisecond pulsars.

Among issues we did not cover are the impact and connection of magnetospheric processes to observed spin-down properties and pulsar evolution. Although the picture of slowing down the pulsar rotation through the emission of powerful electromagnetic wind supported by plasma currents is robust, the old and well-known problem of predicting the braking index,  $n_{\text{br}} = \Omega\ddot{\Omega}/\dot{\Omega}^2$ , is still not solved. Here, magnetospheric models with constant inclination predict  $n_{\text{br}} = 3$ , whereas observations of young pulsars show  $n_{\text{br}} < 3$  (e.g., Lyne & Graham-Smith 2006) but also very much larger values (e.g., Parthasarathy et al. 2020). A related question is the evolution of the inclination angle, where consideration of only the magnetospheric torque implies alignment (Philippov et al. 2014), i.e., the angle between the dipole moment and rotational axis approaching zero as the pulsar ages. The observational clues are controversial; i.e., a seeming statistical tendency for alignment (Tauris & Manchester 1998, Johnston & Karastergiou 2017) and for pulsars with small inclination angles to be older pulsars (Maciesiak et al. 2011) coexists with the observed evidence of counter-alignment in the Crab pulsar (Lyne et al. 2013; see Section 5.3.1). The most likely key here is the dynamics of the internal magnetic field and not the magnetospheric physics. For example, a likely origin of the braking index discrepancy is the evolution of the internal dipole moment in young pulsars, i.e., its potential increase (e.g., Ruderman et al. 1998). The details of the magnetic field evolution have begun to be rigorously investigated (e.g., Gourgouliatos et al. 2016, Bransgrove et al. 2018).

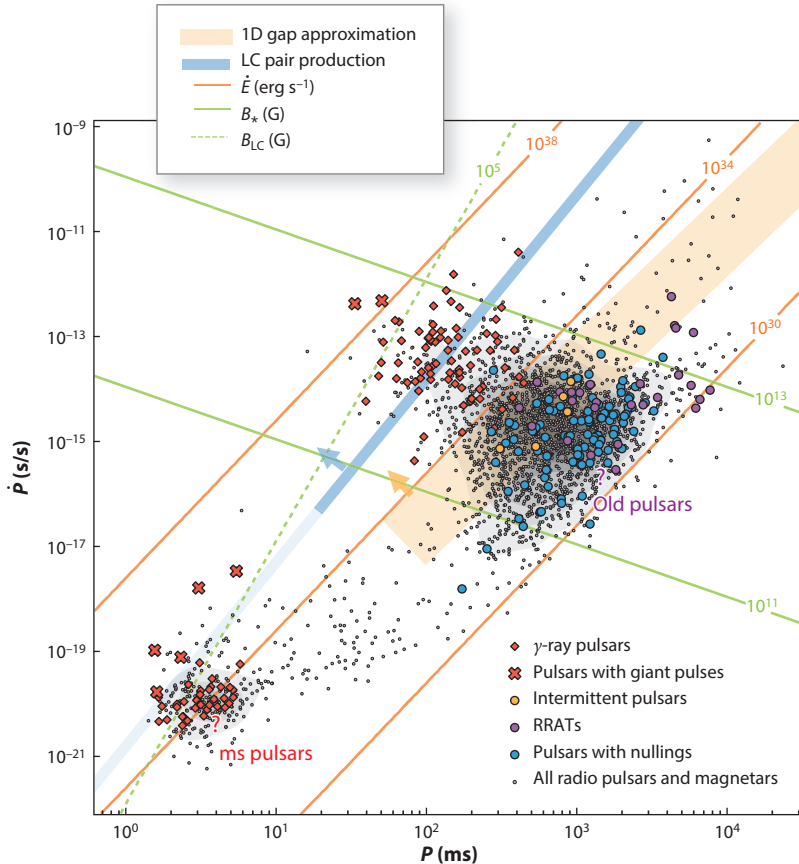


**Figure 17**

$P-\dot{P}$  diagram of the observed neutron stars. Specific populations are shown with different symbols. Green solid lines show the values of the surface field,  $B_*$  =  $10^{11}$  G and  $B_*$  =  $10^{13}$  G, which bound the region where the theory of polar discharge summarized in Section 4.5 is applicable. Green dashed line represents the condition  $B_{LC} = 10^5$  G, which bounds the population of pulsars observed to emit giant radio pulses. Discharge in nonrecycled pulsars above the orange stripe, given by the condition  $0.5R_{pc} < l_{gap} < R_{pc}$ , can be described using the 1D approximation. We note that all intermittent pulsars, pulsars showing nulling behavior and RRATs, except one source, nulling pulsar B1822-14, are located below the line  $l_{gap} = 0.5R_{pc}$ . Pulsars above the blue line produce pair multiplicities in the excess of  $10^4$  in their current sheets. Abbreviations: LC, light curve; RRAT, rotating radio transient.

Up to now, observations have been used to demonstrate the role of magnetospheric currents contributing to and modifying pulsar spin down and contributing to observed timing noise. With sufficient theoretical understanding, combined with increased cadence to pinpoint moments of state change, one should be able to turn this around and account for the different spin-down rates and apply this information to a retrospective addition to the timing model (see Lyne et al. 2010). This would turn even young and noisy pulsars into stable clocks. This first-order correction may then open up avenues to look even deeper, e.g., into the temporal behavior of single pulses including nulling, moding, and general subpulse phenomena. Eventually, models to explain the fundamental emission features, for instance, as polarized shot noise (Cordes 1976, Jenet et al. 2001, Jessner et al. 2010), could be addressed. Upcoming work demonstrates that timing studies

of the gamma-ray photons received by *Fermi* allow one to isolate intrinsic spin noise from interstellar medium effects (A. Parthasarathy & M. Kerr, private communication), so that even for these aspects there will be true synergies between radio and high-energy observations. Nearing the 60-year anniversary of the discovery of pulsars, we are closer to understanding pulsars and their magnetospheres than ever before.

## SUMMARY POINTS

1. Magnetospheric structure of young energetic pulsars is now understood using force-free and first-principles kinetic simulations.
2. The observed high-energy incoherent radiation is likely produced in the current sheet beyond the light cylinder.
3. Observationally, there are at least two different radio emission mechanisms. One operates in the inner magnetosphere, whereas the other one works near the light cylinder and is specific to pulsars with the high magnetic field strength in that region.
4. Radio emission from the inner magnetosphere is intrinsically connected to the process of pair production, and its observed properties contain the imprint of both the geometrical (e.g., rotating vector model behavior of the position angle swing) and propagation effects (e.g., significant circular polarization) through the magnetospheric plasma.
5. Nonstationary dynamics of pair discharge in the polar cap and of magnetic reconnection in the current sheet beyond the light cylinder are the most plausible causes of the coherent radiation.

## FUTURE ISSUES

1. Improving the realism of simulation models of pair discharges and reconnection is crucial to make further quantitative connections with observations.
2. Extending first-principles simulation models to old nonrecycled and millisecond pulsars, and transient magnetars, is important to understand how their magnetospheres get filled with pair plasma and how their observed emission is produced.
3. Building a first-principles model of radio emission, which takes into account the radiation mechanism, propagation effects, and magnetospheric structure, is necessary to explain the main observed characteristics.
4. Understanding the various observed timescales from basic principles must be established.
5. Future observations in the high-frequency radio (i.e., with the Atacama Large Millimeter/submillimeter Array), MeV, and TeV bands, simultaneous radio and X-ray observations, and measurements of the polarization of emission at high energies are critical to verify and extend our understanding of pulsar magnetospheres.

## DISCLOSURE STATEMENT

The authors are not aware of any affiliations, memberships, funding, or financial holdings that might be perceived as affecting the objectivity of this review.

## ACKNOWLEDGMENTS

A.P. thanks J. Arons, A. Beloborodov, V. Beskin, A. Jessner, Y. Lyubarsky, A. Spitkovsky, A. Timokhin, and D. Uzdensky for enlightening discussions on related topics over the years, and group members A. Chernoglazov, A. Galishnikova, H. Hakobyan, J. Mahlmann, J. Nättlä, B. Ripperda, and L. Tolman for reading various versions of this review during its preparation. M.K. is grateful to V. Beskin, J. Cordes, J. Gill, F. Graham-Smith, A. Jessner, S. Johnston, A. Karastergiou, E. Keane, H. Lesch, D. Lorimer, A. Lyne, R. Manchester, D. Mitra, A. Parthasarathy, J. Rankin, J. Seiradakis, B. Stappers, and K. Xilouris for countless stimulating discussions in the past and present, making pulsar emission a fun topic to study just because of that. M.K. thanks A. Jessner, S. Johnston, and A. Karastergiou for comments on the manuscript and the MeerKAT TPA team for providing updated information on nulling pulsars prior to publication. Research at the Flatiron Institute is supported by the Simons Foundation. This research is supported by the Max-Planck Society (MPG).

## LITERATURE CITED

- Abdo AA, Ackermann M, Ajello M, et al. 2009. *Ap. J. Suppl.* 183(1):46–66
- Abdo AA, Ackermann M, Ajello M, et al. 2010. *Ap. J. Suppl.* 187(2):460–94
- Abdo AA, Ajello M, Allafort A, et al. 2013. *Ap. J. Suppl.* 208(2):17
- Abdollahi S, Acero F, Ackermann M, et al. 2020. *Ap. J. Suppl.* 247(1):33
- Anderson PW, Itoh N. 1975. *Nature* 256:25–27
- Ansoldi S, Antonelli LA, Antoranz P, et al. 2016. *Astron. Astrophys.* 585:A133
- Arons J. 1983. *Nature* 302:301–5
- Arons J. 2009. In *Neutron Stars and Pulsars*, ed. W Becker. *Ap. Space Sci. Libr.* 357:373–420
- Arons J, Barnard JJ. 1986. *Ap. J.* 302:120
- Arons J, Scharlemann ET. 1979. *Ap. J.* 231:854–79
- Asseo E, Pellat R, Sol H. 1983. *Ap. J.* 266:201–14
- Baade W, Zwicky F. 1934. *Phys. Rev.* 46:76–77
- Bacchini F, Ripperda B, Philippov AA, Parfrey K. 2020. *Ap. J. Suppl.* 251(1):10
- Backer DC. 1970a. *Nature* 228:42–43
- Backer DC. 1970b. *Nature* 228:752–55
- Backer DC. 1970c. *Nature* 228:1297–98
- Backer DC, Fisher JR. 1974. *Ap. J.* 189:137–45
- Backer DC, Kulkarni SR, Heiles C, Davis MM, Goss WM. 1982. *Nature* 300:615–18
- Bai XN, Spitkovsky A. 2010. *Ap. J.* 715(2):1282–301
- Bailes M, Johnston S, Bell JF, et al. 1997. *Ap. J.* 481:386–91
- Barnard JJ. 1986. *Ap. J.* 303:280–91
- Barnard JJ, Arons J. 1986. *Ap. J.* 302:138–62
- Becker W. 2009. In *Neutron Stars and Pulsars*, ed. W Becker, *Ap. Space Sci. Libr.* 357:91–140
- Becker W, Trümper J. 1997. *Astron. Astrophys.* 326:682–91
- Beloborodov AM. 2008. *Ap. J. Lett.* 683(1):L41–44
- Beloborodov AM. 2017. *Ap. J.* 850(2):141
- Belyaev MA. 2015. *MNRAS* 449(3):2759–67
- Belyaev MA. 2017. arXiv:1707.01598
- Belyaev MA, Parfrey K. 2016. *Ap. J.* 830(2):119
- Benáček J, Muñoz PA, Büchner J. 2021a. *Ap. J.* 923:99
- Benáček J, Muñoz PA, Manthei AC, Büchner J. 2021b. *Ap. J.* 915(2):127
- Benford G, Buschauer R. 1977. *MNRAS* 179:189–207
- Beskin VS. 1990. *Sov. Astron. Lett.* 16:286–89
- Beskin VS. 2010. *MHD Flows Compact Astrophysical Objects: Accretion, Winds and Jets*. Berlin/Heidelberg: Springer

- Beskin VS. 2018. *Phys. Uspekhi* 61(4):353–80
- Beskin VS, Gurevich AV, Istomin IN. 1983. *Zhurnal Eksperimentalnoi Teor. Fiz.* 85:401–33
- Beskin VS, Gurevich AV, Istomin YN. 1988a. *Phys. Rev. Lett.* 61(5):649
- Beskin VS, Gurevich AV, Istomin YN. 1988b. *Ap. Space Sci.* 146:205–81
- Beskin VS, Gurevich AV, Istomin YN. 1993. *Physics of the Pulsar Magnetosphere*. Cambridge, UK: Cambridge Univ. Press
- Beskin VS, Philippov AA. 2012. *MNRAS* 425(2):814–40
- Bessho N, Bhattacharjee A. 2005. *Phys. Rev. Lett.* 95(24):245001
- Bhat NDR, Gupta Y, Kramer M, et al. 2007. *Astron. Astrophys.* 462(1):257–68
- Bhattacharjee A, Huang YM, Yang H, Rogers B. 2009. *Phys. Plasmas* 16(11):112102
- Bilous AV, Kondratiev VI, Kramer M, et al. 2016. *Astron. Astrophys.* 591:A134
- Blandford RD. 1975. *MNRAS* 170:551–57
- Blandford RD. 2002. In *Lighthouses of the Universe: The Most Luminous Celestial Objects and Their Use for Cosmology*, ed. M Gilfanov, R Sunyeav, E Churazov, pp. 381–404. Berlin/Heidelberg: Springer-Verlag
- Blandford RD, Scharlemann ET. 1976. *MNRAS* 174:59–85
- Blaskiewicz M, Cordes JM, Wasserman I. 1991. *Ap. J.* 370:643–69
- Bochenek CD, Ravi V, Belov KV, et al. 2020. *Nature* 587(7832):59–62
- Bornatici M, Kravtsov YA. 2000. *Plasma Phys. Control. Fusion* 42(3):255–64
- Brambilla G, Kalapotharakos C, Timokhin AN, Harding AK, Kazanas D. 2018. *Ap. J.* 858(2):81
- Bransgrove A, Beloborodov AM, Levin Y. 2020. *Ap. J.* 897(2):173
- Bransgrove A, Levin Y, Beloborodov A. 2018. *MNRAS* 473(2):2771–90
- Bucciantini N, Arons J, Amato E. 2011. *MNRAS* 410(1):381–98
- Budden KG. 1952. *Proc. R. Soc. A* 215(1121):215–33
- Burgay M, Bailes M, Bates SD, et al. 2013. *MNRAS* 433:259–69
- Caleb M, Keane E. 2021. *Universe* 7(11):453
- Caleb M, Rajwade K, Desvignes G, et al. 2021. *MNRAS* 510(2):1996–2010
- Camilo F, Cognard I, Ransom SM, et al. 2007a. *Ap. J.* 663(1):497–504
- Camilo F, Ransom SM, Chatterjee S, Johnston S, Demorest P. 2012. *Ap. J.* 746:63
- Camilo F, Ransom SM, Halpern JP, et al. 2006. *Nature* 442:892–95
- Camilo F, Reynolds J, Johnston S, et al. 2007b. *Ap. J. Lett.* 659(1):L37–40
- Cerutti B, Mortier J, Philippov AA. 2016a. *MNRAS* 463(1):L89–93
- Cerutti B, Philippov A, Parfrey K, Spitkovsky A. 2015. *MNRAS* 448(1):606–19
- Cerutti B, Philippov AA. 2017. *Astron. Astrophys.* 607:A134
- Cerutti B, Philippov AA, Dubus G. 2020. *Astron. Astrophys.* 642:A204
- Cerutti B, Philippov AA, Spitkovsky A. 2016b. *MNRAS* 457(3):2401–14
- Cerutti B, Werner GR, Uzdensky DA, Begelman MC. 2013. *Ap. J.* 770(2):147
- Chalumeau A, Babak S, Petiteau A, et al. 2021. *MNRAS*. 509(4):5538–58
- Champion D, Cognard I, Cruces M, et al. 2020. *MNRAS* 498(4):6044–56
- Chen AY, Beloborodov AM. 2014. *Ap. J. Lett.* 795(1):L22
- Chen AY, Cruz F, Spitkovsky A. 2020. *Ap. J.* 889(1):69
- Cheng AF, Ruderman M. 1979. *Ap. J.* 229:348–60
- Cheng AF, Ruderman MA. 1980. *Ap. J.* 235:576–86
- Cheng KS, Ho C, Ruderman M. 1986. *Ap. J.* 300:500–21
- CHIME/FRB Collab., Andersen BC, Bandura KM, et al. 2020. *Nature* 587(7832):54–58
- Chugunov YV, Shaposhnikov VE. 1988. *Astrophysics* 28:98–106
- Clifton T, Weisberg JM. 2008. *Ap. J.* 679:687–96
- Cocke WJ, Disney MJ, Taylor DJ. 1969. *Nature* 221:525–27
- Contopoulos I. 2019. *MNRAS* 482(1):L50–54
- Contopoulos I, Kazanas D, Fendt C. 1999. *Ap. J.* 511:351–58
- Contopoulos I, Stefanou P. 2019. *MNRAS* 487(1):952–60
- Cordes JM. 1976. *Ap. J.* 210:780–91
- Cordes JM. 1978. *Ap. J.* 222:1006–11

- Cordes JM. 1979. *Aust. J. Phys.* 32:9–24
- Cordes JM, Bhat NDR, Hankins TH, McLaughlin MA, Kern J. 2004. *Ap. J.* 612:375–88
- Cordes JM, Chatterjee S. 2019. *Annu. Rev. Astron. Astrophys.* 57:417–65
- Cordes JM, Weisberg JM, Hankins TH. 1990. *Astron. J.* 100:1882–91
- Cruz F, Grismayer T, Chen AY, Spitkovsky A, Silva LO. 2021. *Ap. J. Lett.* 919:L4
- Dai S, Hobbs G, Manchester RN, et al. 2015. *MNRAS* 449:3223–62
- Dai S, Lower ME, Bailes M, et al. 2019. *Ap. J. Lett.* 874(2):L14
- Davidson RC. 1990. *An Introduction to the Physics of Nonneutral Plasmas*. Redwood City, CA: Addison-Wesley
- Dawson JM. 1983. *Rev. Mod. Phys.* 55(2):403–47
- Desvignes G, Kramer M, Lee K, et al. 2019. *Science* 365(6457):1013–17
- Deutsch AJ. 1955. *Ann. d’Astrophys.* 18:1–10
- Drake FD, Craft HD. 1968. *Nature* 220:231–35
- Dyks J. 2008. *MNRAS* 391(2):859–68
- Eatough RP, Falcke H, Karuppusamy R, et al. 2013. *Nature* 501:391–94
- Edwards RT, Stappers BW. 2002. *Astron. Astrophys.* 393:733–48
- Eilek JA, Hankins TH. 2016. *J. Plasma Phys.* 82(3):635820302
- Enoto T, Terasawa T, Kisaka S, et al. 2021. *Science* 372(6538):187–90
- Espinoza CM, Antonopoulou D, Dodson R, Stepanova M, Scherer A. 2021. *Astron. Astrophys.* 647:A25
- Ferraro VCA. 1937. *MNRAS* 97:458–72
- Fussell D, Luo Q, Melrose DB. 2003. *MNRAS* 343(4):1248–56
- Gajjar V, Joshi BC, Kramer M, Karuppusamy R, Smits R. 2014. *Ap. J.* 797(1):18
- Galishnikova AK, Philippov AA, Beskin VS. 2020. *MNRAS* 497(3):2831–38
- Gil J, Lyubarsky Y, Melikidze GI. 2004. *Ap. J.* 600(2):872–82
- Gil JA, Lyne AG. 1995. *MNRAS* 276:L55–57
- Ginzburg VL, Zhelezniakov VV. 1975. *Annu. Rev. Astron. Astrophys.* 13:511–35
- Goldreich P, Julian WH. 1969. *Ap. J.* 157:869–80
- Goldreich P, Keeley DA. 1971. *Ap. J.* 170:463–77
- Gourgouliatos KN, Wood TS, Hollerbach R. 2016. *PNAS* 113(15):3944–49
- Gralla SE, Lupsasca A, Philippov A. 2016. *Ap. J.* 833(2):258
- Gralla SE, Lupsasca A, Philippov A. 2017. *Ap. J.* 851(2):137
- Gruzinov A. 1999. astro-ph/9902288
- Gruzinov A. 2005. *Phys. Rev. Lett.* 94(2):021101
- Guépin C, Cerutti B, Kotera K. 2020. *Astron. Astrophys.* 635:A138
- Guillot S, Kerr M, Ray PS, et al. 2019. *Ap. J. Lett.* 887(1):L27
- Gunn JE, Ostriker JP. 1970. *Ap. J.* 160:979–1002
- Guo F, Li H, Daughton W, Liu YH. 2014. *Phys. Rev. Lett.* 113(15):155005
- Gupta Y, Gangadhara RT. 2003. *Ap. J.* 584:418–26
- H.E.S.S. Collab., Abdalla H, Aharonian F, et al. 2018. *Astron. Astrophys.* 620:A66
- Hakobyan H, Petropoulou M, Spitkovsky A, Sironi L. 2021. *Ap. J.* 912(1):48
- Hakobyan H, Philippov A, Spitkovsky A. 2019. *Ap. J.* 877(1):53
- Hakobyan HL, Beskin VS, Philippov AA. 2017. *MNRAS* 469(3):2704–19
- Han JL, Manchester RN, Xu RX, Qiao GJ. 1998. *MNRAS* 300:373–87
- Hankins TH, Eilek JA, Jones G. 2016. *Ap. J.* 833(1):47
- Hankins TH, Jones G, Eilek JA. 2015. *Ap. J.* 802:130
- Hankins TH, Kern JS, Weatherall JC, Eilek JA. 2003. *Nature* 422:141–43
- Harding AK, Venter C, Kalapotharakos C. 2021. *Ap. J.* 923(2):194
- Hassall TE, Stappers BW, Hessels JWT, et al. 2012. *Astron. Astrophys.* 543:A66
- Hassall TE, Stappers BW, Weltevrede P, et al. 2013. *Astron. Astrophys.* 552:A61
- Hermsen W, Hessels JWT, Kuiper L, et al. 2013. *Science* 339:436–39
- Hermsen W, Kuiper L, Basu R, et al. 2018. *MNRAS* 480(3):3655–70
- Hermsen W, Kuiper L, Hessels JWT, et al. 2017. *MNRAS* 466(2):1688–708
- Hewish A, Bell SJ, Pilkington JDH, Scott PF, Collins RA. 1968. *Nature* 217:709–13

- Hibschman JA, Arons J. 2001. *Ap. J.* 546:382–93
- Hoshino M, Arons J, Gallant YA, Langdon AB. 1992. *Ap. J.* 390:454–79
- Hu R, Beloborodov AM. 2021. *Ap. J. Submitted*. arXiv:2109.03935
- Ilie CD, Johnston S, Weltevrede P. 2019. *MNRAS* 483(2):2778–94
- Istomin IN. 1988. *Zhurnal Eksperimentalnoi Teor. Fiz.* 94:148–58
- Istomin YN. 1994. *Astron. Astrophys.* 283:85–88
- Jankowski F, van Straten W, Keane EF, et al. 2018. *MNRAS* 473:4436–58
- Janet FA, Anderson SB, Prince TA. 2001. *Ap. J.* 546:394–400
- Jessner A, Popov MV, Kondratiev VI, et al. 2010. *Astron. Astrophys.* 524:A60
- Johnston S, Hobbs G, Vigeland S, et al. 2005. *MNRAS* 364(4):1397–412
- Johnston S, Karastergiou A. 2017. *MNRAS* 467(3):3493–99
- Johnston S, Karastergiou A, Mitra D, Gupta Y. 2008. *MNRAS* 388:261–74
- Johnston S, Kramer M. 2019. *MNRAS* 490(4):4565–74
- Johnston S, Weisberg JM. 2006. *MNRAS* 368(4):1856–70
- Jones P. 1986. *MNRAS* 222:577–91
- Jones PB. 2014. *MNRAS* 445(3):2297–301
- Jones PB. 2021. *MNRAS* 506(1):L26–28
- Kaganovich A, Lyubarsky Y. 2010. *Ap. J.* 721(2):1164–73
- Kalapotharakos C, Brambilla G, Timokhin A, Harding AK, Kazanas D. 2018. *Ap. J.* 857(1):44
- Kalapotharakos C, Contopoulos I. 2009. *Astron. Astrophys.* 496(2):495–502
- Kalapotharakos C, Harding AK, Kazanas D. 2014. *Ap. J.* 793(2):97
- Kalapotharakos C, Harding AK, Kazanas D, Wadiasingh Z. 2019. *Ap. J. Lett.* 883(1):L4
- Karastergiou A, von Hoensbroeck A, Kramer M, et al. 2001. *Astron. Astrophys.* 379:270–78
- Kaspi VM, Beloborodov AM. 2017. *Annu. Rev. Astron. Astrophys.* 55:261–301
- Kazbegi AZ, Machabeli GZ, Melikidze GI. 1991. *MNRAS* 253:377–87
- Keane EF, Kramer M, Lyne AG, Stappers BW, McLaughlin MA. 2011. *MNRAS* 415:3065–80
- Keane EF, McLaughlin MA. 2011. *Bull. Astron. Soc. India* 39(3):333–52
- Keith MJ, Shannon RM, Johnston S. 2013. *MNRAS* 432:3080–84
- Komissarov SS. 1999. *MNRAS* 303(2):343–66
- Komissarov SS. 2006. *MNRAS* 367(1):19–31
- Kondratiev VI, Verbiest JPW, Hessels JWT, et al. 2016. *Astron. Astrophys.* 585:A128
- Kramer M. 1994. *Astron. Astrophys.* 107:527–39
- Kramer M. 1998. *Ap. J.* 509:856–60
- Kramer M, Jessner A, Doroshenko O, Wielebinski R. 1997a. *Ap. J.* 489:364–67
- Kramer M, Johnston S. 2008. *MNRAS* 390(1):87–92
- Kramer M, Johnston S, van Straten W. 2002. *MNRAS* 334:523–32
- Kramer M, Karastergiou A, Gupta Y, et al. 2003. *Astron. Astrophys.* 407:655–68
- Kramer M, Lange C, Lorimer DR, et al. 1999. *Ap. J.* 526:957–75
- Kramer M, Lyne AG, O'Brien JT, Jordan CA, Lorimer DR. 2006. *Science* 312:549–51
- Kramer M, Stairs IH. 2008. *Annu. Rev. Astron. Astrophys.* 46:541–72
- Kramer M, Stairs IH, Venkatraman Krishnan V, et al. 2021. *MNRAS* 504(2):2094–114
- Kramer M, Stappers BW, Jessner A, Lyne AG, Jordan CA. 2007. *MNRAS* 377(1):107–19
- Kramer M, Xilouris KM, Jessner A, et al. 1997b. *Astron. Astrophys.* 322:846–56
- Kramer M, Xilouris KM, Lorimer DR, et al. 1998. *Ap. J.* 501:270–85
- Krause-Polstorff J, Michel FC. 1985. *MNRAS* 213:43P–49P
- Kuiper L, Hermsen W. 2015. *MNRAS* 449(4):3827–66
- Kumamoto H, Dai S, Johnston S, et al. 2021. *MNRAS* 501(3):4490–513
- Landau LD. 1932. *Phys. Z. Sowjetunion* 1:285–88
- Landau LD, Lifshitz EM. 1975. *The Classical Theory of Fields*, Vol. 2, *Course of Theoretical Physics*. Oxford, UK: Pergamon. 4th ed.
- Larroche O, Pellat R. 1987. *Phys. Rev. Lett.* 59(10):1104–7
- Lazaridis K, Jessner A, Kramer M, et al. 2008. *MNRAS* 390(2):839–46

- Levin L, Bailes M, Bates S, et al. 2010. *Ap. J. Lett.* 721:L33–37
- Levin L, Lyne AG, Desvignes G, et al. 2019. *MNRAS* 488(4):5251–58
- Li J, Spitskovsky A, Tchekhovskoy A. 2012. *Ap. J. Lett.* 746(2):L24
- Lifshitz EM, Pitaevskii LP. 1981. *Physical Kinetics*, Vol. 10, *Course of Theoretical Physics*. Oxford, UK: Butterworth-Heinemann
- Liu K, Desvignes G, Eatough RP, et al. 2021. *Ap. J.* 914(1):30
- Liu K, Young A, Wharton R, et al. 2019. *Ap. J. Lett.* 885(1):L10
- Lorimer DR, Bailes M, McLaughlin MA, Narkevic DJ, Crawford F. 2007. *Science* 318:777–80
- Lorimer DR, Kramer M. 2005. *Handbook of Pulsar Astronomy*. Cambridge, UK: Cambridge Univ. Press
- Lorimer DR, Lyne AG, McLaughlin MA, et al. 2012. *Ap. J.* 758(2):141
- Lorimer DR, Stairs IH, Freire PC, et al. 2006. *Ap. J.* 640(1):428–34
- Loureiro NF, Uzdensky DA. 2016. *Plasma Phys. Control. Fusion* 58(1):014021
- Lovelace RVE, Sutton JM. 1969. *IAU Circ.* 2135:2
- Luo Q, Melrose DB. 1992. *MNRAS* 258:616–20
- Lyne A, Graham-Smith F, Weltevrede P, et al. 2013. *Science* 342(6158):598–601
- Lyne A, Hobbs G, Kramer M, Stairs I, Stappers B. 2010. *Science* 329:408–12
- Lyne AG, Burgay M, Kramer M, et al. 2004. *Science* 303:1153–57
- Lyne AG, Graham-Smith F. 2006. *Pulsar Astronomy*. Cambridge, UK: Cambridge Univ. Press
- Lyne AG, Manchester RN. 1988. *MNRAS* 234:477–508
- Lyne AG, Stappers BW, Freire PCC, et al. 2017. *Ap. J.* 834:72
- Lyubarskii YE. 1996a. *Astron. Astrophys.* 308:809–20
- Lyubarskii YE. 1996b. *Astron. Astrophys.* 311:172–78
- Lyubarskii YE, Petrova SA. 1998. *Astron. Astrophys.* 333:181–87
- Lyubarskii YE, Petrova SA. 1999. *Ap. Space Sci.* 262:379–89
- Lyubarsky Y. 2019. *MNRAS* 483(2):1731–36
- Lyubarsky Y. 2021. *Universe* 7(3):56
- Lyutikov M. 2007. *MNRAS* 381(3):1190–96
- Lyutikov M. 2021. arXiv:2110.12455
- Lyutikov M, Machabeli G, Blandford R. 1999. *Ap. J.* 512(2):804–26
- Machabeli GZ. 1991. *Plasma Phys. Control. Fusion* 33(11):1227–34
- Maciesiak K, Gil J, Ribeiro VARM. 2011. *MNRAS* 414(2):1314–28
- Mahlmann JF, Aloy MA, Mewes V, Cerdá-Durán P. 2021. *Astron. Astrophys.* 647:A58
- Main R, Lin R, van Kerkwijk MH, et al. 2021. *Ap. J.* 915(1):65
- Malofeev VM, Gil JA, Jessner A, et al. 1994. *Astron. Astrophys.* 285:201–8
- Malov IF, Malofeev VM. 1991. *Astron. Zh.* 68:362–72
- Manchester RN, Hobbs GB, Teoh A, Hobbs M. 2005. *Astron. J.* 129:1993–2006
- Manchester RN, Kramer M, Stairs IH, et al. 2010. *Ap. J.* 710:1694–709
- Manchester RN, Taylor JH, Huguenin GR. 1975. *Ap. J.* 196:83–102
- Maron O, Kijak J, Kramer M, Wielebinski R. 2000. *Astron. Astrophys.* 147:195–203
- McKinnon M. 1997. *Ap. J.* 475:763–69
- McLaughlin MA, Lyne AG, Keane EF, et al. 2009. *MNRAS* 400:1431–38
- McLaughlin MA, Lyne AG, Lorimer DR, et al. 2006. *Nature* 439:817–20
- Mehlhaff JM, Werner GR, Uzdensky DA, Begelman MC. 2021. *MNRAS* 508(3):4532–72
- Melikidze GI, Gil JA, Pataraya AD. 2000. *Ap. J.* 544(2):1081–96
- Melrose DB. 1978. *Ap. J.* 225:557–73
- Melrose DB. 1981. In *Pulsars, IAU Symp.* 95, ed. W Sieber, R Wielebinski, pp. 133–39. Dordrecht, Neth.: Reidel
- Melrose DB. 1992. In *Magnetospheric Structure and Emission Mechanics of Radio Pulsars, IAU Colloq.* 128, ed. TH Hankins, JM Rankin, JA Gil, pp. 305–15. Cambridge, UK: Cambridge Univ. Press
- Melrose DB. 2017. *Rev. Mod. Plasma Phys.* 1(1):5
- Melrose DB, Gedalin ME. 1999. *Ap. J.* 521:351–61
- Melrose DB, Rafat MZ, Mastrano A. 2021a. *MNRAS* 500(4):4549–59

- Melrose DB, Rafat MZ, Mastrano A. 2021b. *MNRAS* 500(4):4530–48
- Mestel L. 1971. *Nature* 233:149–52
- Mestel L. 1973. *Ap. Space Sci.* 24(1):289–97
- Mestel L, Panagi P, Shibata S. 1999. *MNRAS* 309(2):388–94
- Mestel L, Robertson JA, Wang YM, Westfold KC. 1985. *MNRAS* 217:443–84
- Michel FC. 1973. *Ap. J. Lett.* 180:L133–37
- Michel FC, Li H. 1999. *Phys. Rep.* 318:227–97
- Mikami R, Asano K, Tanaka SJ, et al. 2016. *Ap. J.* 832(2):212
- Mikhailovskii AB, Onishchenko OG, Suramlishvili GI, Sharapov SE. 1982. *Sov. Astron. Lett.* 8:369–71
- Mikhaylenko AG, Beskin VS, Istomin YN. 2021. *J. Plasma Phys.* 87(1):905870105
- Miller MC, Lamb FK, Dittmann AJ, et al. 2019. *Ap. J. Lett.* 887(1):L24
- Miller MC, Lamb FK, Dittmann AJ, et al. 2021. *Ap. J. Lett.* 918(2):L28
- Mochol I, Petri J. 2015. *MNRAS* 449:L51–55
- Moffett DA, Hankins TH. 1996. *Ap. J.* 468:779
- Moffett DA, Hankins TH. 1999. *Ap. J.* 522:1046–52
- Mottez F, Bonazzola S, Heyvaerts J. 2013. *Astron. Astrophys.* 555:A125
- Mueller E. 1984. *Astron. Astrophys.* 130(2):415–18
- Muslimov AG, Harding AK. 2004. *Ap. J.* 606:1143–53
- Muslimov AG, Tsygan AI. 1992. *MNRAS* 255:61–70
- Nambu M. 1989. *Plasma Phys. Control. Fusion* 31(1):143–45
- Nambu M. 1996. *Phys. Plasmas* 3(12):4325–35
- Noutsos A, Karastergiou A, Kramer M, Johnston S, Stappers BW. 2009. *MNRAS* 396(3):1559–72
- Pacini F. 1967. *Nature* 216:567–68
- Palfreyman J, Dickey JM, Hotan A, Ellingsen S, van Straten W. 2018. *Nature* 556:219–22
- Parfrey K, Beloborodov AM, Hui L. 2012. *MNRAS* 423(2):1416–36
- Parthasarathy A, Johnston S, Shannon RM, et al. 2020. *MNRAS* 494(2):2012–26
- Pétri J. 2012. *MNRAS* 424(3):2023–27
- Pétri J, Heyvaerts J, Bonazzola S. 2002. *Astron. Astrophys.* 384:414–32
- Petroff E, Hessels JWT, Lorimer DR. 2019. *Astron. Astrophys. Rev.* 27(1):4
- Petropoulou M, Sironi L. 2018. *MNRAS* 481(4):5687–701
- Petrova SA. 2001. *Astron. Astrophys.* 378:883–97
- Petrova SA, Lyubarskii YE. 2000. *Astron. Astrophys.* 355:1168–80
- Philippov A, Tchekhovskoy A, Li JG. 2014. *MNRAS* 441(3):1879–87
- Philippov A, Timokhin A, Spitkovsky A. 2020. *Phys. Rev. Lett.* 124(24):245101
- Philippov A, Uzdensky DA, Spitkovsky A, Cerutti B. 2019. *Ap. J. Lett.* 876(1):L6
- Philippov AA, Cerutti B, Tchekhovskoy A, Spitkovsky A. 2015a. *Ap. J. Lett.* 815(2):L19
- Philippov AA, Spitkovsky A. 2014. *Ap. J. Lett.* 785(2):L33
- Philippov AA, Spitkovsky A. 2018. *Ap. J.* 855(2):94
- Philippov AA, Spitkovsky A. 2015b. *Ap. J. Lett.* 801(1):L19
- Phillips JA, Wolszczan A. 1991. *Ap. J. Lett.* 382:L27–30
- Posselt B, Karastergiou A, Johnston S, et al. 2021. *MNRAS* 508(3):4249–68
- Potekhin AY. 2014. *Phys. Uspekhi* 57(8):735–70
- Radhakrishnan V, Cooke DJ. 1969. *Ap. Lett.* 3:225–29
- Rafat MZ, Melrose DB, Mastrano A. 2019. *J. Plasma Phys.* 85(3):905850311
- Ramachandran R, Kramer M. 2003. *Astron. Astrophys.* 407:1085–95
- Rankin JM. 1983. *Ap. J.* 274:333–58
- Rankin JM. 1990. *Ap. J.* 352:247–57
- Rea N, Kramer M, Stella L, et al. 2008. *MNRAS* 391(2):663–67
- Riley TE, Watts AL, Bogdanov S, et al. 2019. *Ap. J. Lett.* 887(1):L21
- Riley TE, Watts AL, Ray PS, et al. 2021. *Ap. J. Lett.* 918(2):L27
- Riquelme MA, Quataert E, Verscharen D. 2015. *Ap. J.* 800(1):27
- Robinson BJ, Cooper BFC, Gardiner FF, Wielebinski R, Landecker TL. 1968. *Nature* 218:1143–45

- Romani RW. 1996. *Ap. J.* 470:469–78
- Ruderman M. 1974. In *Physics of Dense Matter, IAU Symp. 53*, ed. CJ Hansen, pp. 117–31. Dordrecht/Boston: Reidel
- Ruderman M, Zhu T, Chen K. 1998. *Ap. J.* 492:267–80
- Ruderman MA, Sutherland PG. 1975. *Ap. J.* 196:51–72
- Scharlemann ET, Wagoner RV. 1973. *Ap. J.* 182:951–60
- Serylak M, Johnston S, Kramer M, et al. 2021. *MNRAS* 505(3):4483–95
- Serylak M, Stappers BW, Weltevrede P, et al. 2009. *MNRAS* 394(1):295–308
- Shearer A, Golden A. 2002. In *Proceedings of the 270. WE-Heraeus Seminar on Neutron Stars, Pulsars, and Supernova Remnants*, MPE Report 278, ed. W Becker, H Lesch, J Trümper, pp. 44–53. Garching bei München: Max-Planck Institut
- Shearer A, Stappers B, O'Connor P, et al. 2003. *Science* 301:493–95
- Sironi L, Giannios D, Petropoulou M. 2016. *MNRAS* 462(1):48–74
- Sironi L, Spitkovsky A. 2014. *Ap. J. Lett.* 783(1):L21
- Slowikowska A, Kanbach G, Kramer M, Stefanescu A. 2009. *MNRAS* 397(1):103–23
- Spiewak R, Bailes M, Miles MT, et al. 2022. *Publ. Astron. Soc. Aust.* Accepted
- Spitkovsky A. 2006. *Ap. J. Lett.* 648(1):L51–54
- Spitkovsky A, Arons J. 2002. In *Neutron Stars in Supernova Remnants*, ed. PO Slane, BM Gaensler, pp. 81–86. San Francisco: ASP
- Spolon A, Zampieri L, Burtovoi A, et al. 2019. *MNRAS* 482(1):175–83
- Staelin DH, Reifenstein EC III. 1968. *Science* 162:1481–83
- Sturrock PA. 1971. *Ap. J.* 164:529–56
- Tauris TM, Manchester RN. 1998. *MNRAS* 298:625–36
- Tchekhovskoy A, Spitkovsky A, Li JG. 2013. *MNRAS* 435:L1–5
- Thompson D. 2004. In *Young Neutron Stars and Their Environments, IAU Symp. 218*, ed. F Camilo, BM Gaensler, pp. 399–406. San Francisco: ASP
- Thorsett SE. 1991. *Ap. J.* 377:263–67
- Timokhin AN. 2006. *MNRAS* 368(3):1055–72
- Timokhin AN. 2010. *MNRAS* 408:L41–45
- Timokhin AN, Arons J. 2013. *MNRAS* 429(1):20–54
- Timokhin AN, Harding AK. 2015. *Ap. J.* 810(2):144
- Timokhin AN, Harding AK. 2019. *Ap. J.* 871(1):12
- Tolman EA, Philippov AA, Timokhin AN. 2022. arXiv:2202.01303
- Torne P. 2016. *Exploring radio pulsars with new technologies*. PhD Thesis, Univ. Bonn, Bonn, Ger.
- Torne P, Bell GS, Bintley D, et al. 2022. *Ap. J. Lett.* 925(2):L17
- Torne P, Desvignes G, Eatough RP, et al. 2017. *MNRAS* 465:242–47
- Torne P, Eatough RP, Karuppusamy R, et al. 2015. *MNRAS* 451:L50–54
- Torne P, Macias-Pérez J, Ladjelate B, et al. 2020. *Astron. Astrophys.* 640:L2
- Uzdensky DA. 2016. In *Magnetic Reconnection: Concepts and Applications*, ed. W Gonzalez, E Parker, *Ap. Space Sci. Libr.* 427:473–519. Princeton, NJ: Princeton Univ. Press
- Uzdensky DA, Loureiro NF, Schekochihin AA. 2010. *Phys. Rev. Lett.* 105(23):235002
- Uzdensky DA, Spitkovsky A. 2014. *Ap. J.* 780(1):3
- van Leeuwen J, Kasian L, Stairs IH, et al. 2015. *Ap. J.* 798:118
- Venkatraman Krishnan V, Bailes M, van Straten W, et al. 2019. *Ap. J. Lett.* 873(2):L15
- von Hoensbroech A, Kijak J, Krawczyk A. 1998a. *Astron. Astrophys.* 334:571–84
- von Hoensbroech A, Lesch H, Kunzl T. 1998b. *Astron. Astrophys.* 336:209–19
- Wang C, Lai D, Han J. 2010. *MNRAS* 403(2):569–88
- Wang N, Manchester RN, Johnston S. 2007. *MNRAS* 377:1383–92
- Weisberg JM, Taylor JH. 2002. *Ap. J.* 576:942–49
- Weltevrede P, Johnston S. 2008. *MNRAS* 391:1210–26
- Weltevrede P, Johnston S, Espinoza CM. 2011. *MNRAS* 411:1917–34
- Weltevrede P, Stappers BW, Rankin JM, Wright GAE. 2006. *Ap. J. Lett.* 645(2):L149–52

- Werner GR, Uzdensky DA, Cerutti B, Nalewajko K, Begelman MC. 2016. *Ap. J. Lett.* 816(1):L8
- Wiegelmann T, Sakurai T. 2021. *Liv. Rev. Solar Phys.* 18(1):1
- Xilouris KM, Kramer M, Jessner A, Wielebinski R. 1994. *Astron. Astrophys.* 288:L17–20
- Xilouris KM, Kramer M, Jessner A, Wielebinski R, Timofeev M. 1996. *Astron. Astrophys.* 309:481–92
- Yakovlev DG, Haensel P, Baym G, Pethick C. 2013. *Phys. Uspekhi* 56(3):289–95
- Yuan Y, Levin Y, Bransgrove A, Philippov A. 2021. *Ap. J.* 908(2):176
- Yuen R, Melrose DB. 2014. *Publ. Astron. Soc. Aust.* 31:e039
- Zhang H, Sironi L, Giannios D. 2021. *Ap. J.* 922(2):261
- Zheleznyakov VV. 1970. *Radio Emission of the Sun and Planets*. Oxford, UK: Pergamon
- Zheleznyakov VV, Shaposhnikov VE. 1979. *Aust. J. Phys.* 32:49–60